Fall 2017

EVALUATING SATELLITE DERIVED BATHYMETRY IN REGARD TO TOTAL PROPAGATED UNCERTAINTY, MULTI-TEMPORAL CHANGE DETECTION, AND MULTIPLE NON-LINEAR ESTIMATION

Ricardo Ramos Freire
University of New Hampshire, Durham

EVALUATING SATELLITE DERIVED BATHYMETRY IN REGARD TO TOTAL PROPAGATED UNCERTAINTY, MULTI-TEMPORAL CHANGE DETECTION, AND MULTIPLE NON-LINEAR ESTIMATION

BY

RICARDO RAMOS FREIRE

B.S. in Cartographic Engineering, Rio de Janeiro State University, Rio de Janeiro, Brazil (2003)

M.S. in Computer Engineering, Rio de Janeiro State University, Rio de Janeiro, Brazil (2009)

DISSERTATION

Submitted to the University of New Hampshire

in partial fulfillment of

the requirements for the degree of

Doctor of Philosophy

in

Ocean Engineering

September, 2017

This dissertation has been examined and approved.

Dr. Shachak Pe'eri (Dissertation Director)
Affiliate Associate Professor
Center for Coastal and Ocean Mapping

Dr. Lee Alexander
Research Associate Professor Emeritus
Center for Coastal and Ocean Mapping

Dr. Thomas C. Lippmann
Associate Professor
Center for Coastal and Ocean Mapping

Dr. Christopher E. Parrish
Affiliate Professor
Center for Coastal and Ocean Mapping

Dr. Yuri Rzhanov
Research Professor
Center for Coastal and Ocean Mapping

On July 20th 2017

Original approval signatures are on file with the University of New Hampshire Graduate School.

DEDICATION

I would like to dedicate this work to my wife Adriane and my daughters Anabella and Angelica, whose presence and support were essential to my success.

ACKNOWLEDGEMENTS

First, I would like to thank my Creator for providing me with the conditions to successfully conclude my studies.

I would also like to thank my loved wife Adriane, who agreed to live in a foreign country and, despite the language barrier, was always ready to support me. To my daughters Anabella and Angelica, you bring out my best. I love my three girls.

I would like to express my gratitude to Brazilian Navy and Science without Borders Program, for trusting and designating me in this mission and also for sponsoring my expenses.

In addition, I would like to give other special acknowledgements to these special people that have supported me along this journey:

- My main advisor, Dr. Shachak Pe'eri for your patience, dedication, generosity and friendship along four years of technical discussions. Dr. Lee Alexander, for helping me before I arrive to UNH and enthusiastically revising my texts. Dr. Christopher E. Parrish, for your amazing classes and example of humility. Dr. Yuri Rzhanov, for always having your door open to listen and contribute. Dr. Thomas C. Lippmann, for your persistence and commitment that allowed a cartographer briefly understand the basics on nearshore hydrodynamics. The suggestions you all provided enriched my research and I have no words to describe how thankful I am;

- Colonel Amauri Ribeiro Destri (Brazilian Army, Rio de Janeiro State University), Colonel Jorge Luis Nunes e Silva Brito (Brazilian Army, Rio de Janeiro State University) and Professor Julia Celia Mercedes Strauch (Rio de Janeiro State University), for placing your trust in my skills. Thanks for your letters of recommendation;

- Captain Ana Cláudia de Paula (Brazilian Navy) and Captain Lucia Artusi (Brazilian Navy), for helping me with administrative procedures along these years;

- Captain Rogério de Oliveira Gonçalves (Brazilian Navy), for your support along the selection process;

- Commander Paulo Pereira Oliveira Matos (Brazilian Navy), my Navy co-advisor, for your cooperation and availability along the years;

- Lieutenant Commander Anderson Barbosa da Cruz Peçanha, for our friendship, especially when you took care of Anabella the day Angelica was born. You were having your finals and never had a second thought about it. My wife and I will always remember it. Thank you so much;

- Carlo Lanzoni and his wife Neide, for you friendship and kindness;

- Andy Armstrong, Brian Calder, James Gardner, James Irish, Joel Johnson, John Kelley, Larry Mayer, Larry Ward, Rochelle Wigley, Semme Dijkstra, Steve Wineberg, Thomas Weber and Val Schimidt, for your memorable teachings;

- Jordan Chadwick, Will Fessenden and all the IT guys, for your irreproachable support;

- Other faculty and staff members of the Center for Coastal and Ocean Mapping / Joint Hydrographic Center, for your valuable support; and

- To my family, whose love was always felt despite the distance. Each and every one of you gave us (my wife and I) strength to persist and finish the job. Thank you very much!

TABLE OF CONTENTS

LIST OF TABLES

LIST OF FIGURES

ABSTRACT

EVALUATING SATELLITE DERIVED BATHYMETRY IN REGARD TO TOTAL PROPAGATED UNCERTAINTY, MULTI-TEMPORAL CHANGE DETECTION, AND MULTIPLE NON-LINEAR ESTIMATION

BY

RICARDO RAMOS FREIRE
University of New Hampshire, September, 2017

Acoustic and electromagnetic hydrographic surveys produce highly-accurate bathymetric data that can be used to update and improve current nautical charts. For shallow-water surveys (i.e., less than 50m depths), this includes the use of single-beam echo-sounders (SBES), multi-beam echo-sounders (MBES), and airborne lidar bathymetry (ALB). However, these types of hydrographic surveys are time-consuming and require considerable financial and operational resources to conduct. As a result, some maritime regions are seldom surveyed due to their remote location and challenging logistics.

Satellite-derived bathymetry (SDB) provides a means to supplement traditional acoustic hydrographic surveys. In particular, Landsat 8 imagery: 1) provides complete coverage of the Earth's surface every 16 days, 2) has an improved dynamic range (12-bits), and 3) is freely-available from the US Geological Survey. While the 30 m spatial resolution does not match MBES, ALB, or SBES coverage, SDB based on Landsat 8 can be regarded as a type of "reconnaissance survey" that can be used to identify potential hazards to navigation in areas that are seldom surveyed. It is also a useful means to monitor change detection in dynamic regions.

This study focused on developing improved image-processing techniques and time-series analysis for SDB from Landsat 8 imagery for three different applications:

1. An improved means to estimate total propagated uncertainty (TPU), mainly the vertical component, for single-image SDB;
2. Identifying the location and movement of dynamic shallow areas in river entrances based on multiple-temporal Landsat 8 imagery;
3. Using a multiple, nonlinear SDB approach to enhance depth estimations and enable bottom discrimination.

An improved TPU estimation was achieved based on the two most common optimization approaches (Dierssen et al., 2003 and Stumpf et al., 2003). Various single-image SDB band-ratio outcomes and associated uncertainties were compared against ground truth (i.e., recent Lidar surveys). Several parameters were tested, including various types of filters, kernel sizes, number of control points and their coverage, and recent vs. outdated control points. Based on the study results for two study sites (Cape Ann, MA and Ft Myers, FL), similar performance was observed for both the Stumpf and the Dierssen models. Validation was performed by comparing estimated depths and uncertainties to observed ALB data. The best performing configuration was achieved using low-pass filter (kernel size 3x3) with ALB control points that were distributed over the entire study site.

A change detection process using image processing was developed to identify the location and movement of dynamic shallow areas in riverine environments. Yukon River (Alaska) and Amazon River (Brazil) entrances were evaluated as study sites using multiple satellite imagery. A time-series analysis was used to identify probable shallow areas with no usable control points. By using an SDB ratio model with image processing techniques that includes feature extraction and a

well-defined topological feature to describe the shoal feature, it is possible to create a time-series of the shoal's motion, and predict its future location. A further benefit of this approach is that vertical referencing of the SDB ratio model to chart datum is not required.

In order to enhance the capabilities of the SDB approach to estimate depth in non-uniform conditions, Dierssen's band ration SDB algorithm was transformed into a full non-linear SDB model. The model was evaluated in the Simeonof Island, AK, using Lidar control points from a previous NOAA ALB survey. Linear and non-linear SDB models were compared using the ALB survey for performance evaluation. The multi-nonlinear SDB model provides an enhanced performance compared to the more traditional linear SDB method. This is most noticeable in the very shallow waters (0-2 m), where a linear model does not provide a good correlation to the control points. In deep-waters close to the extinction depth, the multi-nonlinear SDB method is also able to better detect bottom features than the linear SDB method. By recognizing the water column contributions to the SDB solution, it is possible to achieve a more accurate estimate of the bathymetry in remote areas.

CHAPTER 1

INTRODUCTION

1.1 Traditional Hydrographic surveying

According to International Hydrographic Organization (IHO) Standards for Hydrographic Surveys Special Publication Nº 44 (S-44, 2008), the basic purpose for conducting hydrographic surveys is to compile depth data to be used in nautical charts. However, such factors as the density of the depth data, the uncertainty of depth measurements, the ability detect or define underwater features, and the frequency in which surveys are conducted all affect the ability to provide sufficient information to ensure safety-of-navigation.

Historically, hydrographic surveys were conducted from ships and boats using various types of equipment, systems and procedures. In early days, direct measurements of depth were conducted using a lead line and a sounding pole. In the mid 1900's, single-beam echo sounders (SBES) that were developed from military sonars started to be used in hydrographic surveys (IHO Manual of Hydrography, C-13, 2011). Side-scan sonar came into use in the 1970's, but was primarily used for object detection. Beginning in the 1990's multi-beam echo sounder (MBES) and airborne lidar bathymetry (ALB) started to be used. Today, in relatively shallow-water areas (i.e., < 100 m depth) the most commonly used systems include SBES, MBES, ALB and side-scan sonar.

While these types of systems provide high-accuracy measurements that meet IHO S-44 requirements, conducting surveys from vessels or airplanes require considerable resource

management and logistics. For instance, the survey vessel must transit to the study site, and there are high costs associated with installing/maintaining the survey system equipment and personnel. Ground support for horizontal/vertical control is often a major challenge. Sea-state conditions and weather affect the size of the survey vessel and boats that are required to conduct the survey. In particular, the size and location of shallow water areas can significantly impact the amount of underway time required to transit to and survey the area. The number of teams and the necessary skills of survey personnel can be significant. In addition, medical support, transportation, shore accommodation, food and water supplies, and other provisions all impact the endurance of surveying crew. Regardless, these efforts must be performed to achieve suitable results that can be used for producing nautical charts and ensuring safety-of-navigation. However, because of the operational and logistical challenges, the number and frequency of surveys conducted, and their geographic coverage are often quite limited. This becomes even more difficult when hydrographic offices are faced with increasingly limited budgets.

1.2 Satellite Derived Bathymetry (SDB)

An alternative approach is the use of Satellite Derived Bathymetry (SDB). Recent studies and reports have shown that it can be an effective reconnaissance survey tool by providing a bathymetric model from a single satellite imagery and control points provided from the chart or a survey of opportunity (Pe'eri et al., 2014). Current access to publicly-available satellite imagery (e.g., *Landsat 8*, *CBERS-4*, and *Sentinel-2A*) provide repeatable coverage over most of the globe, and provide a means to infer bathymetry and bathymetry changes in remote areas that are difficult to access (Pe'eri et al., 2016).

Unlike active sensors used in echo-sounders or lidar systems that calculate water depth based on two-way travel time of a well-controlled transmitted signal, bathymetry derived from optical satellite imagery is inferred from image pixel values, based on intensity changes of an external source of radiation (e.g., sunlight) that is emitted or reflected by the target (i.e., the bottom). The optical imagery is generated using radiometers that scan specific ranges of spectrum. The SDB approach is based on the optical characteristics of light as it exponentially decays through the water column. The decay rate through the water column varies for different wavelengths and water conditions (Jerlov, 1976). The development of SDB began in the late 1960s (Polcyn and Rollin, 1969) and has since evolved to multiple approaches (e.g., Lyzenga, 1978, Philpot et al., 2004; Stumpf et al., 2003; Dierssen et al., 2003; Louchard et al. 2003; Lyzenga 2006; Vanderstraete et al. 2006; Hogfe et al. 2008; Su et al. 2008; Bachmann et al. 2012; Flener et al. 2012; Bramante et al. 2013).

Although the use of SDB information in nautical charts is not well established worldwide, several hydrographic offices have started using this approach for updating their products. NOAA has been utilizing the SDB approach for marking features on their charts. Figure 1.1 shows an example of NOAA Chart 16081 (Raster chart and Electronic Navigational Chart) that includes the location of the potential uncharted shoal with a supplemental note and an illustration in the source diagram. NOAA has also utilized SDB for other charts in Alaska and along the western Florida coastlines. Similarly in France, SHOM has also been using SDB to update their charting products. As shown in Figure 1.2, SDB has been used to update the southern part of SHOM Chart 7458 (Aratika Atoll chart in French Polynesia). In both cases SDB is a reconnaissance survey technology with the lowest hydrographic quality (i.e., CATZOC D). As such, all chart soundings have been

removed and only approximate depth contours were marked (Tournay and Quemeneur, 2013; Pe'eri et al., 2016).

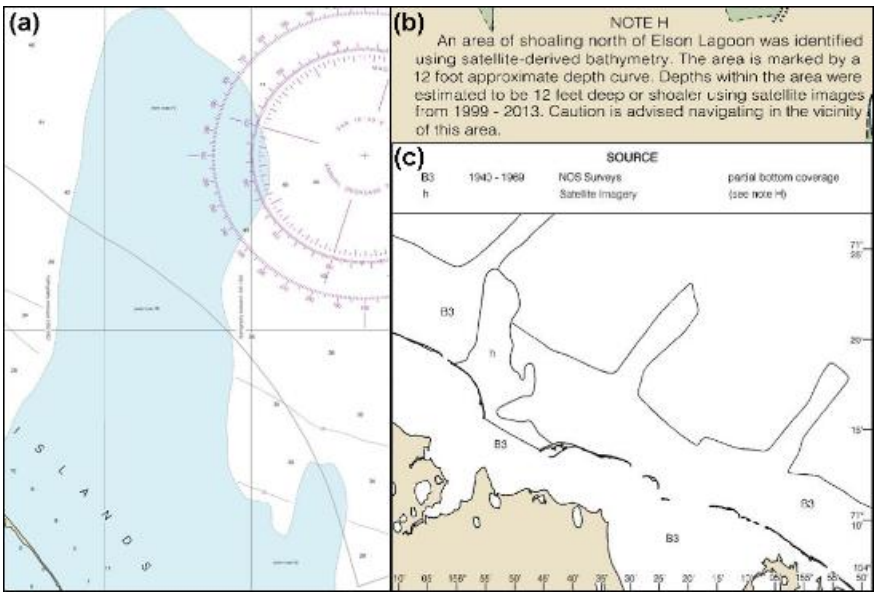

Figure 1.1. NOAA Raster Chart 16081 that includes a new shoal that was identified using multi-temporal SDB: (a) revised 12-foot contour marking the location of the new shoal, (b) chart note describing the method used to identify the shoal, and (c) source diagram. (Peeri et al., 2016).

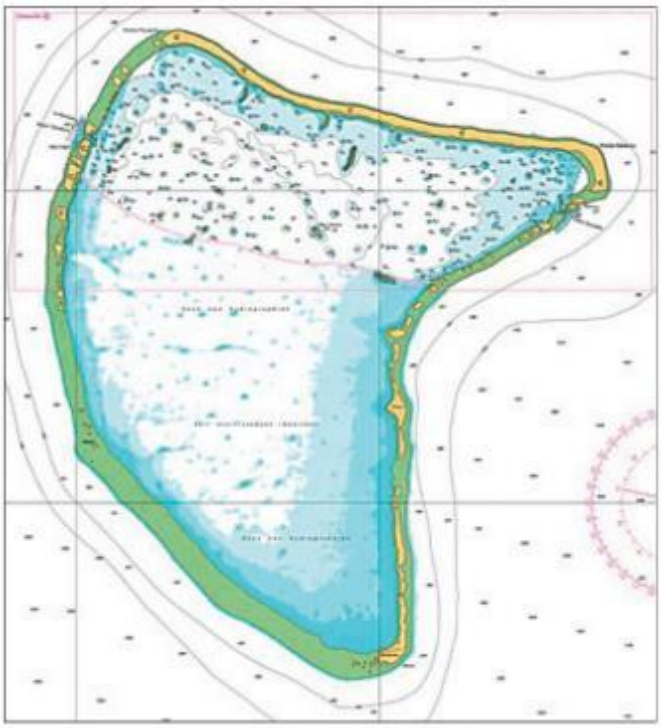

Figure 1.2. SHOM Chart 7458 of Aratika Atoll chart in French Polynesia. The southern part of the Atoll has been updated with SDB information. As such, the depth areas are marked with different colors than the traditional chart (northern part of the chart). Also, all soundings in the areas that were updated using SDB have been removed (Tournay and Quemeneur, 2013).

The physical assumption for the success for a band-ratio SDB approach is that the models assume a uniform bottom reflectance and water attenuation (Philpot, 1989; Dierssen et al., 2003; Stumpf et al., 2003). This assumption implies that any changes in either of these environmental parameters are minor with respect to the depth calculation. Therefore, it is assumed that a linear relationship exists between calibrations points (i.e., soundings) and the SDB model (i.e., the log ratio values between two bands of the satellite imagery). As such, SDB is typically used in tropical and subtropical regions with clear water conditions, and especially over sandy bottom areas (Stumpf et al., 2003; Philpot et al., 2004; Pe'eri et al., 2014). Another reason for the success of SDB as a reconnaissance tool for marine applications is that there no need to measure the tide

height during the image acquisition because transformation parameters used to vertically reference bathymetric model are accounted for though the use of control points that are selected from a nautical chart or smooth sheet, and are already in chart datum (e.g., Mean Lower Low Waters or Low Astronomical Tide).

Although this procedure is relatively simple, it is important to note its limitations. The first is that this procedure is a reconnaissance tool and is not meant to replace traditional hydrographic survey technology (e.g., echo-sounders or ALB). Also, IHO S-44 document specifies that surveys used for charting application have an uncertainty estimation. To date, rigorous TPU estimates have been largely lacking from SDB studies. One preliminary effort was conducted to estimate the SISDB uncertainty using a Monte-Carlo method simulation (Pe'eri et al., 2014). However, the Monte-Carlo method is computationally expensive and requires environmental conditions that can be difficult to extend to other procedures and study sites. Another restriction is the dependency on known depths (e.g., control points) to perform the linear regressions. Areas with outdated bathymetric surveys or with no depth data available need to use a different approach to identify potential risks to navigation. Finally, the assumption of constant water column and bottom returns for the radiative transfer equation solution results in biased depth estimations. These types of limitations are the primary focus of the analysis in this dissertation.

1.3 Research Objectives and Dissertation Structure

In recent years, studies have shown the potential use of the SDB method to derive bathymetry at chart datum from satellite imagery. However, several key steps are missing that limited the use of this method as a robust production tool for marine applications.

The overarching goal of this study is to develop a set of tools related to the use of SDB that can provide cartographers and hydrographers an efficient and reliable means to evaluate chart adequacy on outdated survey areas. The study also aims to develop an empirical process for providing bathymetric information in areas where no survey has been conducted, nor where a current or reliable chart is available. By joining image-processing techniques and time-series analysis, this study has three main objectives for using *Landsat 8* imagery as a means for producing SDB.

i. Provide a full estimation of total propagated uncertainty (TPU) when evaluating single-image Satellite-Derived Bathymetry (SDB).
ii. Develop a means to identify the location and behavior of dynamic shallow areas based on multiple-temporal *Landsat 8* imagery.
iii. Enhance the SDB algorithm to include its non-linear form for more accurate depth estimation.

The following is a brief synopsis of the remainder of this dissertation.

Chapter 2 provides a review of previous research related to the use of SDB for meeting hydrographic survey objectives.

Chapter 3 details how TPU can be used to evaluate single-image SDB. Two traditional optimization models for SDB are modified to take into consideration control points (e.g., soundings) vertical uncertainty, by adding a weight matrix to linear regression.

Chapter 4 presents a topological approach for using satellite imagery to identify danger areas to navigation where traditional optimization SDB methods fail due to the lack of usable sounding.

Chapter 5 presents a new SDB optimization method that empirically takes into consideration key physical parameters to estimate depth, including water column, bottom returns, and diffuse attenuation coefficient. In addition, this method shows clusters of bottom returns that enable a means for seafloor discrimination;

Chapter 6 summarizes the combined results of the three study topics, draws some conclusions, and proposes further research areas that could be conducted.

CHAPTER 2

BACKGROUND

Satellite derived bathymetry is a relatively new field that began to be considered as a tool to update navigation charts in the late 1960's (Polcyn and Rollin, 1969). The first *Landsat* satellite, known as Earth Resources Technology Satellite, was launched in 1972. The following year, a study from Polcyn and Lyzenga (1973) evaluated the potential use of *Landsat 1* to map shallow waters. Since then, each new *Landsat* satellite, as well as other orbital platforms, has improved capabilities that enabled its use for ocean applications.

This chapter discusses some of the more important aspects and components of SDB including:

iv. optical properties

v. solar irradiance

vi. water column radiance and diffuse attenuation coefficien

vii. bottom radiance

Also, the two basic procedures used to derive bathymetry are discussed:

i. single image SD

ii. multiple image SDB

2.1 Optical properties

Solar light that penetrates the water and returns to the satellite detectors depends only on the optical properties of the medium (inherent optical properties – IOPs). Absorption coefficient and volume scattering function are the fundamental IOPs (Mobley, 1994). However, it is easier to measure radiometric variables such as the upwelling and down welling plane irradiances that lead to the use of apparent optical properties (AOPs) rather than IOPs to describe the bulk optical properties of water bodies (Mobley, 2004). Apparent optical properties depend both on the medium (i.e., the IOPs) and the geometric (directional) structure of the radiance distribution that display enough regular features and stability to be useful descriptors of a water body. The focus of this study will be on the optical contributions from the water column and the bottom on the solar light where the contributions from the atmosphere and the water surface mediums are considered negligible. Key optical properties (i.e., radiance and diffuse attenuation coefficient) are defined and briefly described in this section. Their relationships with the water column and the bottom will be used throughout the following chapters.

2.1.1 Solar irradiance

The light source that is used in the SDB method is the sun. It's electromagnetic radiation power (i.e., energy per unit time) per unit area is defined as solar irradiance, E_d, with SI units of watts per square meter ($W \cdot m^{-2}$). To calculate the amount of solar irradiance at sea level, the sun is approximated as a black body at 6,000K. The total solar irradiance at top of atmosphere is 1,367 $W \cdot m^{-2}$, which is an average value affected by annual variation of Earth-Sun distance. The Solar

Irradiance at sea level, at visible wavelength, is 522 $W \cdot m^{-2}$, which is 38.2% of the total solar irradiance (Mobley, 1994).

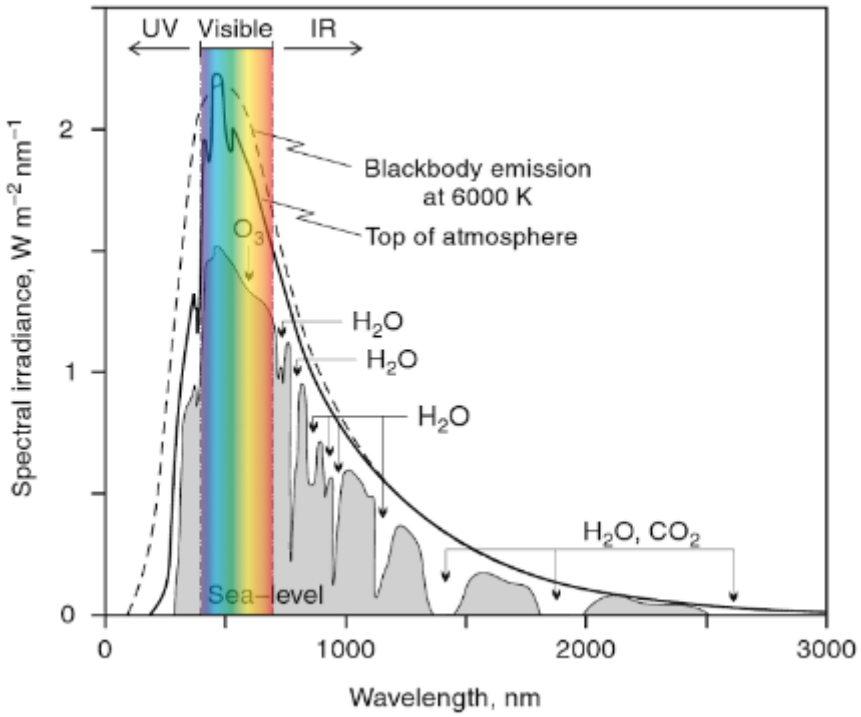

Figure 2.1. Solar irradiance spectrum models for a simulated black body (6000K) above the atmosphere and at sea level (adapted from Lamb and Verlinde, 2011).

2.1.2 Water column radiance and diffuse attenuation coefficient

Imagery sensors, such as cameras and scanners, have a limited field of view. As such, electromagnetic radiation power (i.e., energy per unit time) per unit area received from the interaction of the solar irradiance with a medium within a given solid angle in a specified direction is defined as radiance, $L(\lambda)$, with SI units of watts per square meter ($W \cdot m^{-2}$). As light (e.g., radiances and irradiances) passes through the water (ignoring water surface and bottom boundary

conditions), it decreases exponentially with depth. The coefficient used to describe this light decay is defined as the diffuse attenuation coefficient, $K(\lambda)$. This AOP varies for different water conditions and wavelength (Figure 2.2). Assuming that no losses of the solar irradiance occurred in the atmosphere, then the radiance at a given wavelength, λ_i, collected at the water surface is $L(0, \lambda_i)$. At this point it is possible to calculate the radiance returning from scattering within a given volume of water with a depth of z, $L(z, \lambda_i)$, using Beer's Law (Mobley, 1994) as:

$$L_w(z;\ \lambda_i) = L_w(0;\ \lambda_i) \cdot e^{-K(\lambda_i) \cdot z} \qquad 2.1$$

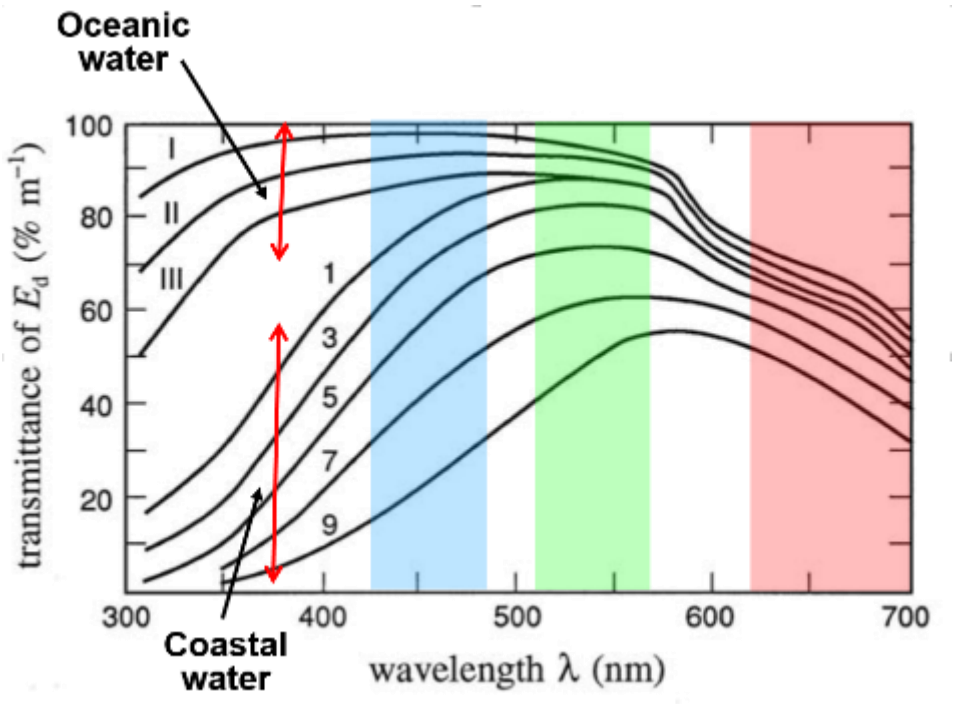

Figure 2.2. Transmittance of light through different water conditions (Jerlov, 1976).

2.1.3 Bottom radiance

In contrast to the multiple studies on water column characteristics during the past 70 years (e.g., Jerlov, 1951; 1976; Preisendorfer, 1976; Mobley, 1994), investigation of underwater bottom characteristics using spectral imagery has been limited. The main reason is that bottom detection is typically only a narrow strip of several hundred meters from the shoreline depending the water quality. Depth penetration of solar light is typically only a few meters up to 30 meters for oceanic water condition. In recent years, there has there been an increase in studies investigating optical remote sensing for bottom mapping, primarily for vegetation and corals. This increase in research is mainly due to the availability of datasets collected from advanced optical systems such as hyperspectral imagery (HSI), and airborne lidar bathymetry (ALB). HSI data is collected from remote sensing platforms (e.g., airborne or satellite). HSI uses large numbers of narrow, contiguous spectral bands (up to 20 nm) that can potentially detect and characterize optical water quality concentrations and vegetation such as colored dissolved organic matter, chlorophyll, suspended matter, macroalgae and seagrass (Brando and Dekker, 2003; Kirkpatrick et al. 2003; Yu et al., 2010; Pe'eri et al., 2016). ALB is an active pulsed laser system that provides water depth and reflectance at 532 nm (Lee and Tuell, 2003). Previous studies have shown the use of ALB to constrain spectral imagery for benthic mapping applications (Tuell and Park 2004; Tuell et al. 2005a; Tuell et al. 2005b; Wang and Philpot, 2007; Park et al. 2010).

The bottom radiance is also used to derive bathymetry. Based on Beer's law, it is possible to relate the observed radiance, $L_{obs}(\lambda_i)$, from an optical sensor to the water depth, z, (Lyzenga, 1978; Philpot, 1989; Philpot and Maritorena et al. 1994):

$$L_{obs}(\lambda_i) = [L_b(\lambda_i) - L_w(\lambda_i)] \cdot e^{-2K(\lambda_i)\cdot z} + L_w(\lambda_i) \quad 2.2$$

$L_b(\lambda_i)$ is the bottom radiance for a single wavelength band and $L_w(\lambda_i)$ is the observed radiance over optically-deep waters with no bottom contribution. It is important to note that this model assumes that the diffuse attenuation coefficient of the upwelling radiance is equal to the diffuse attenuation coefficient of the downwelling radiance. As a result, only a subset of the spectral range from the downwelling irradiance reaches the bottom and is reflected. The optically-deep waters yield optical observations that contain mainly radiance from scattering in the water column while the radiance contribution from the bottom is negligible. The depth limit using satellite-derived bathymetry algorithms is determined by the extinction depth which is the maximum depth that the light can penetrate the water, ($L_{obs}(\lambda_i) \rightarrow L_w(\lambda_i)$). Areas deeper than the extinction depth will show an almost constant value that represents only the water column.

2.2 Single image SDB

2.2.1 Common approaches

Several methods can be used to derive bathymetry based on a single-image approach. Based on descriptions provided by Philpot et al (2004), these include: analytical, optimization and look-up tables.

i. Analytical methods – This approach derives water depth by calculating the attenuation of solar light through the atmospheric and water using radiometric transfer equations. Lyzenga (1978) used an analytical method to formulate a relationship between the radiance observed in imagery to the water depth and

bottom reflectance. His study also developed a radiative transfer model for sun light transmitted into the ocean and reflected back from the bottom to an imagery sensor. Depths are estimated based on a log-linear inversion model where the main assumption is that the bottom type and the water column are uniform. Later, Lyzena also developed a linear model to estimate depths based on pairs of bands from multispectral scanner using LIDAR data as benchmark (Lyzenga, 1985). Thus, multiple parameters are needed to derive bathymetry (e.g., diffuse attenuation for two wavelengths, water column radiance for two wavelengths, bottom radiance for two wavelengths, and control depths). Philpot (1989) expanded Lyzenga's approach, introducing bottom type variability within a scene by presenting a scalar variable sensitive to bottom changes. Lyzenga et al. (2006) presented a sun glint correction algorithm based on near-infrared channel signal, since it presents minimum bottom return, allowing correction to be applied over the whole image without compromising depth correlation on analyzed bands. The model proposed was an update to Lyzenga (1985), and based on multiple linear regression among known depths and spatially equivalent natural logarithms of radiance values (Flener et al., 2012);

ii. Optimization approaches – The optimization approach considers that similar radiometric conditions are observed by images at different wavelength ranges (i.e., bands). Radiometric differences between the two bands are related to optical properties of water. Thus, it is possible solve all but one radiometric parameter simultaneously using a ratio between two bands. Similar to the analytical approach, optimization approaches typically utilize a linear regression by assuming: 1)

optically-homogeneous water conditions, and 2) uniform bottom type. Stumpf et al. (2003) presented a non-linear model to estimate depths by tuning the ratio of natural logarithms of reflectance value from different wavelengths and matching pixels from different bands against chart bathymetry. The method is based on the fact that attenuation of light received by both bands is not equal. When changed into a linear equation, this proposed model also offers improved performance in relatively deep waters. Since bathymetry is extracted based on benchmark soundings, it will have the same vertical datum as the chart or the one used to reduce the survey depths (Pe'eri et al., 2014). Vanderstraete et al. (2006) presented a multi-temporal, multi-sensor approach to detect changes on coastal area using Lyzenga (1978) approach to estimate water column correction. Su et al. (2008) enhanced Stumpf et al. (2003) method by using Levenberg-Marquardt optimization to deal with the non-linear inversion. Kanno et al. (2011) proposed a semi-parametric regression model by combining Lyzenga et al. (2006) with spatial interpolation. This method is intended to be used to increase bathymetric spatial resolution or to fill data gaps. Pe'eri et al. (2014) proposed a workflow for SDB products, whereby chart datum was used as an invariant vertical reference along imagery due to sensor rapid acquisition process, and not sensitive to tidal variations along its pixels. This is accomplished by the translation factor present at Stumpf et al. (2003) which accounts for tidal differences between chart soundings and imagery acquisition;

iii. Look-up tables (LUT) – This supervised classification approach consists on creating a database of remote sensing reflectance spectra based on radiometric

calculation of the interaction of solar light spectrum with different bottom and water types at different depths. Then, each pixel reflectance spectrum from available imagery is compared against created database spectrum. Using least-squares approach, the minimum discrepancy between imagery and database is selected, providing the environmental conditions at each pixel. Louchard et al. (2003) presented a simulated bathymetric library (e.g., look-up tables) of remote sensing reflectance spectra for depths up to 20 m. Bramante et al. (2013) compared the three methods based on a modified Lyzenga et al (2006) model, Stumpf et al. (2003) and Louchard et al. (2003).

2.2.2 SDB band-ratio procedure

In the remote sensing of optically-shallow coastal waters, a typical multispectral sensor contains several channels. Each chanel captures a broad spectral range (70 to 150 nm wide) that collectively spans the visible through the infrared portions of the electromagnetic spectrum. Light transmittance through the water column varies as a function of wavelength. The solar irradiance that is able to penetrate seawater to appreciable depths is typically between 350 nm (ultraviolet-blue) and 700 nm (red), depending on the water clarity and the water depth (Jerlov 1976; Mobley 2004). Sunlight at wavelengths greater than 700 nm (i.e., near infrared) has very low transmittance in seawater (Parrish, 2013).

According to equation 2.2, both the optical property values of the water column and the seafloor are needed to derive the bathymetry:

$$z = -\frac{1}{2K} \cdot ln\left(\frac{\mathrm{L_{obs}}\,(\lambda_i) - L_w(\lambda_i)}{L_b(\lambda_i) - L_w(\lambda_i)}\right) \qquad 2.3$$

However, the requirements for Lyzenga's (1978, 1985) inversion approach (i.e., an analytical method) presented over a complex environment with multiple seafloor types, and the potential accuracy required to calculate the diffuse attenuation coefficient do not meet the available resources for this study. Instead, a ratio transform approach that utilizes two bands to reduce the number of parameters required is used to estimate depth (Stumpf et al. 2003). Based on the assumption that the water column is uniformly mixed, the ratio of two bands will maintain a near-constant attenuation value that is the difference of the diffuse attenuation coefficient values of the two different wavelengths. Dierssen et al. (2003) used a log-difference concept to derive bathymetry in turbid waters. He determined thata strong absorption in the Red band and a relatively weak absorption in the Green band will produce a ratio that is correlated with the bathymetry. The results showed a linear relationship between the green/red (555 nm/ 670 nm) ratio and single-beam echosounder depth measurements, where the gain, m_1, and offset, m_0, are empirically determined:

$$z = m_1 \cdot \left[ln(\mathrm{L_{obs}}(\lambda_i)) - ln\big(\mathrm{L_{obs}}(\lambda_j)\big)\right] + m_0 = m_1 \cdot ln\left(\frac{\mathrm{L_{obs}}\,(\lambda_i)}{\mathrm{L_{obs}}(\lambda_j)}\right) + m_0 \qquad 2.4$$

Stumpf et al. (2003) used a log-ratio approach with Blue and Green bands. Typically, in coastal conditions, light in the green wavelengths (500 to 600 nm) is absorbed with depth faster than blue wavelengths (400 to 500 nm) (Jerlov 1976). The Stumpf et al. (2003) algorithm can remove the errors associated with varying albedo in the atmosphere, water column, and the seafloor since both

bands are affected similarly. Accordingly, the change in ratio between bands is affected more by depth than by bottom albedo (Stumpf et al. 2003). Depth can then be derived using the following equation, where the gain and offset are again empirically determined, as in the Dierssen's approach:

$$z = m_1 \left(\frac{ln(\mathrm{L_{obs}}(\lambda_i))}{ln(\mathrm{L_{obs}}(\lambda_j))} \right) + m_0 \qquad 2.5$$

It is important to note that the linear transform approach has challenges when trying to obtain accurate values for the water column and the seafloor optical properties (Philpot, 1989). A loosely constrained model can fail to provide accurate depth values when the simplified assumptions (e.g., homogeneity of water column parameters) are not satisfied. In this study, only the ratio transform algorithms were evaluated since the ratio-transform algorithms require fewer constants and no optical properties to determine bathymetry.

Key steps in the satellite-derived procedure include (Pe'eri et al., 2014):

i. Pre-processing – Satellite imagery is downloaded based on the geographic location and environmental conditions (e.g., cloud coverage and sun glint) had to be used;
ii. Spatial filtering – 'Speckle noise' in the Landsat imagery is removed using spatial filtering;
iii. Water separation – Dry land and most of the clouds are removed;
iv. Identifying the extinction depth – The optical depth limit for one to infer bathymetry (also known as, the extinction depth) is calculated;
v. Applying the bathymetry algorithm – The bathymetry is calculated using the Stumpf et al. (2003) algorithm on the blue and green bands;

vi. Vertical referencing – A statistical analysis between the algorithm values to the chart soundings references the Digital Elevation Model (DEM) to the chart datum.

A detailed discussion on the SDB procedure is provided in Chapter 4.

Vertical referencing of the SDB model to chart datum includes three sub-steps: selection of control soundings, determination of the extinction depth and vertical transformation of the SDB model. First step is to select reliable control soundings, ideally from a recent survey (ALB or acoustic). The reference soundings should be selected over areas in which the charted seafloor morphology shows visual correspondence with the algorithm result. Additional soundings may be selected from the chart over optically-deep waters (i.e., seafloor morphology cannot be recognized in the algorithm result) in order to determine the extinction depth. Next, the algorithm model results are compared to the control soundings at coincident points. The averaged values of the SDB model are plotted against the control point soundings (Pe'eri et al., 2014). It enables discriminate areas where the seafloor contributes to the recorded pixel values (i.e., optically-shallow areas) from those areas where contributions are only from water color and suspended particulates (i.e., optically-deep areas). Based on a visual inspection of the depth measurements, other depth boundaries were also determined (Figure 2.3). Areas shallower than the extinction depth show a linear relationship between the reference bathymetry and the algorithm results. Areas deeper than the extinction depth do not show a clear correlation between the reference bathymetry and the algorithm results, and will break from the linear trend of the optically-shallow waters. A regression analysis was used to indicate the linearity between the datasets. The calculated parameters in the regression analysis included r^2 (the coefficient of determination), gain, and offset. Based on the highest correlation (r^2 closest to 1), the best procedure configuration was selected.

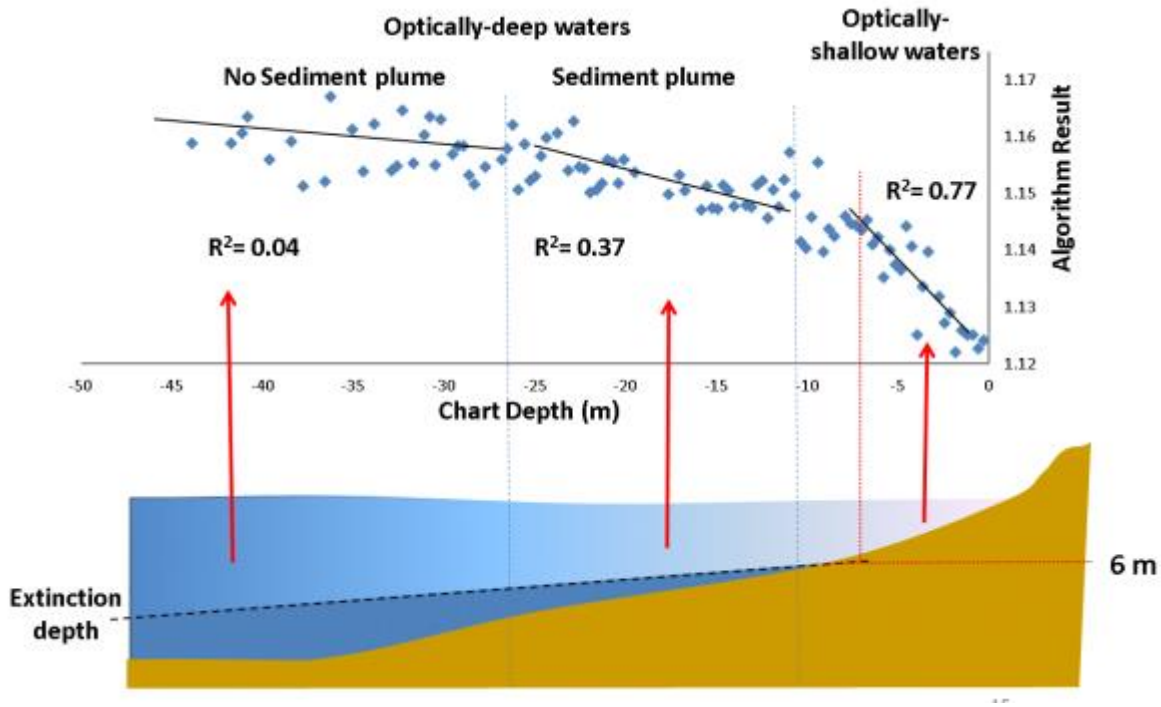

Figure 2.3. A schematic illustration of the statistical analysis using the blue-green Stumpf et al. (2003) algorithm against ALB survey data over a study site in Cape Ann, MA (Pe'eri et al., 2014). Top part of the image shows the scatter plot of the algorithms results as a function of the chart sounding (MLLW). The bottom part of the image provides a possible explanation for the algorithm results and their relation to the depth of extinction.

2.3 Multiple-image approach

Most of the studies related to multiple satellite images used a set of images from a single-image approach over a time duration for monitoring a particular seafloor feature (e.g., coral reef habitats). Multi-temporal change detection on coral reefs has been described by Zainal et al. (1993), Andréfouët et al. (2001), Dustan et al. (2001), Matsunaga et al. (2001), Palandro et al. (2003) and LeDrew et al. (2004). These studies were primarily related to coral reefs classification,

and not bathymetry. Vanderstraete et al. (2006) presented a multi-temporal multi-sensor approach to detect changes on coastal areas. Pe'eri et al. (2015) presented the use of multiple satellite imagery to determine regions that were not influenced by turbidity. By evaluating the difference between image pairs, it was possible to determine areas with minimum depth differences. Those areas were assumed to contain clear waters. Assuming that turbidity is constantly changing, areas subject to its interference will present different depths based on its respective SDB. It was noticed that areas considered clear presented highest correlation to charted depths. To harmonize radiometric distributions received by two images (i.e., relative to the same area) at different epochs, a histogram equalization model was presented. Also, since the method aims to derive depths based on minimum difference of SDB, final product would result in a mosaic where overlapping areas are integrated by averaging depths. Tidal effects are taken into account based on the use of chart soundings as control points (Pe'eri et al., 2014). SDB multiple-image approach is based on the same processing concepts used in a SDB single-image approach.

CHAPTER 3

APPLYING TOTAL PROPAGATED UNCERTAINTY (TPU) TO SINGLE-IMAGE SATELLITE-DERIVED BATHYMETRY

3.1 Introduction

Single-Image Satellite Derived Bathymetry (SISDB) is a remote sensing technique whereby multi-spectral imagery is processed by combining the underwater physical properties of the satellite bands (characterized by different wavelength ranges), and correlate these bands to known depths. This relatively new approach has been used by hydrographic offices and researchers to derive shallow-water bathymetry, and as a means of hydrographic survey reconnaissance (Lyzenga, 1978; Dierssen et al., 2003; Stumpf et al., 2003; Philpot et al., 2004; Lyzenga, et al. 2006; Pe'eri et al., 2014). The revisit cycles and global coverage of multi-spectral satellite imagery enable a cost-effective alternative for obtaining near-shore bathymetry in areas in which traditional surveying (e.g., ship-based acoustic surveying or Airborne Lidar Bathymetry) is infeasible due to limited resources, and logistical or safety constraints. Landsat imagery is commonly used for SISDB because it is publicly-available through the U.S. Geological Survey (USGS) Earth Explorer website (http://earthexplorer.usgs.gov/). In particular, *Landsat 8* (L8) imagery presents a higher image quality and has become recognized as a useful means to obtain nearshore bathymetry (Pe'eri et al., 2016).

Using simplified radiative transfer equations (Philpot, 1989; Lyzenga et al., 2006), it is possible to relate imagery radiance from the water column and bottom to the water depth. To establish a correlation between observed radiance (e.g., imagery pixel values) and the water depth,

most SISDB algorithms use an optimization approach (Philpot et al., 2004; Lyzenga, et al., 2006). Typically, the optimization approach is in the form of a ratio of the logarithms of the blue and green bands (Stumpf et al., 2003). Assuming that the turbidity in the water column is uniform, this ratio algorithm output is expected to vary linearly with depth (Lyzenga, 1978 ; Philpot et al., 2004; Lyzenga, et al., 2006). Survey soundings from smooth-sheets (i.e., fair-sheets), or survey data that is tidally-referenced can be used as ground truth to linearly transform the log ratio into meaningful depths referenced to chart datum. There is no need to measure the tide height during the image acquisition because the determination of the transformation parameters from the tidally-referenced control points automatically accounts for the tide (Pe'eri et al. 2014). Differences in water levels are usually well approximated as a vertical offset and do not impair the linear relationship between chart control points and ratio algorithm output. Therefore, the procedure eliminates the need for either tide-coordinated imagery or tide correctors.

Most research on SISDB has focused on the algorithms that are used to derive bathymetry. Typically, the performance of SISDB algorithms is evaluated by comparing the algorithm's results against a reference data set of higher accuracy (e.g., Liceaga-Correa and Euan-Avila, 2002; Kanno et al., 2011; Bramante et al., 2013; Flener et al., 2013; Su et al. 2014). The International Hydrographic Organization (IHO) develops and publishes Standards for Hydrographic Surveys S-44 (IHO, 2008) that regulate the conduct of hydrographic surveys required to produce or update nautical charts. According to IHO S-44 publication, all survey related uncertainties should be addressed when producing an estimation of the total propagated uncertainty (TPU).

To date, rigorous TPU estimates have been largely lacking from SISDB studies. A preliminary effort was conducted to estimate the SISDB uncertainty using a Monte-Carlo method simulation (Pe'eri et al., 2014). However, the Monte-Carlo method is computationally expensive

and requires environmental conditions that can be difficult to extend to other procedures and study sites.

The main objective of this research project is to present an improved TPU estimation that is based on the two most common optimization approaches (Dierssen et al., 2003 and Stumpf et al., 2003). Different SISDB model depth and corresponding uncertainties are compared against ground truth (i.e., recent surveys). Several parameters were tested, including various types of filters, kernel sizes, number of control points and their coverage, and recent versus outdated control points.

This study revisits the SIDSDB procedure first described in Pe'eri et al. (2014), and generates a full TPU model based on the uncertainty contributions throughout the SISDB procedure. The Dierssen and Stumpf SISDB algorithms were evaluated in this study. Using Mathcad Prime 3.1 (http://www.ptc.com), L8 imagery was used to evaluate SISDB algorithms using linear regression to relate the control points and L8 channels ratio. Bathymetry models and uncertainty values were generated for two sites along the East Coast of the United States: Ft. Myers, FL, and northern Cape Ann, MA. Two control points datasets were used for the vertical transformation: 1) Airborne Lidar Bathymetry (ALB) with a small position uncertainty (i.e., sub-meter accuracy), and 2) charted depth soundings shown on a NOAA nautical chart. However, since the scale of the chart is 1:40,000, there are some inherent limitations in using the charted sounding as quality control points. This includes relatively few soundings per unit area, and each sounding having large degree of positional uncertainty (i.e., > 1 m vertically and >10 m horizontally). In this regard, the difference between SISDB derived depths based on chart soundings and SISDB derived depths based on ALB data calibration points was computed to verify if the derived soundings were within the vertical uncertainty, assuming a confidence level of 90% (CL90).

3.2 SISDB Procedure

The relationship between the observed radiance in satellite imagery above shallow-water environment can be expressed using a simplified solution to radiative transfer equation (Philpot, 1989; Lyzenga et al., 2006):

$$L_{obs}(\lambda) = (L_b(\lambda) - L_w(\lambda))e^{-2K(\lambda)\cdot z} + L_w(\lambda) \quad 3.1$$

Where $L_b(\lambda)$ is the bottom radiance, $L_w(\lambda)$ the radiance scattered from the water column (no bottom contribution), $K(\lambda)$ the diffuse attenuation coefficient and z is depth.

The exponential attenuation of light through the water column is wavelength dependent (Figure 3.1). Wavelengths greater than 0.85 μm typically do not penetrate more than a few mm of the water surface (Parrish, 2013). For most water cases, the diffuse attenuation coefficient values of the blue (around 0.4 - 0.5 μm) and green (around 0.5 - 0.6 μm) wavelengths are on the same order of magnitude (Fig. 3.1). The diffuse attenuation coefficient value of the near infrared (NIR) band (> 0.85 μm) is larger by two orders of magnitude (Jerlov, 1961; Smith and Baker, 1981). In the absence of specular water surface reflections, water in the NIR band will typically be manifest through very low digital numbers (i.e., dark pixels), in comparison to the adjacent land,especially in the case of beaches composed of sand and vegetation that reflect strongly in the NIR. It is possible to avoid specular water surface reflections by selecting scenes acquired with advantageous solar illumination ray-path geometry with respect to satellite sensor and the water-surface target, as described at Mahiny and Turner, 2007.

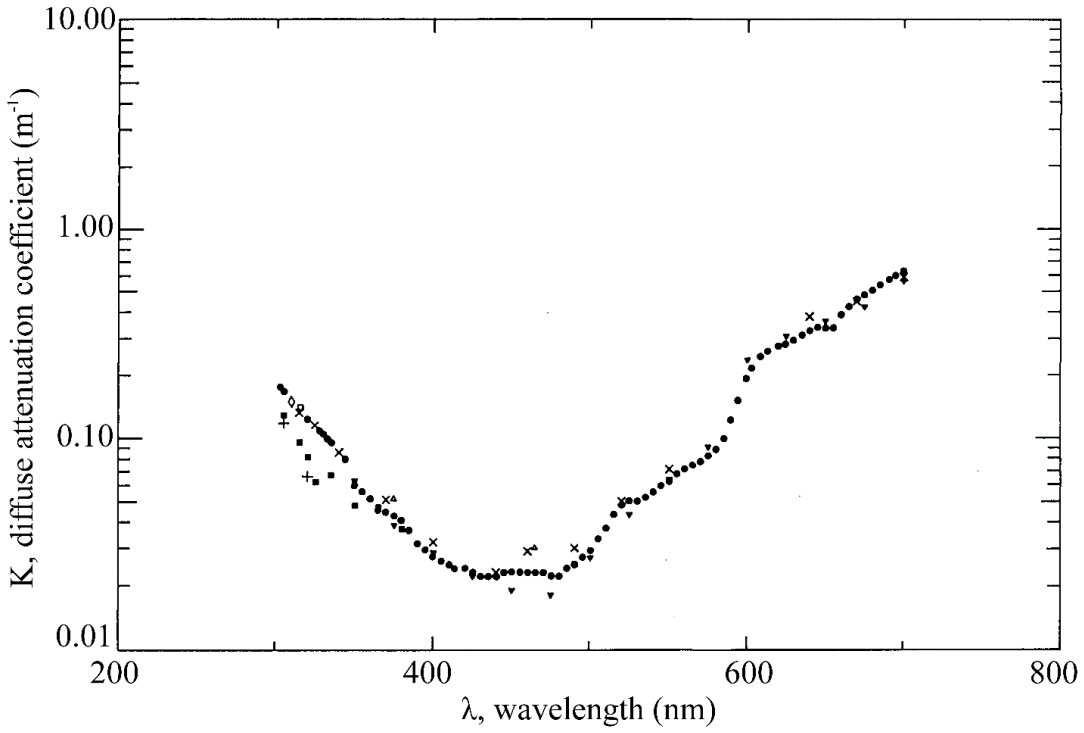

Figure 3.1. Diffuse attenuation coefficient as a function of wavelength for open-ocean conditions (Smith and Baker, 1981).

There are different approaches available to calculate SISDB including analytical methods (Lyzenga 1978; Philpot 1989; Lyzenga et al. 2006; Frener et al., 2012), optimization approaches (Dierssen et al. 2003; Stumpf et al. 2003; Vanderstraete et al., 2006; Su et al. 2014), and look-up-table approaches (Louchard et al. 2003; Bramante et al. 2013). In this study a sub-category of the optimization approach was used based on a band ratio. The radiance values of the blue and green bands are typically used in the band-ratio algorithms.

The two most commonly used band-ratio optimization algorithms are those developed by Dierssen et al. (2003) that models the difference between observed radiance log values and Stumpf et al. (2003) that uses the division between the observed radiance log values of the Blue (B) band $L_{obs}\,(\lambda_B)$ and the Green (G) band, $L_{obs}\,(\lambda_G)$. SISDB determination will depend on a scaling

coefficient (based on the diffuse attenuation coefficient), m_0, and a translation coefficient (based on bottom return and diffuse attenuation coefficient), m_1. These parameter values are presented at Dierssen's algorithm (Dierssen et al., 2003):

$$z = m_0 \cdot ln\left(\frac{L_{obs}\,(\lambda_B)}{L_{obs}(\lambda_G)}\right) + m_1 \qquad 3.2$$

Stumpf's algorithm (Stumpf et al., 2003) presents a slightly different model using a ratio of the observed radiance log values:

$$z = m_0 \left(\frac{ln(L_{obs}(\lambda_B))}{ln(L_{obs}(\lambda_G))}\right) + m_1 \qquad 3.3$$

Both band ratio algorithms provide reasonable results for hydrographic reconnaissance (Pe'eri et al., 2014). The key steps in the SISDB procedure include: filtering, land/water separation, and vertical transformation. In this study, determination of the extinction depth (i.e., the depth limit for bottom detection using the satellite imagery) is considered as an initial, sub-step of the vertical transformation. Extinction depth was 8 m for both study sites. In certain instances, other types of pre-processing steps could be performed, including sun-glint removal, cloud removal, atmospheric correction, or radiometric calibration. However, these pre-processing steps are beyond the scope of this research project, and were not investigated.

3.2.1 De-noising

Based on a recent report by Czapla-Myers et al (2015), the signal-to-noise ratio (SNR) of L8 radiance imagery acquired by the Operational Land Imager can be often eight times higher than imagery acquired by *Landsat 7* (L7) using the Enhanced Thematic Mapper Plus. This was caused by the radiometric quality of L7 being degraded after May, 2003, following a Scan Line Corrector error. The horizontal accuracy of L8 was also improved from 50 m at 90% confidence interval (L7) to 12 m at 90% confidence interval (Storey et al., 2014). The L8 imagery is available to the user in Universal Transverse Mercator (UTM) projected coordinates, and is referenced to the WGS 84 (G872) datum. In addition to the limited dynamic range of 8 bit in L7 imagery, a type of 'speckle noise' was present in all bands. In particular, the green band contained additional radiometric noise that is referred to 'wave noise' (Vogelmann et al. 2001; Pe'eri et al., 2015). L8 imagery contains 12-bit information stretched to a 16-bit dynamic range. Although the noise in the L8 imagery is significantly lower than that of L7 imagery, some noise and striping artefacts has been observed in the datasets. According to the USGS Earth Resources Observation Systems (EROS) Data Center (Thomas Adamson, personal communication, 2015), the striping is due to: 1) per-detector relative gain estimates; 2) individual detector instabilities; and 3) slight differences between each detector's linearity.

Due to these limitations, only recent L8 imagery (from 2015) with cloud cover lower than 5% was used for this study. The imagery was loaded into Mathcad Prime 3.1 as matrices using Geospatial Data Abstraction Library (GDAL) to transform the image files into ASCII format, since *Mathcad* was down sampling the 16-bit images to 8-bits when using its image reading tools. In order to enhance the image quality, spatial domain filters were applied in the pre-processing step. Four different types of spatial filters with kernel sizes of 3×3 and 5×5 were evaluated: average,

median, 2D adaptive Wiener and Gaussian low-pass (Gonzalez and Woods, 2017). From the four filters, the spatial domain Gaussian low-pass filter and average filter were chosen based on Signal-to-Noise Ratio (SNR) analysis using the kernel's mean, μ, and standard deviation, σ (Brüllmann and d'Hoedt, 2011):

$$SNR = 20log\left(\frac{\mu}{\sigma}\right) \quad 3.4$$

$\frac{1}{16}\begin{pmatrix}1 & 2 & 1\\ 2 & 4 & 2\\ 1 & 2 & 1\end{pmatrix}$ Gaussian low-pass kernel 3x3	$\frac{1}{9}\begin{pmatrix}1 & 1 & 1\\ 1 & 1 & 1\\ 1 & 1 & 1\end{pmatrix}$ Average kernel 3x3
$\frac{1}{256}\begin{pmatrix}1 & 4 & 6 & 4 & 1\\ 4 & 16 & 24 & 16 & 4\\ 6 & 24 & 36 & 24 & 6\\ 4 & 16 & 24 & 16 & 4\\ 1 & 4 & 6 & 4 & 1\end{pmatrix}$ Gaussian low-pass kernel 5x5	$\frac{1}{25}\begin{pmatrix}1 & 1 & 1 & 1 & 1\\ 1 & 1 & 1 & 1 & 1\\ 1 & 1 & 1 & 1 & 1\\ 1 & 1 & 1 & 1 & 1\\ 1 & 1 & 1 & 1 & 1\end{pmatrix}$ Average kernel 5x5
Figure 3.2. Spatial domain filter kernels.	

3.2.2 Water Separation

Water body areas were separated from land areas based on the spatially filtered blue and green bands (i.e., Bands 2 and 3 in L8). A shortwave infrared (IR) band (Band 6 in L8) was used as a spatial condition to mask the land from visible bands and extract the water bodies. This land/water separation was done using the Normalized Difference Water Index (NDWI, as in

McFeeters, 1996, Gao, 1996, Ji et al., 2009 and McFeeters, 2013) IR band, $L_{obs}\,(\lambda_{IR})$ and Red band, $L_{obs}\,(\lambda_R)$, using:

$$NDWI = \frac{L_{obs}\,(\lambda_R) - L_{obs}\,(\lambda_{IR})}{L_{obs}\,(\lambda_R) + L_{obs}\,(\lambda_{IR})} \qquad 3.5$$

As mentioned previously, water in the IR band will typically have very low digital numbers in comparison to the adjacent land. As shown in Figure 3.3, water pixels will typically be characterized by lower IR-band pixel values in comparison to Red-band pixel values. On the other hand, land pixels will typically be characterized by higher IR-band pixel values in comparison to Red-band pixel values. As a result, water masses would have positive NDWI values.

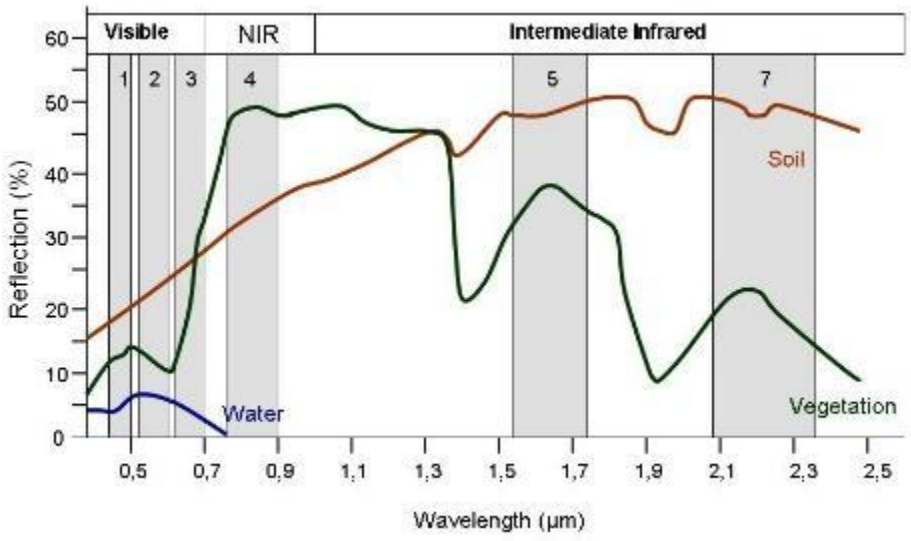

Figure 3.3. Spectral characteristics of water, soil and vegetation in the visible and IR range (based on Gao, 1996).

3.2.3 Vertical transformation

A vertical transformation is established between the log ratio values and chart datum using control points from a reference dataset that are referenced to the same datum used for the navigational chart (Pe'eri et al., 2014). It is important to note that the spatial distribution and spot spacing density (i.e., measurements per unit area) of the control points varies between survey locations. The main reason for this difference is the suitability of the available data that can be used as control points. Whenever possible, it recommended to use the soundings contained on the SS that contain a denser spot spacing compared to nautical chart soundings. SS will potentially provide a stronger statistical solution. However, even SS soundings typically contain an average spot spacing that ranges from tens to hundreds of meters (i.e., not all pixels in the Landsat imagery will contain a sounding). In cases where surveys are available (e.g., ALB or MBES), the horizontal point spacing of the survey data (< 3 m) is usually an order of magnitude smaller than the image resolution (30 m for L8 imagery). In this type of situation, it is necessary to statistically reduce the number of control points by using common sampling techniques (Cochran, 1977). In this study, the horizontal Root Mean Square Error ($RMSE_H$) values provided in the *Landsat* Metadata (MTL) files from L8 imagery were used to sample the ALB and SS datasets (Figure 3.4). A geo-statistical averaging was applied to depth measurements in reducing them to a single value per image pixel to calculate the associated uncertainty value. Soundings average calculation disregarded depths that were considered near the pixel border, based on the horizontal uncertainty values at L8 metadata (Figure 3.4).

To evaluate the contribution of positioning quality of the control points on the vertical transformation, the same amount/position of ALB measurements and SS soundings were used as control points in this study. The adjustment metric was based on the L_2-norm between down-

sampled spatial resolution control points and estimated depths. The relationship between the distributions of the control points within the study site to the vertical transformation was also evaluated using control points covering 25%, 50% and 100% of the whole study area. For the vertical transformation, it is assumed that a linear dependency between the SISDB model and the control points (i.e., a linear regression) can be applied to the SISDB model within the optically-shallow waters.

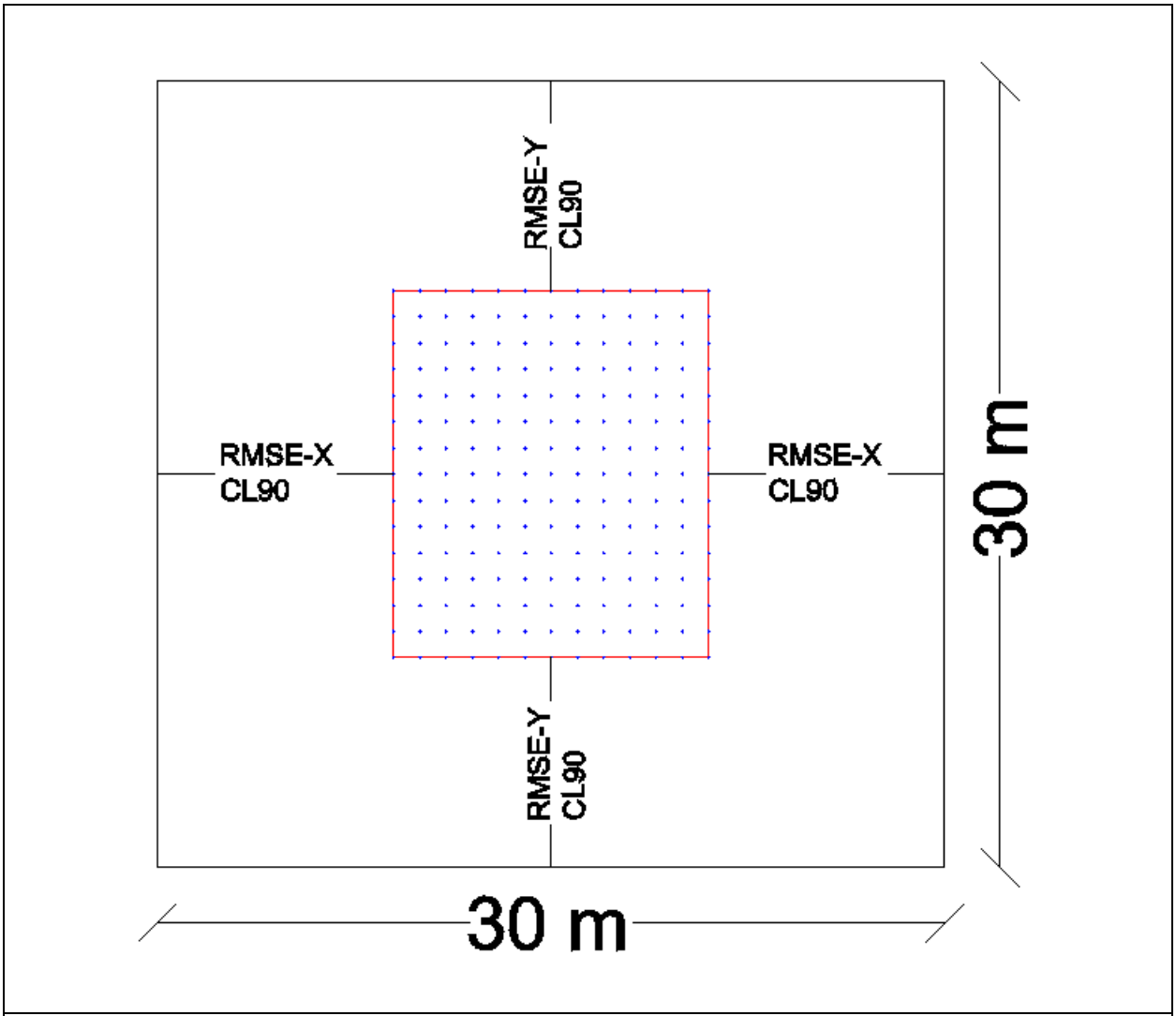

Figure 3.4. ALB selected soundings within a L8 pixel, used to estimate the most probable value of depth related to that pixel.

Based on equation 3.1, band ratio algorithms have linear behavior if $L_w(\lambda_B) \approx 0$ and $L_w(\lambda_G) \approx 0$ (Dierssen et al., 2003; Stumpf et al., 2003). Accordingly, both Dierssen's and Stumpf's SISDB band-ratio algorithms (Equations 3.2 and 3.3) can be described using an affine form. In order to calculate the scaling coefficient, m_0, and a translation coefficient, m_1 for both algorithms, a linear regression approach is used to match n-values of depth measurements, L, against n-values of the corresponding SISDB pixel values log ratio that are present in the first column of the Jacobian matrix $A_{D,S}(\lambda_B, \lambda_G)$:

$$V_{D,S} = A_{D,S}(\lambda_B, \lambda_G) \cdot X_{D,S} - L \qquad 3.6$$

Where $V_{D,S}$ is the residual vector for Dierssen's and Stumf's linear regression, $A_D(\lambda_B, \lambda_G) = \begin{pmatrix} ln\left(\frac{L_{obs}(\lambda_B)_0}{L_{obs}(\lambda_G)_0}\right) & 1 \\ \vdots & \vdots \\ ln\left(\frac{L_{obs}(\lambda_B)_{n-1}}{L_{obs}(\lambda_G)_{n-1}}\right) & 1 \end{pmatrix}$, $A_S(\lambda_B, \lambda_G) = \begin{pmatrix} \frac{ln(L_{obs}(\lambda_B)_0)}{ln(L_{obs}(\lambda_G)_0)} & 1 \\ \vdots & \vdots \\ \frac{ln(L_{obs}(\lambda_B)_{n-1})}{ln(L_{obs}(\lambda_G)_{n-1})} & 1 \end{pmatrix}$, $X_{D,S} = \begin{pmatrix} m_0 \\ m_1 \end{pmatrix}$; and $L = \begin{pmatrix} z_0 \\ \vdots \\ z_{n-1} \end{pmatrix}$

Linear regression was applied to transform imagery log ratio into depths using ALB or SS control points. A weight matrix W, based on the uncertainty of sound selection procedure (Figure 3.4), was defined to balance the adjustment. The linear regression itself is fitted using a Least Squares Method (LSM, Mikhail, 1976; Vaníček, 1995), where ${V_{D,S}}^T \cdot W \cdot V_{D,S} = min$, and:

$$X_{D,S} = \left({A_{D,S}}^T \cdot W \cdot A_{D,S}\right)^{-1} \cdot \left({A_{D,S}}^T \cdot W \cdot L\right) \qquad 3.7$$

Where $W = \begin{pmatrix} 1/{\sigma_{z_0}}^2 & \dots & 0 \\ \vdots & \ddots & \vdots \\ 0 & \dots & 1/{\sigma_{z_{n-1}}}^2 \end{pmatrix}$

After a solution is provided from the linear regression (3.7), it is possible to calculate the residuals vector, $V_{D,S}$, and subsequently the root mean square error, $RMSE_{D,S}$:

$$RMSE_{D,S} = \sqrt{\frac{{V_{D,S}}^T V_{D,S}}{n-2}} \tag{3.8}$$

When using a large number of control points from either a survey dataset (e.g., ALB or MBES), the processing time required to calculate the vertical transformation will increase because of the calculations associated to using a weight matrix. Since weight matrix is a diagonal matrix, it is possible to optimize the processing time by calculating the sums for the $X_{D,S}$ solution vector. This optimized calculation of weight matrix is also useful for vertical uncertainty propagation. The solution of the parametric linear adjustment matrices in Equation 3.7 can be defined by a set of coefficients:

$${A_{D,S}}^T W A_{D,S} = \begin{pmatrix} C_5 & C_3 \\ C_3 & C_1 \end{pmatrix} \tag{3.9}$$

$${A_{D,S}}^T W L = \begin{pmatrix} C_2 \\ C_4 \end{pmatrix} \tag{3.10}$$

Where $C_1 = \sum_{k=0}^{n-1} \frac{1}{{\sigma_k}^2} = \sum_{k=0}^{n-1} {W_k}^2$; $C_2 = \sum_{k=0}^{n-1} A_{D,S_{k,0}} L_k {W_k}^2$; $C_3 = \sum_{k=0}^{n-1} A_{D,S_{k,0}} {W_k}^2$; $C_4 = \sum_{k=0}^{n-1} L_k {W_k}^2$; and $C_5 = \sum_{k=0}^{n-1} {A_{D,S_{k,0}}}^2 {W_k}^2$.

Accordingly, depth estimations for Dierssen ($\hat{Z}_{D_{i,j}}$) and Stumpf ($\hat{Z}_{S_{i,j}}$) are described by:

$$\hat{Z}_{D_{i,j}} = \frac{ln\left(\frac{L_{obs}(\lambda_B)_{i,j}}{L_{obs}(\lambda_G)_{i,j}}\right) \cdot (C_1C_2 - C_3C_4) + (C_5C_4 - C_3C_2)}{C_1C_5 - (C_3)^2} \quad 3.12$$

$$\hat{Z}_{S_{i,j}} = \frac{\frac{ln\left(L_{obs}(\lambda_B)_{i,j}\right)}{ln\left(L_{obs}(\lambda_G)_{i,j}\right)} \cdot (C_1C_2 - C_3C_4) + (C_5C_4 - C_3C_2)}{C_1C_5 - (C_3)^2} \quad 3.13$$

Where i, j stands for the rows and columns of the satellite image

3.3 Total propagated uncertainty

IHO S-44, contains guidelines on quality definitions for hydrographic surveys that are considered necessary for safety-of-navigation (IHO, 2008). More specifically, IHO S-44 states that "*All components and their combination must be capable of providing data to the required standard*." The combination of all the components (both random and systematic) is defined as the total propagated uncertainty (TPU). Assuming that the horizontal and vertical components of the TPU are independent from each other, it is common practice to describe the TPU using the total horizontal uncertainty (THU) and the total vertical uncertainty (TVU). In the case of SISDB analysis, the THU will be strictly dependent on imagery horizontal uncertainty. Calibration information that predict the horizontal uncertainty of the imagery are available within metadata

files distributed with L8 imagery. TVU of SISDB will be calculated in this study by analyzing uncertainties related to satellite imagery, as well as available control points (soundings). Since both the horizontal and vertical components are assumed to have null covariance, TPU will be determined by the quadratic summation of THU and TPU. Also, the survey quality that produces the control point will affect the uncertainty estimation.

3.3.1 Total horizontal uncertainty

No horizontal transformation is performed along SDB depth estimation. As such, the horizontal uncertainty in the SISDB procedure is the same as the horizontal uncertainly of the L8 imagery. According to the *Landsat 8 Data Users Handbook* (USGS, 2016), L8 imagery is referenced to WGS84, projected in UTM, and has a reported horizontal accuracy of 12 m at 90% confidence level (CL90). Image-to-image registration was conducted by the USGS that verified horizontal accuracies of pixel locations of L8 imagery are well within the 12 m CL90 specification (Storey et al., 2014). The x and y RMSE components described in metadata (MTL) files are quadratic summed to achieve THU and is also limited by 12 m CL90 specification.

3.3.2 Total vertical uncertainty (TVU) components

Based SISDB procedure described in section 3.2.3, the two key properties that contribute to the total vertical uncertainty (TVU) include: 1) uncertainty related to the radiometric characteristics of the satellite imagery and filtering process; and 2) uncertainty related to the quality

of the control points. It was assumed that the uncertainties of the two key properties are independent, and can be approximated as Gaussian variables.

3.3.2.1 Radiometric uncertainty

As previously confirmed by Mishra et al. (2014) and Czapla-Myers et al. (2015), the radiometric uncertainty design specification for L8 imagery is ±5%. Using the values of the kernels described in Figure 3.2, the radiometric uncertainty of the satellite imagery after using spatial domain filter kernel, *H*, can be calculated as:

$$\sigma_{L_{obs}} = \sqrt{\sum\sum\left[\left(5\% \cdot H_{i,j} \cdot P_{i,j}\right)^2\right]} \qquad 3.14$$

Where $H_{i,j}$ are values of filter kernel constituents, as described in Figure 3.2 and $P_{i,j}$ represent image pixel values within the window (same dimensions as H).

3.3.2.2 Water and bottom optical properties

The diffuse attenuation coefficient, $k(\lambda)$, constrains the effective depth penetration of sunlight into the water (Mishra et al, 2005, Equation 3.1). The optical properties of the bottom may also affect this result, based on the optical characteristics of the bottom that may absorb part of the energy of the incident solar light (Philpot et al., 2004). In the case of SISDB, the optical characteristics of the bottom are assumed uniform and scattering from the water column is very

small. As such, water column contribution for the observed radiance is assumed to be negligible. Also, bottom radiance for two different bands (i.e., $L_b(\lambda_2)$ and $L_b(\lambda_1)$) are assumed as constant.

3.3.2.3 Control points

National Hydrographic offices collect hydrographic survey data based on the requirements contained in IHO S-44 publication. ALB or acoustic surveying in shallow waters (typically, < 40 m) have relatively uniform spot spacing and uncertainty. SS data or chart sounding represent a subset of all compiled surveys in each area that employ an intentional bias toward shoal areas (i.e., the charted depth is often purposefully taken to represent the shallowest measured depth in each area). Typically, uncertainty of SS data is approximated according to maximum allowable uncertainty (Table 3.1). Because the IHO S-44 requires accuracy with a 95% Confidence Interval rather than the 90% used by NASA to report on the image quality, the results are based on the IHO S-44 standard. As such, a distinction will be made using 95% Confidence Interval (95% CI).

Survey order	Maximum allowable TVU (95% CI)	Maximum allowable THU (95% CI)
Special Order	a = 0.25 m b = 0.0075	2 m
Order 1a/1b	a = 0. 5 m b = 0.013	5 m + 5% of depth
Order 2	a = 1.0 m b = 0.023	20 m + 10% of depth

Table 3.1. IHO S-44 maximum allowable uncertainties according to IHO S-44 survey standards, where the maximum allowable TVU is calculated using $\pm\sqrt{a^2 + (b * depth)^2}$ (IHO, 2008).

3.3.3 Total vertical uncertainty (TVU) solution

The resulting SISDB TVU is primarily dependent on the radiometric uncertainty of each of L8 bands, and the maximum allowable uncertainty of the control points. It is important to note that the radiometric values of the bands used to calculate the uncertainty (i.e., $L_{\mathrm{obs}}(\lambda_{\mathrm{B}})_k$ and $L_{\mathrm{obs}}(\lambda_{\mathrm{G}})_k$) are sampled from the images by using a spatial filter kernel. Depending on the chosen SISDB model, the uncertainty estimation is constrained to column 0 values of the Jacobian matrix ($\sigma_{\mathrm{A_{D,S_{k,0}}}}$):

$$\sigma_{\mathrm{A_{D_{k,0}}}} = \sqrt{\left(\frac{\sigma_{\mathrm{L_{obs}(\lambda_B)_k}}}{\mathrm{L_{obs}(\lambda_B)_k}}\right)^2 + \left(\frac{\sigma_{\mathrm{L_{obs}(\lambda_G)_k}}}{\mathrm{L_{obs}(\lambda_G)_k}}\right)^2} \qquad 3.15$$

$$\sigma_{\mathrm{A_{S_{k,0}}}} = \sqrt{\left(\frac{\sigma_{\mathrm{L_{obs}(\lambda_B)_k}}}{\mathrm{L_{obs}(\lambda_B)_k \cdot \ln(L_{obs}(\lambda_G)_k)}}\right)^2 + \left(\frac{\sigma_{\mathrm{L_{obs}(\lambda_G)_k}} \cdot \ln(\mathrm{L_{obs}(\lambda_B)_k})}{\mathrm{L_{obs}(\lambda_G)_k \cdot \left(\ln(L_{obs}(\lambda_G)_k)\right)^2}}\right)^2} \qquad 3.16$$

The TVU solution of the SISDB was calculated combining partial derivatives (of equations 3.12 and 3.13) to its variables uncertainties. The uncertainties reported in the metadata were used as the control point uncertainties, σ_{L_k}, of the SS soundings and for the ALB data in the study. The model uncertainties, $\sigma_{A_{D,S_{k,0}}}$, for Dierssen's linear regression and Stumpf's linear regression are defined in equations 3.15 and 3.16. As a result, the TVU per pixel is:

$$TVU_{i,j} =$$

$$= \sqrt{\left(\frac{(C_1C_2 - C_3C_4)\sigma_{A_{D,S_{i,j}}}}{C_1C_5 - (C_3)^2}\right)^2 + A_{D,S}{}^2_{i,j}(R_{1a} + R_{2a}) + 2A_{D,S_{i,j}}(R_{1b} + R_{2b}) + R_{1c} + R_{2c}} \qquad 3.17$$

Where

$\mathrm{A_{D}}_{i,j} = ln\left(\frac{L_{obs}(\lambda_B)_{i,j}}{L_{obs}(\lambda_G)_{i,j}}\right)$; $\mathrm{A_{S}}_{i,j} = \frac{ln(L_{obs}(\lambda_B)_{i,j})}{ln(L_{obs}(\lambda_G)_{i,j})}$;

$\mathrm{R_{1a}} = \sum_{\mathrm{k=0}}^{\mathrm{n-1}}\left\{\left(\sigma_{A_{D,S_{\mathrm{k,0}}}} \cdot \mathrm{W_k}\right)^2\left[\frac{\mathrm{C_1L_k - C_4}}{\mathrm{C_1C_5 - (C_3)^2}} - \frac{2(\mathrm{C_1C_2 - C_3C_4})\left(\mathrm{C_1}A_{D,S_{\mathrm{k,0}}} - \mathrm{C_3}\right)}{(\mathrm{C_1C_5 - (C_3)^2})^2}\right]^2\right\}$;

$\mathrm{R_{1b}} = \sum\left\{\left(\sigma_{A_{D,S_{\mathrm{k,0}}}} \cdot \mathrm{W_k}\right)^2\left\{\left[\left(\frac{\mathrm{C_1L_k - C_4}}{\mathrm{C_1C_5 - (C_3)^2}} - \frac{2(\mathrm{C_1C_2 - C_3C_4})\left(\mathrm{C_1}A_{D,S_{\mathrm{k,0}}} - \mathrm{C_3}\right)}{(\mathrm{C_1C_5 - (C_3)^2})^2}\right)\right] \cdot \left[\left(\frac{\mathrm{-C_2 - C_3L_k + 2C_4}A_{D,S_{\mathrm{k,0}}}}{\mathrm{C_1C_5 - (C_3)^2}} - \frac{2(\mathrm{C_5C_4 - C_3C_2})\left(\mathrm{C_1}A_{D,S_{\mathrm{k,0}}} - \mathrm{C_3}\right)}{(\mathrm{C_1C_5 - (C_3)^2})^2}\right)\right]\right\}\right\}$;

$\mathrm{R_{1c}} = \sum\left\{\left(\sigma_{A_{D,S_{\mathrm{k,0}}}} \cdot \mathrm{W_k}\right)^2\left[\left(\frac{\mathrm{C_1L_k - C_4}}{\mathrm{C_1C_5 - (C_3)^2}} - \frac{2(\mathrm{C_1C_2 - C_3C_4})\left(\mathrm{C_1}A_{D,S_{\mathrm{k,0}}} - \mathrm{C_3}\right)}{(\mathrm{C_1C_5 - (C_3)^2})^2}\right)\right]^2\right\}$;

$\mathrm{R_{2a}} = \sum\left\{\left(\sigma_{\mathrm{L_k}} \cdot \mathrm{W_k}\right)^2\left[\frac{\mathrm{C_1}A_{D,S_{\mathrm{k,0}}} - \mathrm{C_3}}{\mathrm{C_1C_5 - (C_3)^2}}\right]^2\right\}$;

$\mathrm{R_{2b}} = \sum\left\{\left(\sigma_{\mathrm{L_k}} \cdot \mathrm{W_k}\right)^2\left[\frac{(\mathrm{-C_3A_{k,0} + C_5})\left(\mathrm{C_1}A_{D,S_{\mathrm{k,0}}} - \mathrm{C_3}\right)}{(\mathrm{C_1C_5 - (C_3)^2})^2}\right]\right\}$; and

$\mathrm{R_{2c}} = \sum\left\{\left(\sigma_{\mathrm{L_k}} \cdot \mathrm{W_k}\right)^2\left[\frac{\mathrm{-C_3}A_{D,S_{\mathrm{k,0}}} + \mathrm{C_5}}{\mathrm{C_1C_5 - (C_3)^2}}\right]^2\right\}$

3.3.4 TVU verification

Reducing point spacing ALB and SS datasets, as well as only using matching soundings from both datasets resulted on not using a large portion of down-sampled ALB data. For instance, depth and TVU were calculated at Cape Ann study site, using Dierssen's model, with 399 control points. The residual amount of averaged ALB data was 5,740 points. Those points, which were not used on the adjustment, were used to validate TVU values. Estimated soundings and their correspondent uncertainties at CI95 were evaluated against those points. The averaged ALB depths should lie inside the estimated depth uncertainty boundaries. If so, TVU for the specific estimated depth is considered valid. Ideally, the number of depths with valid TVU is greater than 95%.

3.4 Results

Bathymetry of two study sites (Cape Ann, MA and Ft. Myers, FL, Figures 3.5 and 3.6) was derived through linear regression using Dierssens's and Stumpf's affine form algorithms. SS soundings and ALB measurement were used as control points for the vertical referencing (Table 3.2). As described above, the number of ALB and SS measurements were reduced to match L8 spatial resolution. Three dataset of control points were generated based on the amount of coverage over the study area (i.e., 25%, 50% and 100% of the whole area). Depth estimation of pixels not used on adjustment was restricted to log ratio range used to calculate linear regression parameters. Control points derived from ALB and SS were evaluated in terms of SISDB and TVU (Figure 3.7). In addition to the control point datasets, a third dataset was generated from ALB measurement as a reference dataset to evaluate the performance of the weighted SISDB algorithm. The reason to use ALB measurements as the reference "ground truth" was because of their high vertical accuracy

(<0.25 m). Finally, the contribution of the radiometric enhancement using two types of normalized filters (Average and Gaussian low-pass) with kernel sizes of 3×3 and 5×5.

Data	Details	Ft. Myers, FL	Cape Ann, MA
L8	Acquisition date	2015-03-17	2014-10-12
	Cloud coverage (%)	1.38	3.15
	Map projection	UTM-17N	UTM-19N
	Horizontal datum	WGS84	WGS84
ALB	Survey agency	USACE	USACE
	Acquisition year	2010	2014
	Grid resolution	1 m	1 m
	Vertical datum	MLLW	MLLW
SS	Survey agency	NOAA	NOAA
	Survey ID	H08194, H08195, H08196, H08358, H08362, H08363	H08095, H08096
	Acquisition year	1957, 1960, 1959, 1957, 1960, 1961	1954, 1954
	Vertical datum	MLLW	MLLW

Table 3.2. Study sites dataset description.

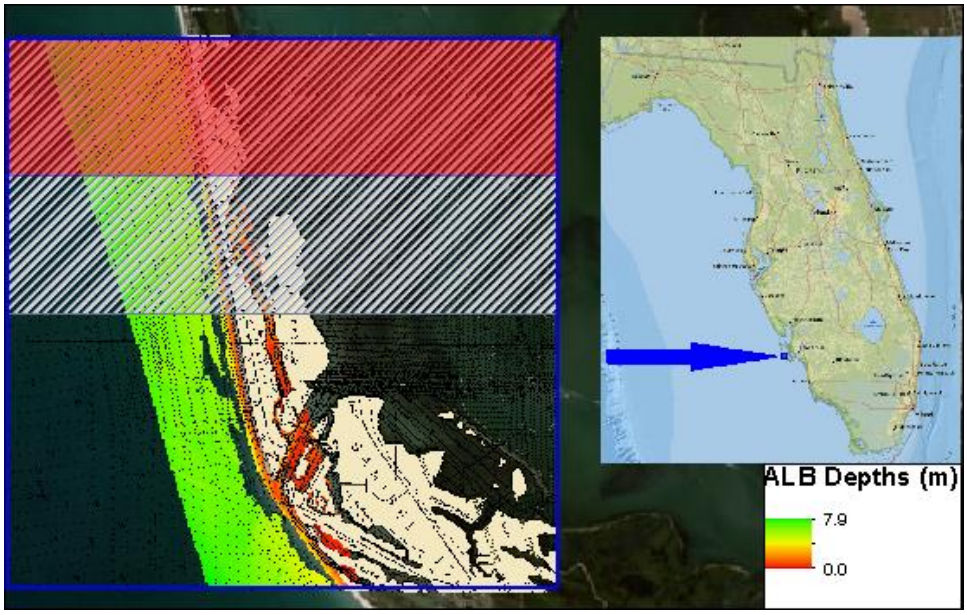

Figure 3.5. Fort Myers (FL) site, including with the coverage area of the three control point datasets: 25% (red box), 50% (gray box) and 100% (hollow blue box).

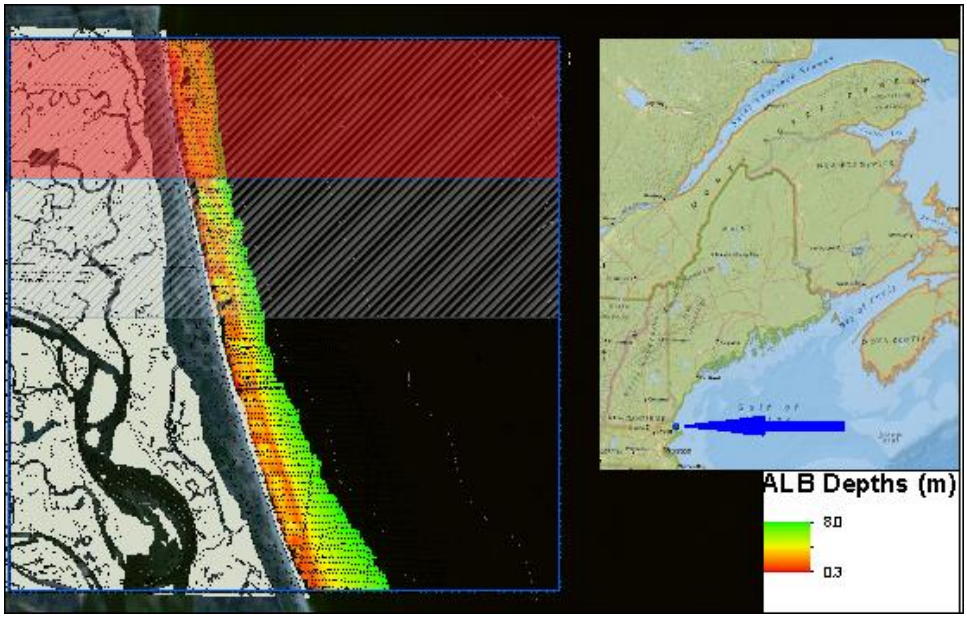

Figure 3.6. Cape Ann (MA) site, including with the coverage area of the three control point datasets: 25% (red box), 50% (gray box) and 100% (hollow blue box).

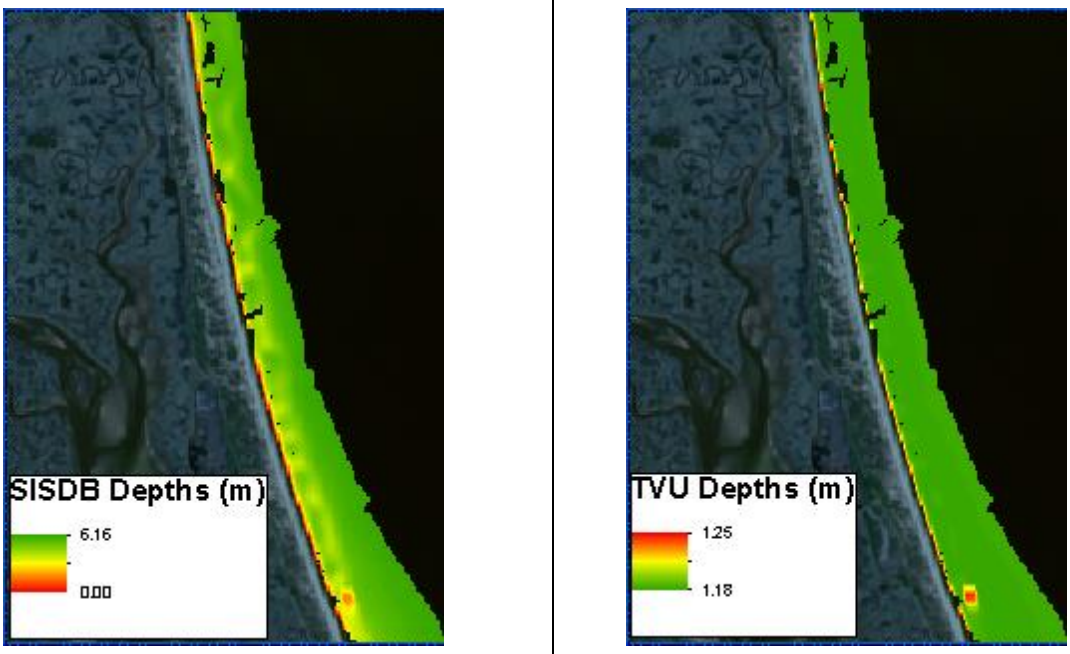

(a) (b)

Figure 3.7. Both images are based on Dierssen's model, using a 5x5 kernel average filter, with ALB control points (100% of study area) at Cape Ann. (a) shows depth estimation for SISDB and (b) displays TVU values calculated for each estimated sounding.

Overall, the study results using the Dierssen's and Stumpf models for the SISDB produced similar depths and uncertainties (Figure 3.8). Due to models' agreement, only Stump's model will be presented. TVU values for Cape Ann ranged from 0.92 to 2.75 m (1 Sigma), depending on the filter and number of control points. For Fort Myers, TVU ranged from 0.75 to 1.80 m. Although different kernels may present lower TVU values, this uncertainty enhancement seems to be artificial and is not reflected when validating TVU estimations.

SS and ALB depths were down sampled to L8 spatial resolution, associating one pixel to one averaged depth. Matching down sampled ALB and SS data composed two control points datasets. The remaining down sampled ALB depths (blue points, Figure 3.8) were used to check

TVU estimations. TVU validation calculated the percentage of blue points (ALB) sitting inside the boundaries of depths estimations and its associated uncertainty – showed as "Predicted".

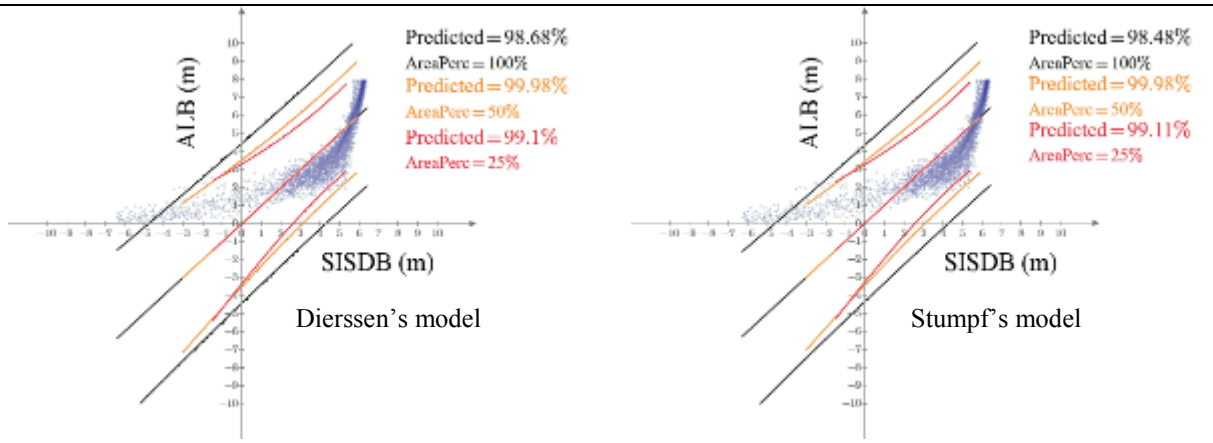

Figure 3.8. Study result using over Cape Ann, MA, using SS control points and 3x3 average filter: using Dierssen's model (at left) and Stumpf's (at right). Blue points represent depths derived from ALB averaging, not used in linear regressions. The line passing through (0,0) is SISDB depth estimation. The upper and lower lines represent depth's TVU at CI95. Predicted percentages show the agreement between estimated TVU, and the difference between estimated depths and ALB data for 25%, 50% and 100% SS control points.

Fort Myers study area showed significant problems in the TVU validation, primarily when using SS control points associated to a 5x5 average filter (Figure 3.10). On the other hand, Cape Ann presented no major problems when comparing estimated TVU to the difference between estimated depths and ALB reduced data (Figure 3.9).

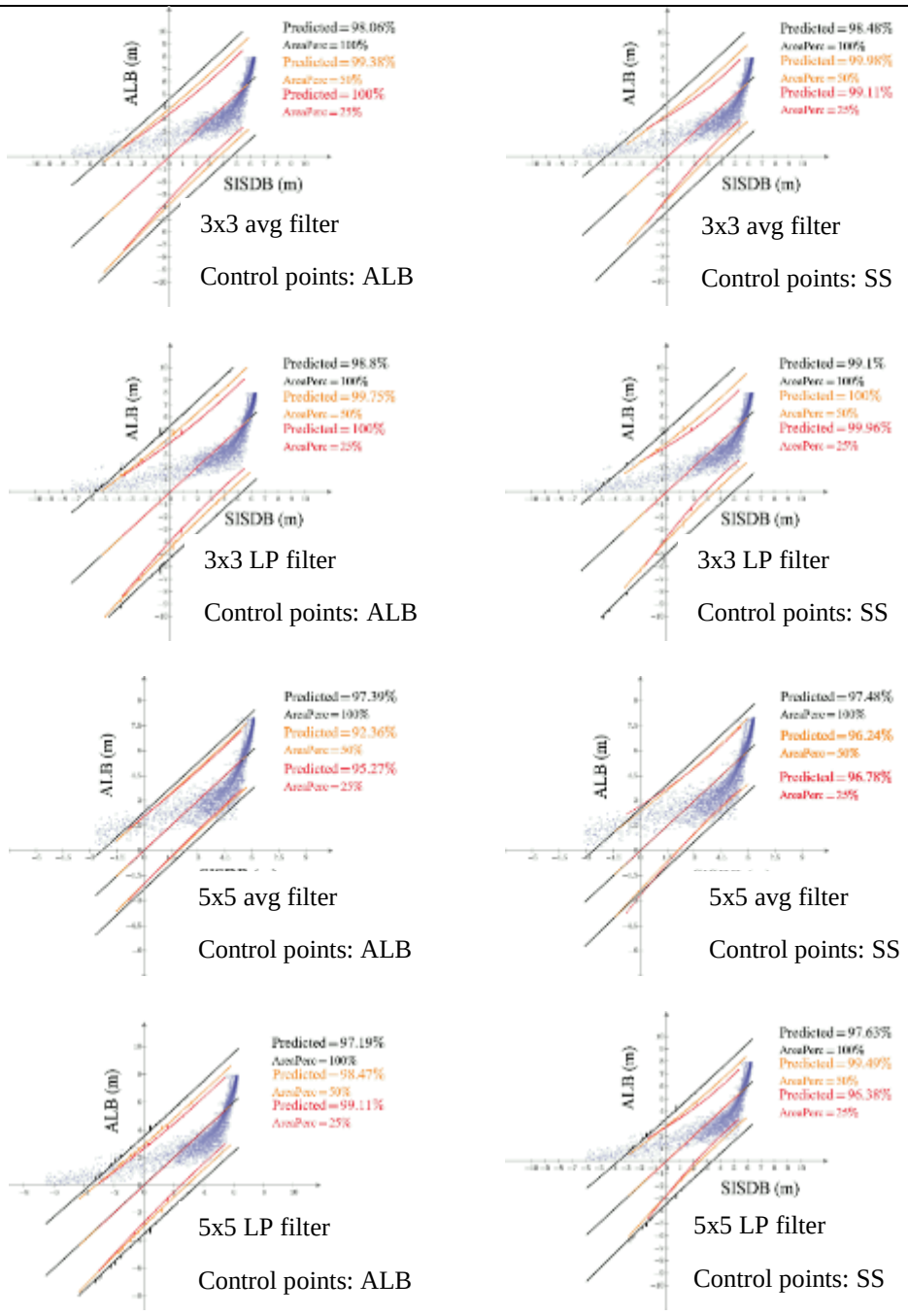

Figure 3.9. Cape Ann, MA, estimated depths and uncertainties compared against averaged ALB depths (blue points, not used for linear regression).

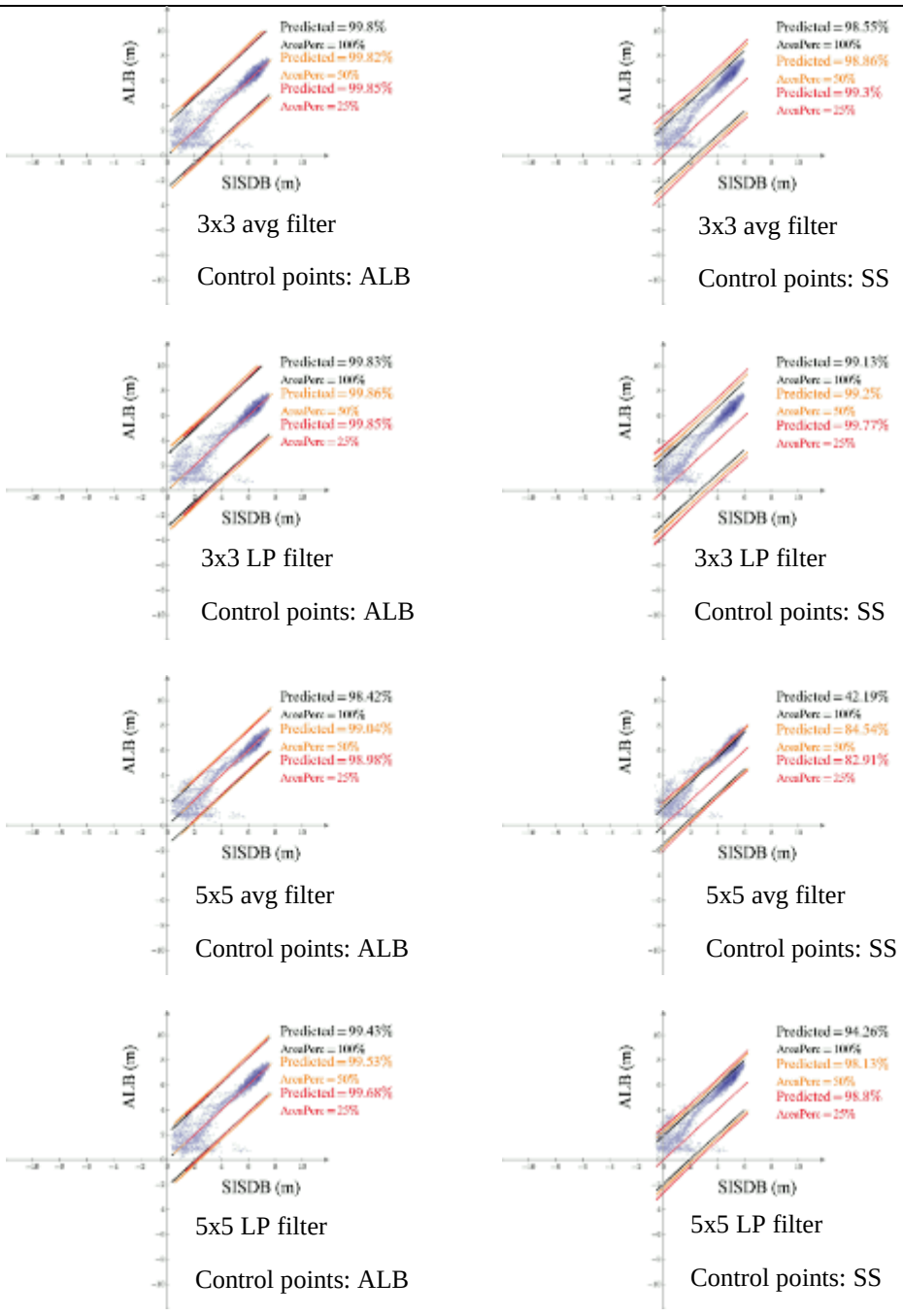

Figure 3.10. Fort Myers, FL, estimated depths and uncertainties compared against averaged ALB depths (blue points, not used for linear regression).

3.5 Discussion

The analysis of TVU model indicates it is primarily dependent on the quality of the satellite imagery. Regardless of the algorithm structure, the log ratio, or difference of logs, there is an observed dependence between the vertical uncertainty and scaling coefficient to the radiometric uncertainty of the imagery. An additional improvement would be to use a non-linear model to estimate bathymetry. Such model would consider non-uniform water column and bottom conditions.

Another crucial factor is the temporal component. As time increases between the collection date of the control point and the acquisition of the satellite imagery, currents and strong weather events can change the bathymetry within the area of interest over time. Ideally, the survey can be conducted shortly before the acquisition time of the satellite imagery that is used in the SISDB procedure. For example, the use of a single-beam echo sounder immediately before satellite imagery is available (typically, two weeks) can provide a cost-efficient solution with a TVU on a sub-meter level. This assumption can be verified when analyzing the estimated depths and TVU validation on Figures 3.9 and 3.10. Cape Ann presents the almost the same results for ALB and SS estimation, even though SS data was collected in the 1950's. Depth trend line matches blues points on both ALB and SS regressions, and indicates a stable area. Fort Myers is the opposite. This area has experienced strong storms during the past 60 years (e.g. hurricanes Donna, 1960, Gordon, 1994, Gabrielle, 2001 and Charley, 2004 – Ingargiola et al., 2013). Although most of Fort Myers TVU validation (Figure 3.10) showed good percentages, depth trend line (central) is apart from blue points which are translated to the upper TVU line. This problem is aggravated when using the 5x5 average filter. But, it is important to note that it is present in all the other regressions

using SS control points. The reduced ALB control points indicate the solution. As previously stated, using a few updated survey points (such as SBES) would largely benefit SISDB and its TVU.

The significance of the proposed uncertainty approach is that there is no need for an operator to find optically-deep water area within the image (Pe'eri et al. 2014). Previous work for estimating the SISDB uncertainty used a Monte-Carlo simulation depended on the sample size extracted from the image, and on random variables to converge to a stable error estimation. Also, the processing time required for this approach is significantly shorter since only one calculation is needed rather than multiple iterations necessary for the Monte Carlo approach. Potentially, there may be some benefit in further reducing the processing time. If so, Equation 3.17 could be simplified:

$$TVU_{i,j} \approx 1.11 \frac{(C_1 C_2 - C_3 C_4)\sigma_{A_{D,S_{i,j}}}}{C_1 C_5 - (C_3)^2} = 1.11 m_0 \sigma_{A_{D,S_{i,j}}} \qquad 3.18$$

CHAPTER 4

CHANGE DETECTION OF DYNAMIC SHALLOW AREAS OCCURRING IN RIVER ENTRANCES USING MULTIPLE LANDSAT 8 IMAGERY

4.1 Introduction

Conducting hydrographic surveys on navigable rivers is a challenging but necessary effort for Hydrographic Offices (HOs). Some of the more important challenges include dynamic fluctuations in river flow and sediment transport. In turn, this can cause significant changes in water levels, depth areas, sediment types, and obstructions to safe navigation. Typically, HOs perform traditional hydrographic surveys in river entrances using single-beam echo sounders (SBES), multibeam echo sounders (MBES), or airborne LiDAR bathymetry (ALB). The type of equipment used is influenced by many factors, including by depth range, water clarity, time-frame, and budget. Despite the importance of keeping nautical charts updated in the entrances of navigable rivers where dynamic changes are occurring, many Hydrographic Offices do not have the resources to conduct frequent hydrographic surveys. An additional challenge occurs where hydrographic surveys are needed in remote areas. SBES, MBES, and ALB surveys all require crews on site, logistical arrangements, and significant investments in time and effort. These types of constraints often result in long periods of time between surveys. As a result, the existing nautical charts often do not reflect the present conditions, and may not be suitable for ensuring safe and efficient maritime navigation.

Although satellite-derived bathymetry (SDB) provides bathymetric datasets at a coarser spatial resolution, and are less accurate compared to traditional hydrographic surveys, it provides

continuously repeating coverage over the same area. Satellite imagery, such as *Landsat* and *Sentinel*, are publicly available at no cost, although have some constraints caused by cloud coverage and sun glint. As a result, it is possible to generate a multi-temporal analysis using a SDB approach. Each SDB imagery dataset provides a snapshot in time of shallow-water bathymetry. Changes in the bathymetry can be identified by making a comparison between scenes acquired at different times over the same area. Identifying and mapping the morphological changes and correlating them with reference benchmarks can provide valuable information for hydrographers, cartographers, and coastal managers in terms that mariners often wonder: "What has changed?"

A number of studies have been conducted on estimating bathymetry from SDB single imagery (Pe'eri et al., 2014, Pe'eri et al., 2013, Flener et al., 2012, Bramante et al., 2013, Su et al.). More recent papers discussed the use of multiple-image analysis on SDB to enhance the final product (Pe'eri et al., 2016, Pe'eri et al., 2014). The major drawback for these types of approaches is that calibration points (i.e., soundings from previous surveys) are needed to estimate bathymetry from SDB. This can be a significant challenge in highly dynamic environments where depth soundings are outdated or non-existent. Another challenge associated with mapping SDB variations occurs when extracted features of dynamic changes over time present complex topological variations. This can make it difficult to identify displacement vectors.

Delineation of a feature using multiple satellite imagery from different platforms, however, is not a straightforward task. After limiting the satellite imagery to near cloud-free conditions (e.g., less than 10%), there may be some areas that will have only one useful image per year, or per several years. In addition, historical images from different platforms (i.e., *Landsat 7, 5 or 4*) are characterized with a low dynamic range (8-bit) and radiometric noise that poses difficulties when a semi-automatic approach is used (e.g., the processing algorithms are guided by the operator).

The feature analysis over time enables several outcomes: 1) identifies the location of stable areas versus dynamic areas, 2) assesses the impact of major weather events that affected the seafloor (e.g., hurricanes), and 3) enhances the use of the single-image SDB approach. The goal of this portion of the research is to describe the use of SDB for charting dynamic features.

A change detection process using image processing was developed to identify the location and movement of dynamic shallow areas in riverine environments. Two river entrances were evaluated as study sites using multiple satellite imagery scenes from current (i.e., *Landsat 8*) and legacy Landsat imagery (i.e., *Landsat 7, 5 or 4*) imagery over time: Yukon River (USA) and Amazon River (Brazil). The time-series analysis developed in this study was used to identify probable shallow areas on both sites. In particular, the process described does not require the use of charted soundings as calibration points for SDB. This is important since the most recent survey of the entrance the Amazon River was in 1997, while the the last survey of the Yukon River site was in 1899.

4.2 Feature extraction using SDB

4.2.1 SDB process

The SDB procedure to derive reconnaissance bathymetry is already used for chart updates over remote and dynamic locations (Kampia et al., 2016; Pe'eri et al., 2016; Tournay and Quéméneur, 2013). By assuming uniform conditions for the water column and the bottom, it is possible to solve the depth parameter, *z*, by calculating a log ratio between two satellite bands, typically the blue and green bands. In this study, a SDB ratio model was utilized (Pe'eri et al.,

2014) that included the following steps: (1) radiometric enhancement, (2) dry-land removal, and (3) calculation of the SDB ratio model. It is important to note that control points are not available for conducting a vertical reference of the SDB ratio model to chart datum. Instead, feature extraction and analysis was conducted directly from the SDB ratio model.

4.2.1.1 Radiometric enhancement

Landsat 8 is the most recent platform of the Landsat satellites that provides to the publicly-available satellite imagery at no cost. *Landsat 8* imagery contains 12-bit information stretched to a 16-bit dynamic range. The signal-to-noise ratio radiometric performance using an Operational Land Imager is as much as eight times higher than its predecessor, *Landsat 7* using the *Enhanced Thematic Mapper Plus* (Czapla-Myers et al., 2015). This difference in image quality can affect the comparison images analyzed from *Landsat 8* to satellite images acquired from *Landsat 7* or earlier platforms that are limited dynamic range of 8 bit. In addition, all satellite imagery contains some degree of radiometric noise (e.g., speckle noise, banding or striping). As part of the pre-processing, a 3X3 Gaussian low-pass kernel was applied on all the satellite imagery that was used in the study:

$$\frac{1}{16}\begin{pmatrix} 1 & 2 & 1 \\ 2 & 4 & 2 \\ 1 & 2 & 1 \end{pmatrix} \qquad 4.1$$

4.2.1.2 Dry-land removal

Water body areas were separated from land areas using shortwave infrared (IR) band $L_{obs}\ (\lambda_{IR})$ and Red (R) band, $L_{obs}\ (\lambda_R)$, as a spatial condition to mask dry land areas from visible bands and extract the water bodies. This land/water separation was performed using a Normalized Difference Water Index (NDWI) following (McFeeters, 1996, Gao, 1996, Ji et al., 2009 and McFeeters, 2013):

$$NDWI = \frac{\mathrm{L_{obs}}\ (\lambda_R) - \mathrm{L_{obs}}\ (\lambda_{IR})}{\mathrm{L_{obs}}\ (\lambda_R) + \mathrm{L_{obs}}\ (\lambda_{IR})} \qquad 4.2$$

If NDWI values are positive, they are considered as water area pixels.

4.2.1.3 Calculation of the SDB ratio model

For this study, assuming homogeneous turbid waters, a SDB ratio model was calculated using a log ratio between the Green (G) band $L_{obs}\ (\lambda_G)$ and the Red (R) band, $L_{obs}\ (\lambda_R)$, (Dierssen et al., 2003):

$$z = m_0 \cdot ln\left(\frac{L_{obs}\ (\lambda_G)}{L_{obs}(\lambda_R)}\right) + m_1 \qquad 4.3$$

Since no updated soundings were available in the study areas, the SDB ratio model was not vertically transformed to chart datum and remained in image space. As such the scaling coefficient (i.e., based on the diffuse attenuation coefficient) was equal to one, $m_0 = 1$, and the translation coefficient was equal to zero, m_1=0.

4.2.2 Feature extraction

Shallow-area structures were identified by using an edge-detection algorithm on log ratio imagery. Canny edge-detection (Canny, 1986), based on Mathcad 3.1 Prime internal function "*canny*", presented good results on creating boundaries around shallow features.

Only the features of interest were selected from the Canny edge detection results on the SDB ratio model. Other less obvious features were removed manually (Figure 4.1, left image). To overcome the complexity of the shoal feature's shape, a well-defined topological feature was used generalize Canny edge detection results. Constraints for the well-defined topological feature were selected as "extreme points" (Figure 4.1, yellow points in the right image). Having the list of pixel coordinates, its extreme limits were defined by maximum and minimum E, N. All points that had, at least, one coordinate matching such limits were used to compose the yellow points (Figure 4.1).

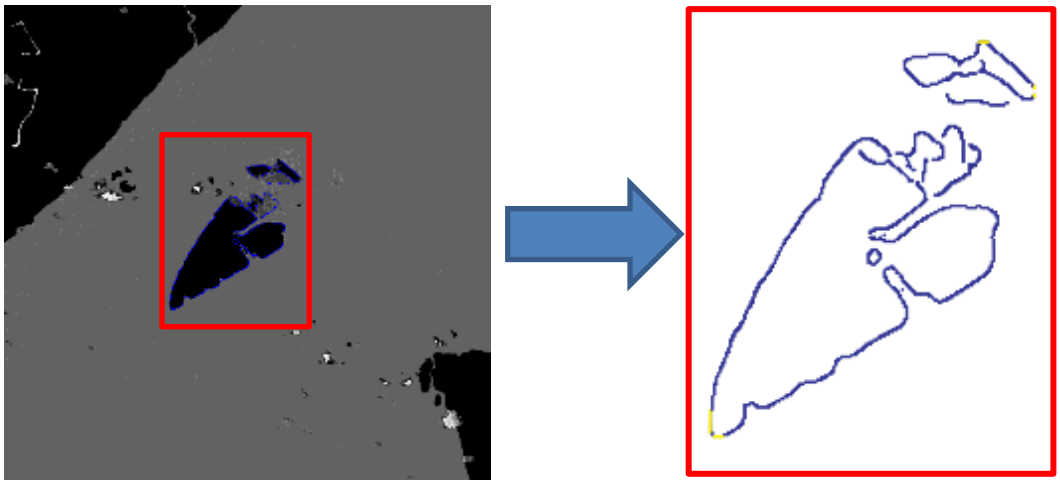

Figure 4.1. (Left image): Canny edge detection results based on log ratio of imagery bands. The edges are used to identify "extreme points" (shown in yellow).

4.3 Change detection process for shallow-area features using time series and prediction

This section uses the mathematical simplification of complex features into ellipses (Appendix B). Knowing the parameters of such conics enables the establishment of a mathematic relationship among them along time. Based on this relationship model, predictions in how the features would behave in the near future can be estimated.

Since this process is based on generalizing a caution area into an ellipse with known geometric parameters, it is possible to map feature transformations over time (Figure 4.2). As such, this process can be performed using all the imagery datasets that are available for a specific area over different time periods. This can provide a means of historical change detection analysis over time.

To predict a probable caution area ellipse for the near future, the general ellipse equation is modified by adding a time variable:

$$E(x, y, t) = x^2 + c1_t \cdot x \cdot y + c2_t \cdot x^2 + c3_t \cdot x + c4_t \cdot y + c5_t = 0 \qquad 4.16$$

Solving such system of equations can be performed more efficiently when parametric equation variables are used. The process involves working with each of the variables separately, (e.g., *a(t)*, *b(t)*, *θ(t)*, *x0(t)* and *y0(t))* one at a time. A linear regression model was developed for each *x0(t)* and *y0(t)*. The prediction variables *a(t)* and *b(t)* were constrained by upper CL95 value or using a maximum observed value for each semi-axis, whichever was smaller. Finally, both lower and upper CL95 values for *θ(t)* were calculated, and provided a two-ellipse result for each prediction. However, if CL95 was beyond max/min observed range for *θ(t)*, only the last two parameters were used.

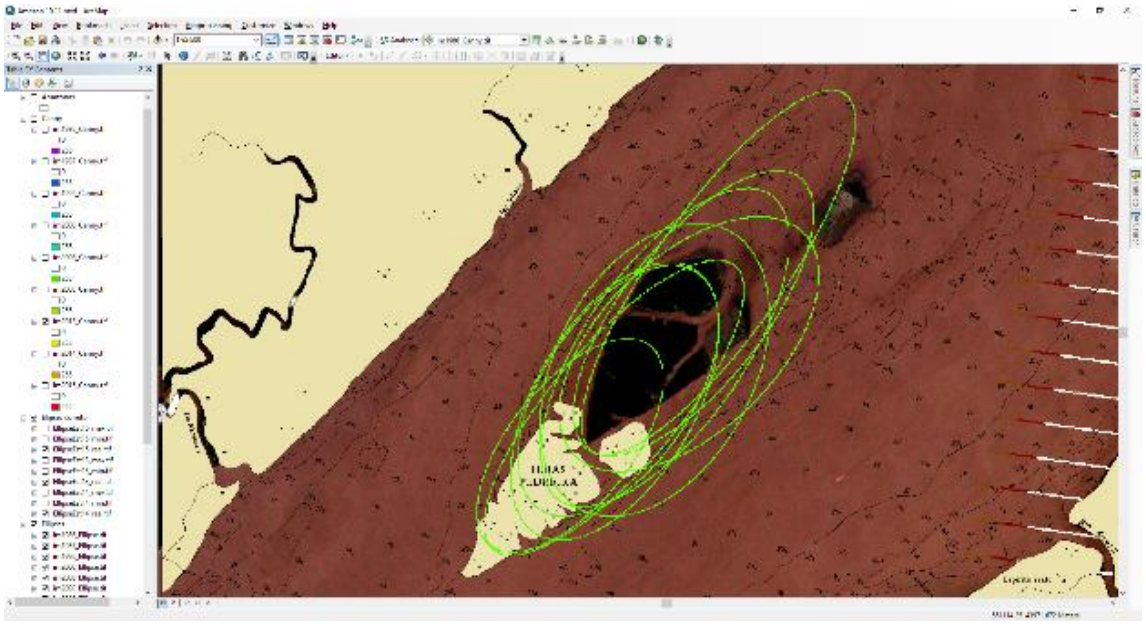

Figure 4.2. Ellipse transformations along time (1986-2015).

4.4 Study Sites

The first study site investigated by the change detection process developed in this study was the Yukon River, Alaska, USA, which is 3,185 km long and discharges an average of 5.7 x 10^3 m^3 s^{-1} (Brabets et al., 2000). The Yukon River serves several communities in the area that require their essential commodities to be transported by barges, including: fuel, fishery, construction equipment and material (Lower Yukon River Regional Port Project, 2014). There have been efforts to create a hub at Emmonak to optimize river usage to distribute goods for other local communities. However, no hydrographic surveys were conducted in the region since the 1898-1899 field seasons that were used to create the two first edition charts covering Apoon (Chart 9372) and Kwikluak (Chart 9373) Passes in the Yukon River Delta at a scale of 1:80,000. The original sounding data are still found on the current largest scale NOAA Raster Navigational Chart (RNC) Chart 16240 at a scale of 1:300,000 (Figure 4.3).

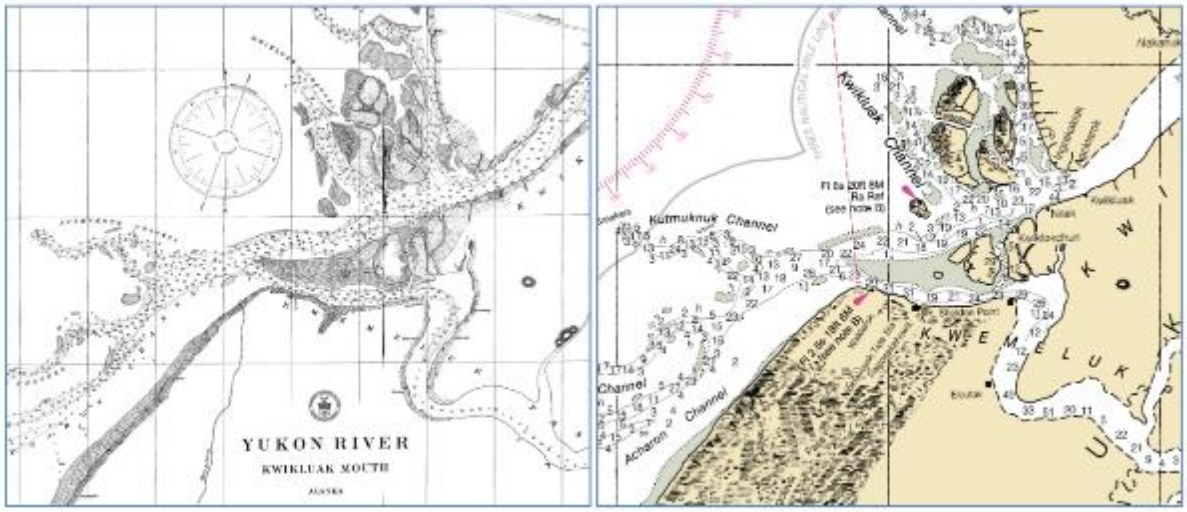

Figure 4.3. Comparison of Chart 9373 in 1907 in feet (left) and Chart 16240 in 2016 in fathoms (right).

The second study site investigated by the change detection process developed in this study was the Amazon River that is 6,992 km long. The delta region is ~150 km wide and contributes with almost 20% of Earth's freshwater discharge into the ocean. The Amazon River contains more than 1,000 tributaries, three of them > 3,000 km in length (UNEP, 2009). It experiences an average of 1.3 x 10^6 km^2 of sediment plume seasonally with discharges that vary from 0.8 x 10^5 m^3 s^{-1} to 2.4 x 10^5 m^3 s^{-1} (Grodsky et al., 2013, Cunha et al., 2012 and Moura et al., 2016). The Amazon River basin and its tributaries are responsible for half of Brazil's commercial maritime riverine network (Wiegmans and Konings, 2017). Due to logistical constraints of operating in a large river with strong currents and in a jungle surrounding, survey operations near the entrance have not been conducted since the late 1970's. However, shoal and exposed features within the river have been observed shifting over time using satellite imagery (Figure 4.4).

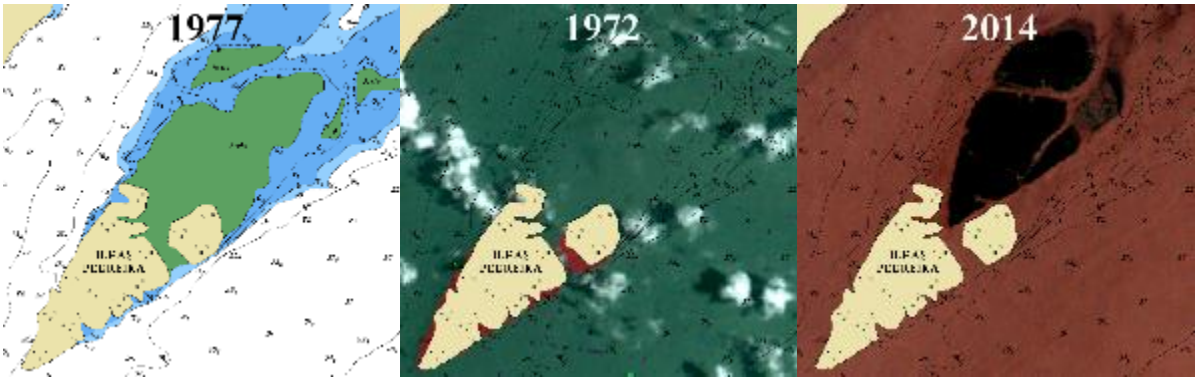

Figure 4.4. Amazon River Study site: (left) DHN chart 203 (1:80,000), (center) Landsat 1 imagery acquired in 1972, and (right) Landsat 8 imagery acquired in 2014.

4.5 Results

4.5.1 Yukon River

NOAA has recently updated the river banks of the Yukon River and shoal-feature locations within it as newly released Electronic Navigational Charts (ENC) using on SDB data (Kampia et al., 2016). However, no depth values are present since no hydrographic surveys have been conducted over the past 117 years. As such, the SDB results cannot be vertically referenced to chart datum without reliable control points available, and are subject to water level variations. To minimize the water-level impact on the SDB results, five satellite imagery datasets over a 13-year period were used for analysis of the shoal-feature location (Table 4.1). In is important to note that although the satellite repetition rate over a given site is 16 days, cloud coverage and ice limited the ability to use many images in the datasets at the latitude of the study site.

Satellite	Date	Cloud coverage (%)	Dynamic range
Landsat 7	2002-08-21	0.00	8-bits
Landsat 5	2006-10-26	2.00	8-bits
Landsat 5	2008-05-24	18.00	8-bits
Landsat 8	2014-09-06	0.00	12-bits
Landsat 8	2015-06-21	0.16	12-bits

Table 4.1. List of *Landsat* imagery used at Yukon River.

Two shallow-water areas at in the entrance of Yukon River were selected for this study (Figure 4.5). A topological linear regression for Site 1 located on the southwestern part of the entrance was created using the 2006, 2008 and 2014 imagery. The early three images (i.e., 2006, 2008 and 2014) were also analyzed to generate two predictions (i.e., lower and upper CL95 ellipses) for the shoal location in June 21, 2015. A time-series for Site 2, located on the northeastern part of the entrance, was created using satellite imagery acquired in 2002, 2006, 2008 and 2014. Similar to Site 1, the early four images (i.e., 2002, 2006, 2008 and 2014) were also analyzed to generate two predictions for the shoal location in June 21, 2015. Feature extraction and analysis from a 2015 satellite imagery was used as a reference and compared to the prediction results generated for both areas.

Figure 4.5. Two shallow-water sites in the Yukon River in which features were extracted using Canny edge detection.

The calculated time-series over Site 1 (2006-2014) show that the shoal-area was advancing toward the Bering Sea at a rate of -0.103 km/yr easting and 0.043 km/yr northing. It is also noticeable that the fitted ellipses' size and orientation changed as sediment eroded from eastern side and accreted on the western side. These changes were also dependent on the river's water level. Based on the translation parameters of the fitted ellipses, a linear regression was calculated for each of the areas (Figure 4.6). At Site 2 (2002-2014) was observed a rate of 0.016 km/yr easting and 0.011 km/yr northing. This shoal showed the lowest determination coefficients.

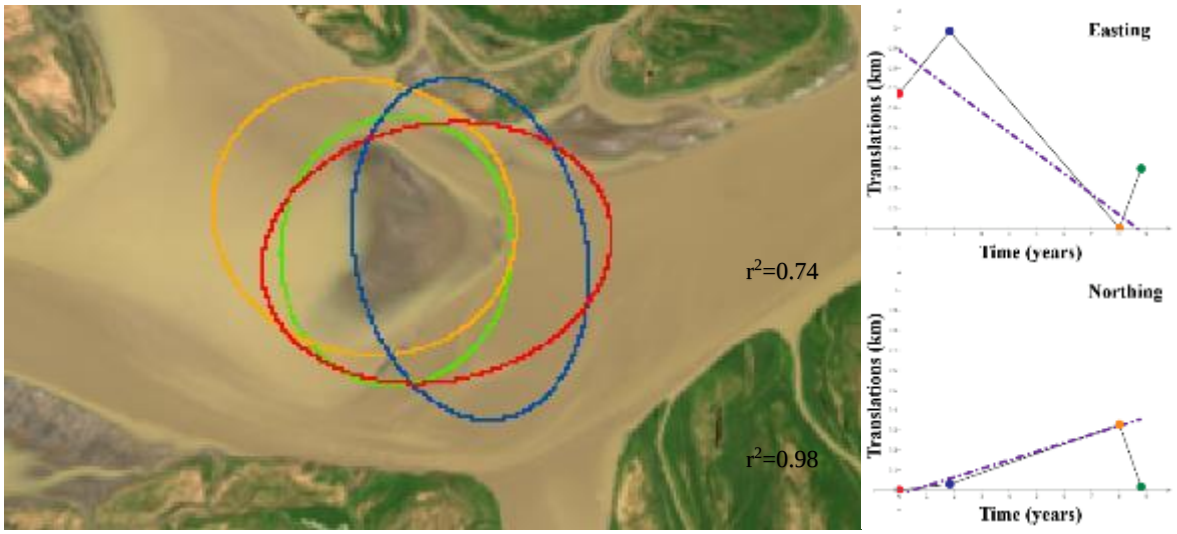

Figure 4.6. Time series of Shoal area 1 calculated using the topological fitting over an 8-year period starting from Sep-01, 2006. The ellipses red (2006), blue (2008), orange (2014) and green (2015) are represent the best fitting for features extracted using Canny edge detection.

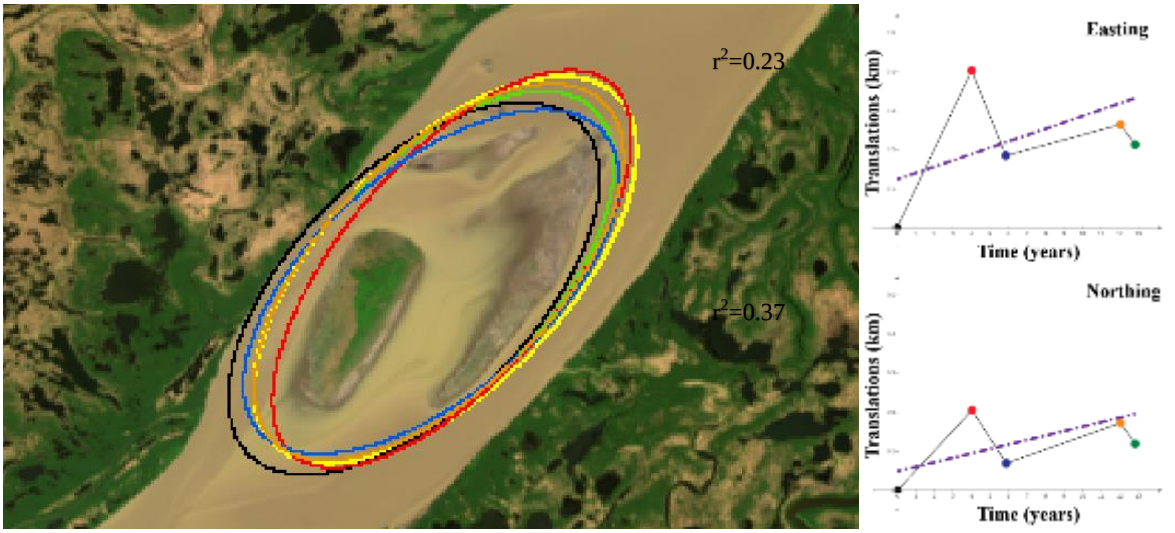

Figure 4.7. Time series of Shoal area 2 calculated using the topological fitting over a 12-year period starting from Aug-21, 2002. The ellipses black (2002), red (2006), blue (2008), orange (2014) and green (2015) are represent the best fitting for features extracted using Canny edge detection.

The predicted ellipses (yellow), for each site, were compared against the fitted ellipses (green) extracted from the 2015 satellite imagery (Figure 4.8). Results indicate that it is possible to relate the dynamic motion of the feature to the performance of prediction tool. In Site 1, the extracted feature is contained by the predicted ellipses and only a small portion of fitted ellipse (about 3.5% of its total area) is outside the predicted ellipses. Although the geometric union of predicted ellipses (shown in yellow) does not contain the entire area of the fitted ellipse (show in green), the feature edges were all correctly bounded. The distance between the center of predicted ellipses and the extracted ellipse is 463 m. The orientation of the predicted ellipses was 16º and 111º with respect to the extracted ellipse. The prediction results for Site 2 are better than Site 1. Both predicted ellipses are close to each other and to the extracted ellipse. The distance between the center of predicted ellipses and the extracted ellipse is 141 m. The orientation of the predicted ellipses was -1º and 2º with respect to the extracted ellipse.

Figure 4.8. Yellow ellipses represent predicted geometries for 2015, while green one are based on actual observed data for this year.

4.5.2 Amazon River

The shallow-water area selected at the entrance of the Amazon River Entrance is Pedreira Islands, near Macapá city, Amapá, Brazil (Figure 4.9). These islands, located on the northern branch of the river entrance, were analyzed using satellite imagery acquired over a 29-year period (1986 – 2015) to calculate and characterize the feature's dynamic trend (Figure 4.10). Cloud cover and high-water levels (up to 6 m in range) restricted the dataset to ten usable images (Table 2). Features analyzed from satellite imagery acquired in 1986, 1987, 1996, 2000, 2006 and 2008 was used to calculate a trend. Satellite imagery acquired in 2013, 2014 and 2015 was used as a reference to predicted feature locations based on the calculated trend.

Image file	Date	Cloud coverage (%)	Dynamic range
Landsat 5	1986-07-15	0.00	8-bits
Landsat 5	1987-07-02	11.00	8-bits
Landsat 5	1996-08-27	15.00	8-bits
Landsat 5	2000-09-07	17.00	8-bits
Landsat 5	2006-10-26	2.00	8-bits
Landsat 5	2008-05-24	18.00	8-bits
Landsat 8	2013-09-27	9.23	12-bits
Landsat 8	2014-09-14	10.79	12-bits
Landsat 7	2015-08-24	6.00	8-bits

Table 4.2. List of *Landsat* imagery used at Amazon River.

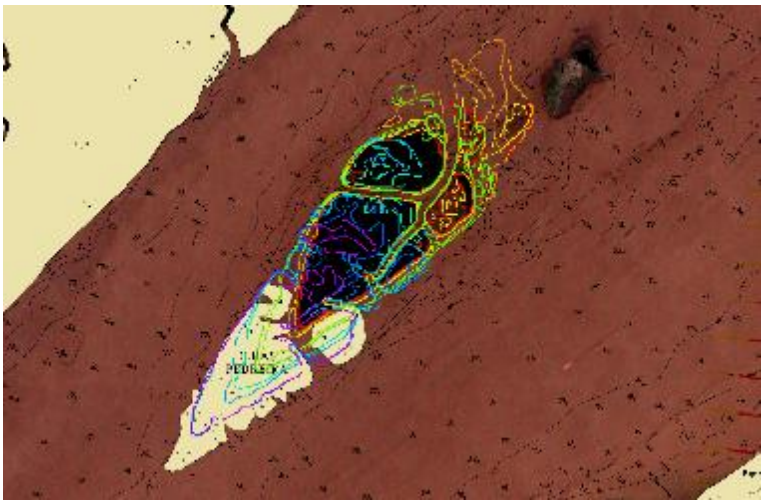

Figure 4.9. Edge detection at Amazon River. Image based on 2015 data.

It is noticeable that a process of erosion and accretion affected Ilhas Pedreiras site over time. To map the dynamic changes that occurred during this process, the same assumptions used for the Yukon River ellipse parameters were applied to the Amazon study site. In particular, the translation variables were modeled using a linear regression while the other components were statistically constrained.

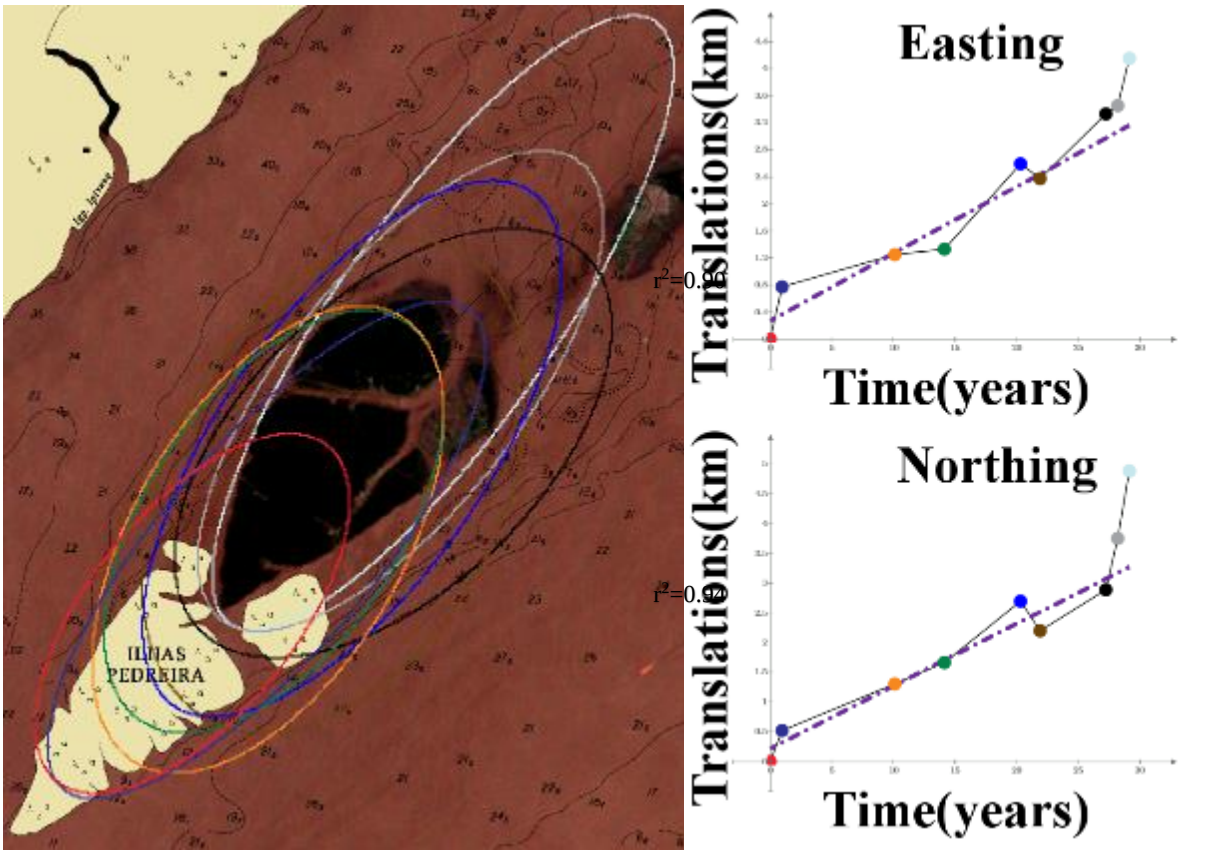

Figure 4.10. Time series of Shoal area calculated using the topological fitting over a 22-year period starting from Jul-15, 1986. The ellipses red (1986), dark blue (1987), orange (1996), green (2000), blue (2006), brown (2008), black (2013), grey (2014) and light blue (2015) represent the best fitting for features extracted using Canny edge detection.

The prediction for the shoal feature location in the Amazon study site was conducted for 5, 6 and 7 years into the future of the last satellite image (2008). These results allow to identify the differences between the predicted geometrics and the extracted (i.e., actual) location of a shoal feature over time. The results for a 5-year (i.e., 2013) and a 6-year prediction into the future show that the predicted ellipses are close in distance and in orientation to the extracted ellipses. For a 5-year prediction (2013), the distance between the center of predicted ellipses and the extracted ellipse is 402 m. The orientation of the predicted ellipses was 4º and 8º with respect to the extracted ellipse. For the 2014 prediction, the distance between the center of predicted ellipses and the

extracted ellipse is 694 m. The orientation of the predicted ellipses was -3º and 10º with respect to the extracted ellipse. Finally, for 2015, the distance between the center of predicted ellipses and the extracted ellipse is 1890 m. The orientation of the predicted ellipses was -6º and 7º with respect to the extracted ellipse.

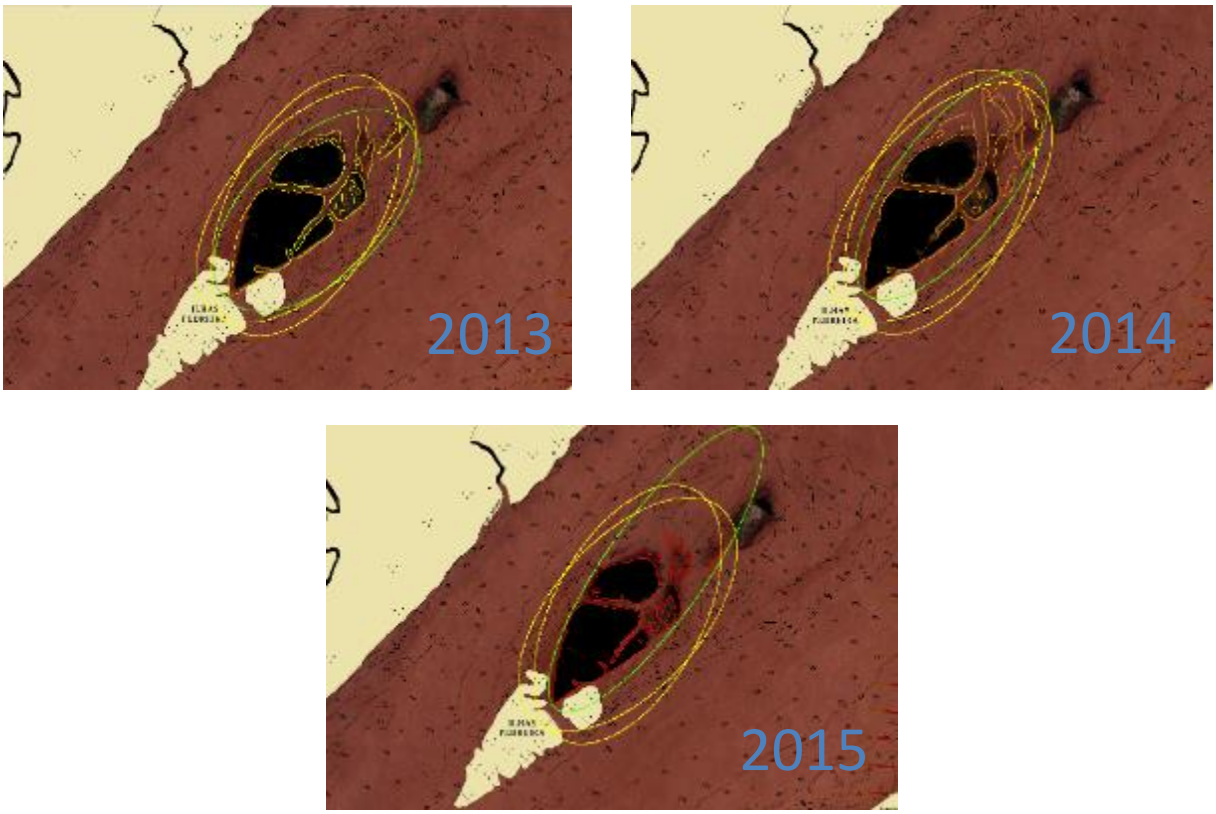

Figure 4.11. Yellow ellipses represent predicted geometries while green ones are based on actual observed data for 2013 (a), 2014 (b) and 2015 (c).

4.6 Discussion

The results of the study demonstrated the ability to update the suitability and extend the use of an existing nauticalchart using remote sensing techniques. By using an SDB ratio model

with image processing techniques that include feature extraction and a well-defined topological feature to describe the shoal feature, it is possible to create a time series of the shoal's motion, and predict its location in the near-future (e.g., up to 7 years). The benefit of this approach is that there is no need for vertically referencing of the SDB ratio model to chart datum.

The results of study also identify dependence of the change detection process on the image quality and the environmental factors, especially the two selected study sites located in Arctic and Amazon regions. Key steps in the change detection process are feature extraction and topological fitting steps. An area of interest is extracted and then generalized using a Canny edge detection. Then, the area is fitted into a well-defined topological feature. The use of multiple satellite platforms with different dynamic ranges (i.e., 8-bit and 12-bit) reduces the performance of the feature extraction step, especially with *Landsat 5* and *7* imagery. Even after low-pass filtering per channel, the log ratio of *Landsat 5* and *7* was noisier and affected the detection capability of the algorithms. It would be useful to investigate other adjustment techniques to enhance ellipses fitting around the edges. The elongated ellipse calculated for 2015 data in Amazon River could be readjusted by adding a geometrical constraint, such as applying a Lagrange multiplier that would also search for a minimum area or eccentricity.

The environmental factors affecting the change detection process included persistent cloud coverage and freezing of the water surface (in the case of the Yukon River). These environmental factors limited the number of usable images to less than one image per year. The river's water level also affected edge detection algorithms. Since the water levels in riverine environments vary according to meteorological conditions, it is hard to vertical reference a given feature from all the available satellite images and select the same elevations for boundaries. Instead, a selection of the last three or four images over a 5-year period or longer will cover most scenarios. It is expected

that areas with higher availability of satellite imagery would perform better since time interval between detected features would be minimized, and the influence of water level on the detected shallow structures would be more evident.

Both the Amazon River and Yukon River (site 1) presented relevant coefficient of determination values for Easting and Northing. For the Amazon area, it is noticeable that Year 2015 presented a greater difference between predicted and observed ellipse centers (1890 m). Although there is expected decrease in the ability to predict further changes over time, this difference is caused by the elongated geometry of the fitting ellipse. As such, imposing conditions to geometric adjustment may provide better predictions. The northing and easting rates shows a very dynamic environment (Figure 4.10). When associated to high coefficient of determination values, this becomes an interesting site to develop meaningful prediction models. The same consideration applies to Yukon River study site 1. Those two sites should be monitored continuously (e.g., annually), although it may be difficult to obtain usable images due to constant cloud coverage and persistent ice coverage (in Alaska case).

When analyzing easting and northing of shallow features at Site 2, there are low coefficients of determination values. However, these almost stationary shoals (rates of 0.016 km/yr easting and 0.011 km/yr northing) exhibited the highest agreement between predicted and observed ellipses in the study. Although study site 2 poses a risk to navigation, its stability along time lessens its importance in terms of continuous monitoring. Perhaps checking it every 5-10 years would be sufficient.

Figure 4.12. Translation of shoals at Pedreira Islands, Amazon River, Brazil between nautical chart 203 (1977) and satellite image (2014).

Re-positioning shoal areas on charts using the SDB approach has been applied to several NOAA charts, including the Yukon River (Kampia et al., 2016). As mentioned previously, trend calculations of dynamic features using SDB can be used to extend the adequacy of the charted features for river navigation up to five years beyond the dates of the satellite imagery. This recommendation is illustrated in the Yukon River (Figure 4.13). Extracted ellipses from 8-year and 12-year datasets are stacked together with predicted ellipses one year beyond the last image in the dataset (shoreline and shallow water areas). As a result, the hydrographic office can predict the routes of the marine vessels along the river, and plan surveys accordingly. In Figure 4.13, the predicted traffic was marked (pink) and compared to Automatic Identification System (AIS) data (red circles).

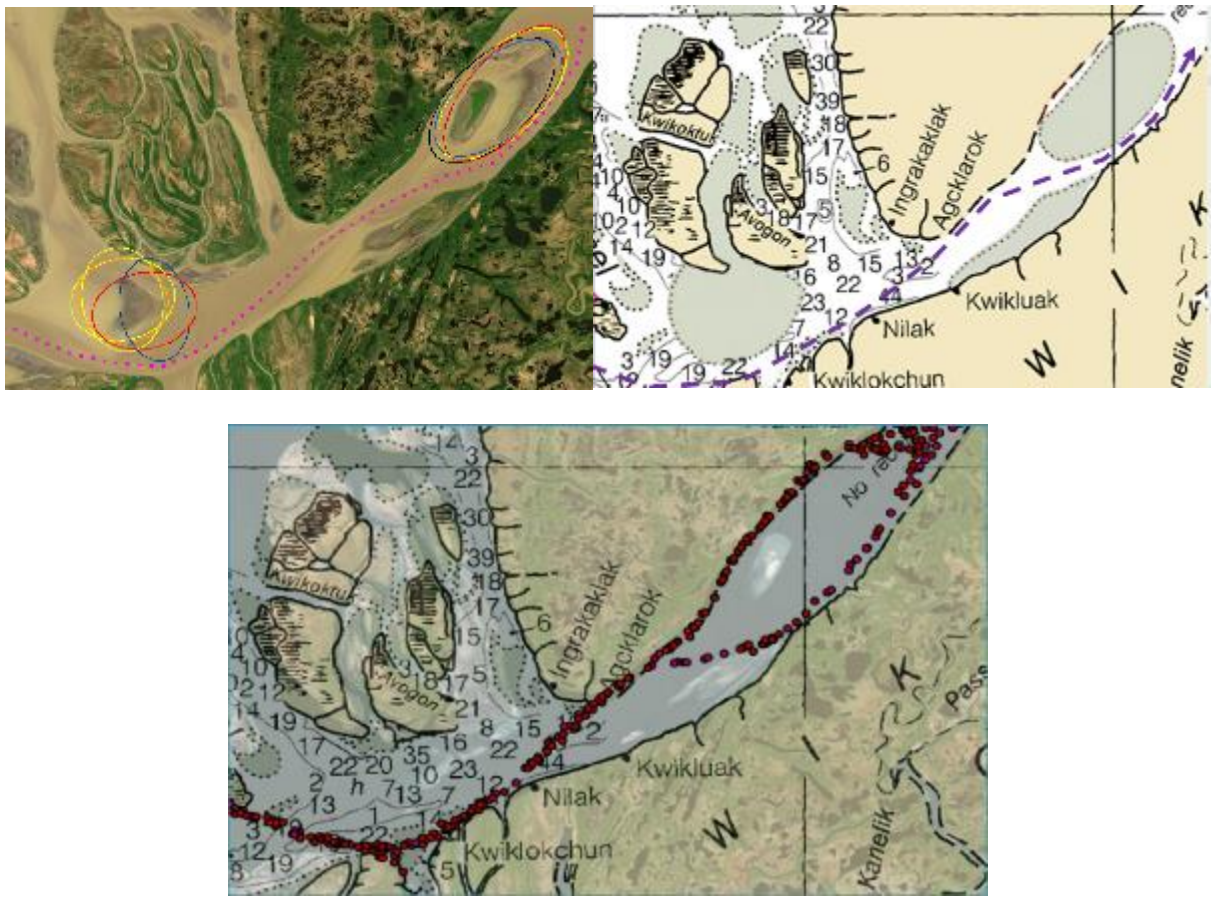

Figure 4.13. Predicted route (pink) compared to Satellite AIS points (in red) overlaid on Chart 16240, with ESRI Imagery Basemap service in the background (Courtesy of Lt. Anthony Klemm).

CHAPTER 5

DERIVING OPTICAL CHARACTERISTICS USING A NON-LINEAR SDB APPROACH

5.1 Introduction

Optical remote sensing technologies have been used to acquire shallow-water bathymetry up to the shoreline since the 1990's. The two main technologies include airborne lidar bathymetry (ALB) and Satellite-derived bathymetry (SDB). ALB is an active remote sensing technology that uses a pulsed laser beam to measure water depths by calculating the two-way travel time of the laser pulses through water column. SDB is a passive remote sensing technology that utilizes different multispectral bands to infer water depth based on changes in observed radiance measurements.

Over the past two decades, ALB has been used extensively to map nearshore areas for chart updates (e.g., Pe'eri and Long, 2011; White et al. 2011; Pastol, 2011). Since ALB is an optical system its performance is dependent on the optical characteristics of the water (Guenther, 1985). The main limiting factor affecting the performance of ALB is water clarity, namely the diffuse attenuation coefficient. As a result, the water depth of the seafloor can only be estimated to the extent of light penetration.

On the other hand, SDB provides a cost-effective reconnaissance tool for assessing bathymetry in remote locations, or prior to a hydrographic survey using traditional sensors, such as acoustic or ALB (Pe'eri et al., 2015). Although its accuracy is lower than ALB, there are publicly available multispectral imagery covering many parts of the world. Traditional SDB

optimization methods (Dierssen et al., 2003; Stumpf et al., 2003) assume a uniform bottom reflectance and water attenuation. This assumption implies that any changes in either of these environmental parameters are minor with respect to the depth calculation. Further, it is assumed that a linear relationship exists between calibrations points (i.e., soundings) and the SDB model (i.e., the log ratio values between two bands of the satellite imagery).

Similar to ALB, a single SDB result may detect a plume of suspended matter in the water and be misinterpreted it as a shoal. Previous work has shown that sediment plumes produce "false bathymetry" areas that are different in depth than the actual bottom bathymetry (Pe'eri et al., 2014; Philpot et al., 2004; Stumpf et al., 2003). SDB also assumes a uniform linear relationship exists between calibrations points and the SDB model in specific environmental conditions (i.e., null water column and constant bottom type returns). As such, non-uniform water column or bottom conditions will affect depth estimates using SDB.

In this study, the goal is to use the multispectral bands in satellite imagery and its repeatable spatial coverage over an area to estimate environmental conditions using an enhanced SDB approach. The enhanced approach uses a non-linear calculation to estimate depth in non-uniform conditions, and compare the depth to available control points. It is possible to estimate water column conditions over time, assuming bottom characteristics do not change during the observation period.

The study site that was selected presents a major challenge for a linear SDB model approach. As such, Dierssen's band ratio SDB algorithm was developed into a full non-linear SDB model. The new non-linear SDB model was evaluated in the Simeonof Island, AK area using *Landsat 8* imagery. The control points used in this project came from a NOAA ALB survey H12103, conducted between May and August of 2009. However, adverse sea-state conditions

during the time of the survey resulted in some ALB survey gaps. A linear and non-linear SDB model were generated using control points acquired by NOAA ALB survey. Both models were compared to each other using the ALB survey for performance evaluation.

5.2 Linear SDB model

5.2.1 SDB approach

The linear SDB model is an optimization approach that uses the ratio of the logarithms of the blue and green bands (Stumpf et al., 2003). Assuming that the turbidity in the water column is uniform, this ratio algorithm output is expected to vary linearly with depth (Lyzenga, 1978; Philpot et al., 2004; Lyzenga, et al., 2006). Tidally-referenced survey soundings can be used to linearly transform the log ratio into meaningful depths that are referenced to chart datum. There is no need to measure the tide height during the image acquisition since the determination of the transformation parameters from the tidally-referenced control points automatically accounts for the tide (Pe'eri et al. 2014). Differences in water levels are usually well approximated as a vertical offset, and do not impair the linear relationship between chart control points and ratio algorithm output. Therefore, the procedure eliminates the need for either tide-coordinated imagery or tide correctors.

The linear SDB model involves four (4) main steps: (1) radiometric enhancement, (2) dry-land removal, (3) calculation of the SDB ratio model, and 4) vertical referencing.

Radiometric enhancement **-** To remove radiometric noise (e.g., speckle noise, banding or striping) from the satellite imagery, a 3X3 Gaussian low-pass kernel was applied to the imagery dataset as a pre-processing step:

$$\frac{1}{16}\begin{pmatrix}1 & 2 & 1\\ 2 & 4 & 2\\ 1 & 2 & 1\end{pmatrix} \quad 5.1$$

Dry-land removal **-** Next, water body areas were separated from land areas using shortwave infrared (SWIR) band $L_{obs}\ (\lambda_{SWIR})$ and Red (R) band, $L_{obs}\ (\lambda_R)$, as a spatial condition to mask dry land areas from visible bands and extract the water bodies. This land/water separation was performed using a Normalized Difference Water Index (NDWI) based on McFeeters, (1996), Gao (1996), Ji et al.(2009), and McFeeters (2013):

$$NDWI = \frac{\mathrm{L_{obs}}\ (\lambda_R) - \mathrm{L_{obs}}\ (\lambda_{SWIR})}{\mathrm{L_{obs}}\ (\lambda_R) + \mathrm{L_{obs}}\ (\lambda_{SWIR})} \quad 5.2$$

Calculation of the SDB linear ratio model

A SDB ratio model was then calculated using a log ratio between two bands $L_{obs}\ (\lambda_1)$ and $L_{obs}\ (\lambda_2)$ (Dierssen et al., 2003):

$$z = m_0 \cdot ln\left(\frac{L_{obs}\ (\lambda_1)}{L_{obs}(\lambda_2)}\right) + m_1 \quad 5.3$$

Where, m_0 is the scaling coefficient (based on the diffuse attenuation coefficient) and m_1 is the translation coefficient (based on bottom return and diffuse attenuation coefficient).

5.2.2 SDB approach

It is useful to explain the development of the linear model to understand its limitations. Using a simplified radiative transfer equation (RTE) solution following Philpot (1989), it is possible to correlate observed radiance $L(\lambda)$, bottom radiance $L_b(\lambda)$, radiance scattered from the water column $L_w(\lambda)$, and diffuse attenuation coefficient, $k(\lambda)$, to water depth z.

$$L(\lambda) = [L_b(\lambda) - L_w(\lambda)]e^{-2k(\lambda)z} + L_w(\lambda) \quad (5.4)$$

Next, this relationship is rearranged to have all the radiance parameters on the same side.

$$\frac{L(\lambda_1) - L_w(\lambda_1)}{L_b(\lambda_1) - L_w(\lambda_1)} = e^{-2k(\lambda_1)z}$$

$$\frac{L(\lambda_2) - L_w(\lambda_2)}{L_b(\lambda_2) - L_w(\lambda_2)} = e^{-2k(\lambda_2)z} \quad (5.5)$$

This enables solving for depth, z, by dividing between the λ_1 and λ_2 relationships:

$$z = \frac{1}{-2\big(k(\lambda_1) - k(\lambda_2)\big)}\left[ln\left(\frac{L(\lambda_1) - L_w(\lambda_1)}{L(\lambda_2) - L_w(\lambda_2)}\right) + ln\left(\frac{L_b(\lambda_2) - L_w(\lambda_2)}{L_b(\lambda_1) - L_w(\lambda_1)}\right)\right] \quad (5.6)$$

In the case of a linear SDB model, it is assumed that the water contribution for the observed radiance is negligible with uniform bottom conditions (i.e., $\left(L_b(\lambda_2)\right)/\left(L_b(\lambda_1)\right) \approx Constant$).

5.3 Non-linear SDB model and optical properties estimation

5.3.1 Non-linear form

In the case of a non-linear form, Equation 5.6 is used instead of Dierssen's algorithm (Equation 5.3):

$$z = m_0 ln\left[\frac{L(\lambda_1) - L_w(\lambda_1)}{L(\lambda_2) - L_w(\lambda_2)}\right] + m_1 \qquad 5.7$$

Where $m_0 = \frac{1}{-2\left(k(\lambda_1) - k(\lambda_2)\right)}$ and $m_1 = m_0 ln\left[\frac{L_b(\lambda_2) - L_w(\lambda_2)}{L_b(\lambda_1) - L_w(\lambda_1)}\right]$. The solution vector for the non-linear system of equations defined from 5.7 is represented by $X^T = \left(\widehat{m_0}, \widehat{L_w(\lambda_1)}, \widehat{L_w(\lambda_2)}, \widehat{m_1}\right)$. Like SDB based on linear regression, z_n soundings are used as control points. However, in the case of a non-linear SDB, the solution vector X is an approximated solution to the system of equations. The residual vector, V, observation vector, L, and the non-linear model, $F(X)$, are related by:

$$\underbrace{\begin{pmatrix} z_1 \\ \vdots \\ z_N \end{pmatrix}}_{L} + \underbrace{\begin{pmatrix} v_1 \\ \vdots \\ v_N \end{pmatrix}}_{V} = \underbrace{\begin{pmatrix} m_0 ln\left[\dfrac{L(\lambda_1)_1 - L_w(\lambda_1)}{L(\lambda_2)_1 - L_w(\lambda_2)}\right] + m_1 \\ \vdots \\ m_0 ln\left[\dfrac{L(\lambda_1)_N - L_w(\lambda_1)}{L(\lambda_2)_N - L_w(\lambda_2)}\right] + m_1 \end{pmatrix}}_{F(X)} \quad 5.8$$

To calculate solution vector, X, it is necessary to first linearize $F(X)$. Based on Wells and Krakiwsky (1971) and Gemael et al. (2015), the linearization can be performed using Taylor's series linear approximation around an initial approximation vector, $X0$:

$$V = F(X) - L = \underbrace{F(X0) - L}_{-\Delta L} + \underbrace{\left.\frac{dF(X)}{dX}\right|_{X=X0}}_{A} \underbrace{(X - X0)}_{\Delta X} = A\Delta X - \Delta L \quad 5.9$$

The Jacobian matrix, A, of the partial derivatives of the non-linear equations at $X0$ is:

$$A = \begin{pmatrix} ln\left[\dfrac{L(\lambda_1)_1 - \widehat{L_w(\lambda_1)}}{L(\lambda_2)_1 - L_w(\lambda_2)}\right] & -\dfrac{\widehat{m_0}}{L(\lambda_1)_1 - \widehat{L_w(\lambda_1)}} & \dfrac{\widehat{m_0}}{L(\lambda_2)_1 - \widehat{L_w(\lambda_2)}} & 1 \\ \vdots & \vdots & \vdots & \vdots \\ ln\left[\dfrac{L(\lambda_1)_N - \widehat{L_w(\lambda_1)}}{L(\lambda_2)_N - \widehat{L_w(\lambda_2)}}\right] & -\dfrac{\widehat{m_0}}{L(\lambda_1)_N - \widehat{L_w(\lambda_1)}} & \dfrac{\widehat{m_0}}{L(\lambda_2)_N - \widehat{L_w(\lambda_2)}} & 1 \end{pmatrix} \quad 5.10$$

The increment ΔX is calculated by minimizing the quadratic sum of the residuals, $V^T V$:

$$\Delta X = (A^T A)^{-1}(A^T \Delta L) \quad 5.11$$

Then, increment ΔX corrects the initial approximation $X0$ and produces a tentative solution vector, X:

$$X = X0 + \Delta X \tag{5.12}$$

The solution vector will be determined after n-iterations, when RMSE between the observation vector, L, and the non-linear model, $F(X)$, converging, i.e., RMSE is not decreasing when compared to RMSE0, as follows:

$$RMSE0 = \sqrt{\frac{V0^T V0}{N-4}} \qquad RMSE = \sqrt{\frac{V^T V}{N-4}} \tag{5.13}$$

Where $V0 = F(X0) - L$ and $V = F(X) - L$.

To summarize, the overall process for the proposed non-linear approach is shown as a flow chart in Figure 5.1. The process begins with a 'educated guess' for initial approximation vector $X0$ (Appendix 6-A) and its corresponding $RMSE0$. The next step is to calculate the increment vector based on the incremental observations vector, ΔL, at $X0$, as well as the Jacobian matrix, *A*, that stands for the partial derivatives from Taylor expansion at $X0$. Using increment vector result, the incremental ΔX is calculated. Then, an iterative process compares the *RMSE* of the potential solution vector, *X*, and the initial approximation RMSE0. If *RMSE* is less than *RMSE0*, then a new *X0* becomes *X* and the process is repeated until the smallest *RMSE* is achieved that becomes the 'final solution' for vector *X*.

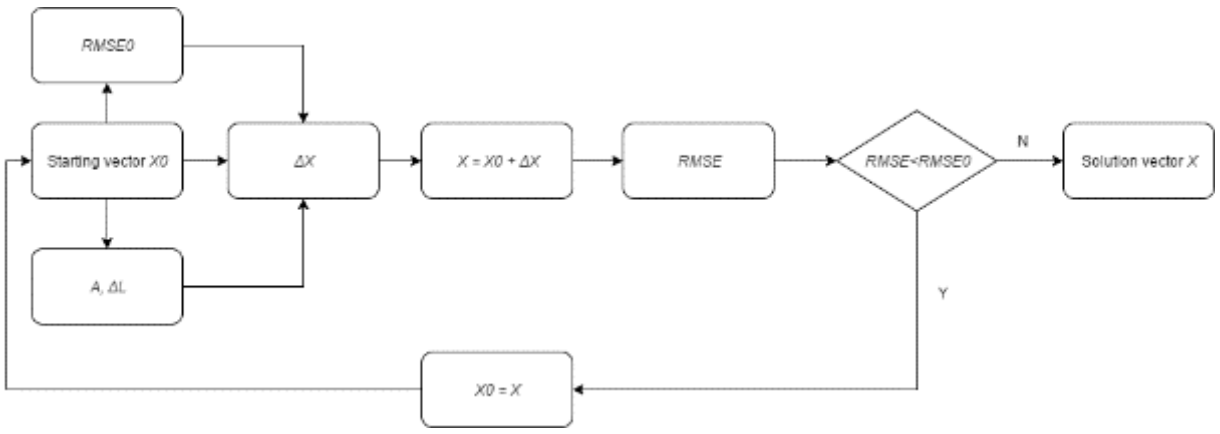

Figure 5.1. Non-linear adjustment flow chart, created using draw.io free online diagram software.

5.3.2 Diffuse attenuation estimation

The scaling coefficient, m_0, is based on the diffuse attenuation coefficients. It is possible to extract the diffuse attenuation coefficients using three band-pair combinations that include Blue-Green (BG), Blue-Red (BR), Green-Red (GR):

$$\begin{aligned} k(\lambda_B) - k(\lambda_G) &= \frac{1}{-2{m_0}^{BG}} \\ k(\lambda_G) - k(\lambda_R) &= \frac{1}{-2{m_0}^{GR}} \\ k(\lambda_B) - k(\lambda_R) &= \frac{1}{-2{m_0}^{BR}} \end{aligned} \qquad 5.14$$

This system of equations has an intrinsic singularity. Traditional LSM would fail since the product of Jacobian matrices is not invertible. To provide a solution, Moore-Penrose pseudoinverse was used.

5.3.3 Bottom estimation

As mentioned previously, the translation coefficient, m_1, in a SDB model is based on bottom return and a diffuse attenuation coefficient. Using the calculated solution vector, X, the translation coefficient can be defined as:

$$\widehat{m_1} = \widehat{m_0} ln \left[\frac{L_b(\lambda_2) - \widehat{L_w(\lambda_2)}}{L_b(\lambda_1) - \widehat{L_w(\lambda_1)}} \right] \quad 5.15$$

Equation 5.15 can be reorganized to show the dependence of $L_b(\lambda_1)$ on $L_b(\lambda_2)$ for Blue, Green and Red bands combinations:

$$L_b(\lambda_B) = \left(e^{-\widehat{m_1}/\widehat{m_0}} \right) L_b(\lambda_G) + \left[\widehat{L_w(\lambda_B)} - \left(e^{-\widehat{m_1}/\widehat{m_0}} \right) \widehat{L_w(\lambda_G)} \right]$$
$$L_b(\lambda_G) = \left(e^{-\widehat{m_1}/\widehat{m_0}} \right) L_b(\lambda_R) + \left[\widehat{L_w(\lambda_G)} - \left(e^{-\widehat{m_1}/\widehat{m_0}} \right) \widehat{L_w(\lambda_R)} \right] \quad 5.16$$

$$L_b(\lambda_B) = \left(e^{-\widehat{m_1}/\widehat{m_0}}\right) L_b(\lambda_R) + \left[\widehat{L_w(\lambda_B)} - \left(e^{-\widehat{m_1}/\widehat{m_0}}\right) \widehat{L_w(\lambda_R)}\right]$$

Assuming that each of the solution vectors are constants, then the dependence of $L_b(\lambda_1)$ on $L_b(\lambda_2)$ is linear:

$$L_b(\lambda_1) - \alpha_{12} L_b(\lambda_2) = \beta_{12} \qquad 5.17$$

As such, it is possible to extract the bottom radiance using three band-pair combinations that include Blue-Green (BG), Blue-Red (BR), Green-Red (GR):

$$\begin{aligned} L_b(\lambda_B) - \alpha_{BG} L_b(\lambda_G) &= \beta_{BG} \\ L_b(\lambda_B) - \alpha_{BR} L_b(\lambda_R) &= \beta_{BR} \\ L_b(\lambda_G) - \alpha_{GR} L_b(\lambda_R) &= \beta_{GR} \end{aligned} \qquad 5.18$$

It was also observed that land areas (removed using NDWI) present a strong correlation between the channels based on its determination coefficient (0.98). The result is consistent between the pairs of channels Blue, Green and Red (Figure 5.2). Unlike the local coefficients $(\alpha_{ij}, \beta_{ij})$ at 5.18 (i.e., are based on water column and diffuse attenuation coefficients), the coefficients that map land areas between channels are valid for the entire study area:

$$\gamma_{BG} L_b(\lambda_G) - L_b(\lambda_B) = -\xi_{BG}$$

$$\gamma_{BR} L_b(\lambda_R) - L_b(\lambda_B) = -\xi_{BR} \qquad 5.19$$

$$\gamma_{34} L_b(\lambda_R) - L_b(\lambda_G) = -\xi_{GR}$$

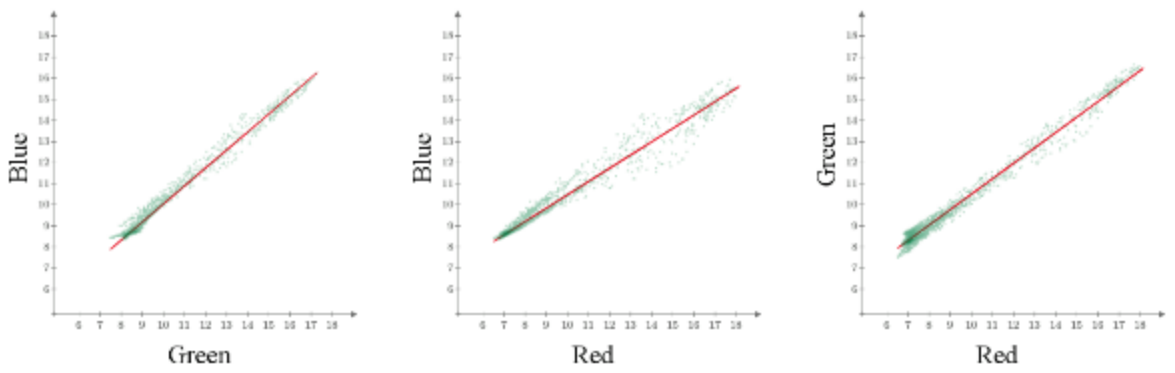

Figure 5.2. Determination coefficient on land areas between Blue, Green and Red channels. Digital numbers values, in the axis, were divided by 1000.

By reassigning 5.18 and 5.19 equations to a matrix format, it is possible to incorporate the bottom return radiance relationships into the solution vector, X_b:

$$X_b = \begin{pmatrix} L_b(\lambda_B) \\ L_b(\lambda_G) \\ L_b(\lambda_R) \end{pmatrix} = \left({A_b}^T A_b\right)^{-1} \left({A_b}^T P_b\right) \qquad 5.25$$

Where $A_b = \begin{pmatrix} 1 & -\alpha_{BG} & 0 \\ 0 & 1 & -\alpha_{GR} \\ 1 & 0 & -\alpha_{BR} \\ -1 & \gamma_{BG} & 0 \\ 0 & -1 & \gamma_{GR} \\ -1 & 0 & \gamma_{BR} \end{pmatrix}$ and $P_b = \begin{pmatrix} \beta_{BG} \\ \beta_{GR} \\ \beta_{BR} \\ -\xi_{BG} \\ -\xi_{GR} \\ -\xi_{BR} \end{pmatrix}$.

Finally, the solution vector values were constrained to the range of [5,000, 20,000]. If the result was not compliant, no bottom return was possible to detect for the analyzed cell. All three visible bottom band returns (i.e., blue, green, and red) are merged to a RGB raster using *ArcGIS* 10.4.1. Potentially, this enables the identification of different types of bottom conditions. Since there is no *a*-priori knowledge on the environmental factors or their spectral characteristics, an Iterative Self-Organizing Data Analysis Technique (ISODATA) is applied to the RGB raster image (Ball and Hall, 1965). This was achieved using *ArcMap Spatial Analyst* toolbox and selecting Iso Cluster Unsupervised Classification. Using the spectral information Red, Green and Blue bands, bottom responses were defined. The number of classes ranged from 5-10, a minimum class size was 20 and sampling interval was 10. This method of unsupervised classification provides the ability to estimate an initial number of classes that represent bottom conditions with similar spectral characteristics.

5.3.4 Sub-dividing study area

Traditional optimization SISDB methods (Stumpf et al., 2003, Dierssen et al., 2003, Pe'eri et al., 2015) are normally used to calculate linear parameters within a study area. In doing so, two assumptions are made: 1) the water column contributions are null, and 2) the bottom returns per

band are assumed to be constant throughout the study area. The results of this research study are different in that the diversity of physical conditions that normally exist within any study area are more fully considered.

A key assumption in this study is that the water column contributions and the bottom returns can be approximated as constant for each wavelength, but only within a small area. In this study, an ideal area for deriving a solution using the non-linear SDB processing was evaluated, where the area range is between 3x3 to 7x7 pixels. According to the maximum-area criteria, the study area was divided into a grid containing multiple, small cell areas (Figure 5.3). Using this approach, it is possible to develop more meaningful depth estimates for deeper areas than was previously possible using more traditional methods. Also, the use of a fixed value area, such as a grid, increases the computational performance when calculating the SDB model.

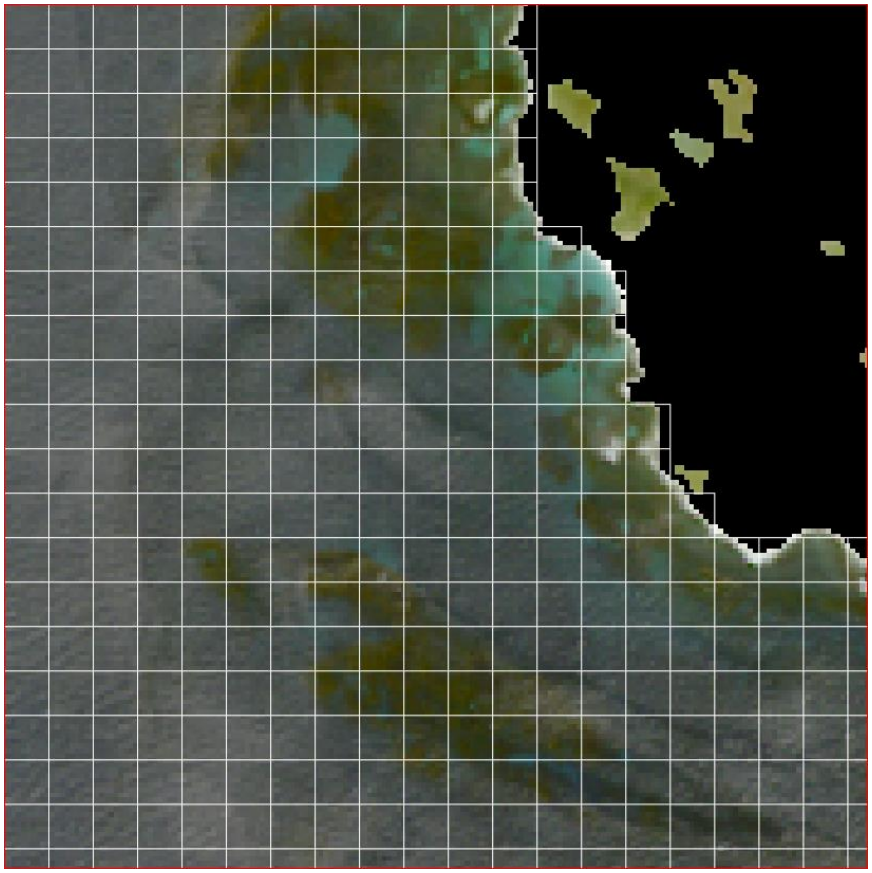

Figure 5.3. Southeast of Simeon of Island, AK study site divided into multiple small cells.

5.4 Results

The study site selected to test the non-linear SDB model is a shallow-water area (up to 30 m deep) southeast of Simeon Island, AK (Figure 5.4). In addition to constant cloud cover that limited the number of usable *Landsat 8* imagery, the study site is also characterized with dynamic non-uniform water column conditions and patches of vegetation (i.e., kelp). These environmental conditions pose a challenge for traditional SISDB processing. *Landsat 8* imagery was used to evaluate the non-linear SISDB algorithms. The satellite imagery was acquired in July 2016 with

low cloud coverage condition (1.14%). ALB survey data (NOAA survey H12103) that was performed during May - August 2009 was used as control points to vertically reference the SDB model. It is important to point out that the 2009 ALB survey did not achieve full bottom coverage and contained gaps (Figure 5.4). A possible explanation to the limited distribution of the control points were the high sea-state conditions during the ALB survey (NOAA/NOS H12103 Descriptive Report). The amount of ALB measurements was statistically down-sampled from 3-m spot spacing to 30-m spot spacing, i.e. the *Landsat 8* spatial resolution using common sampling techniques (Figure 5.4).

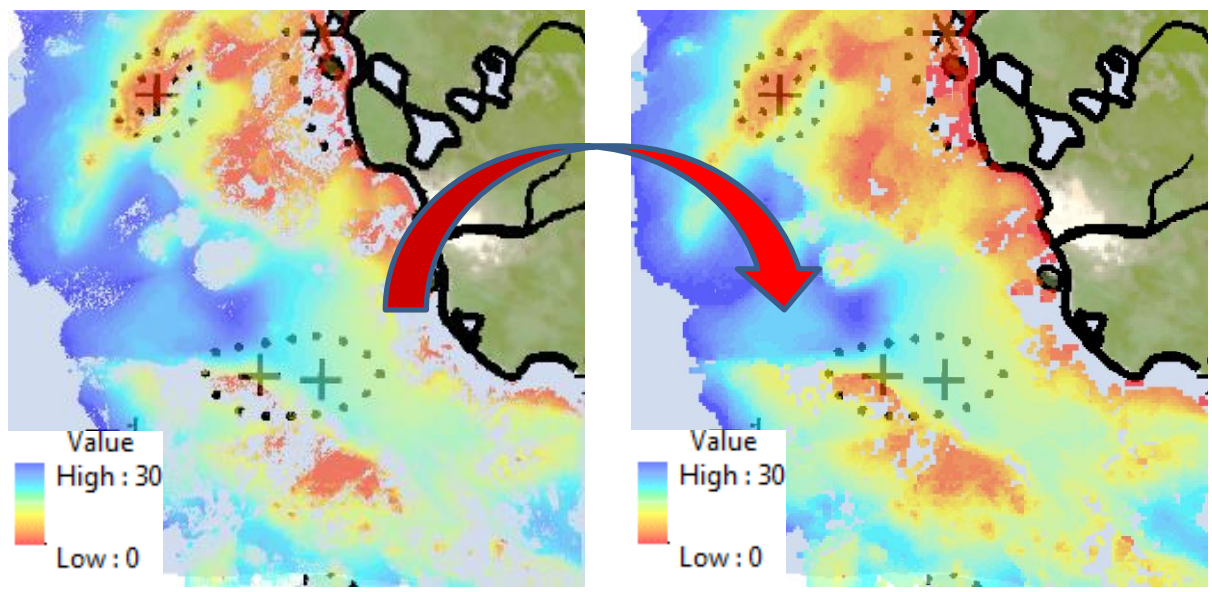

Figure 5.4. Control points from a 2009 ALB survey: (left) all available ALB measurements at an average 3-m spot spacing; (right) statistically down-sampled ALB measurements at 30-m spot spacing.

Bathymetry from the proposed non-linear SISDB model was compared to bathymetry derived using a traditional linear regression approach as described by Dierssen et al. (2003). The

effective optical depth (i.e., the extinction depth that the SDB model can detect the bottom) was also calculated using the control points in depths up to 30 m. Estimated extinction depths are 18 m, 6 m, and 6 m for the traditional linear SDB approach using the blue-green, green-red and blue-red bands, respectively (Figure 5.5). Linear model depths were estimated using control points until 30 m to match non-linear depth range. When comparing the bathymetry results from both SDB models to the control point values, the traditional SDB algorithm provides a rather poor result: RMSE of 6.07 m for the blue-green 7.15 m for green-red, and 7.28 m using, for the blue-red bands(Figure 5.5). It is important to note that all negative depth estimations (e.g., values that are above zero depth curve at chart datum) were converted to zero. Otherwise, the RMSE value could have be even higher. As shown in Figure 5.5, the scatter plot comparing depth estimations from the linear SDB model to its correlating control points is not tight around the control point trend line. In addition, the slope from the linear SDB models do not seem to overlap the control point trend line. This may be explained due to the water column geographic variability during the acquisition time of the satellite imagery.

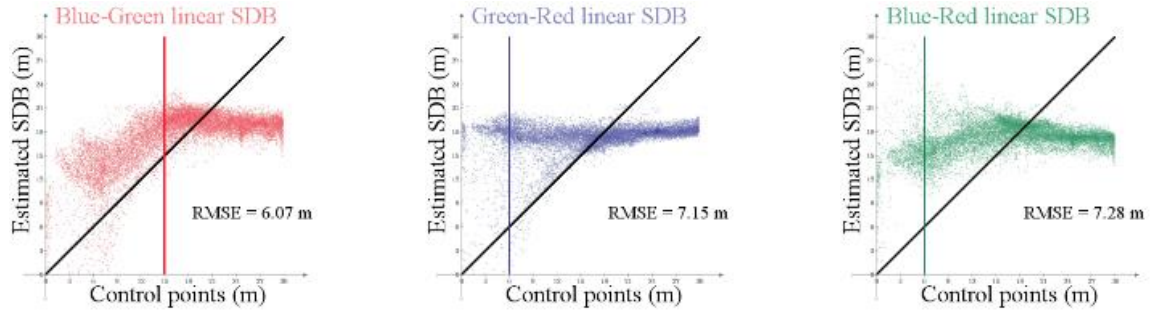

Figure 5.5. Scatter plots of the estimated linear SDB depths using blue-green, blue-red, and green-red band ratios against corresponding ALB measurements. The vertical colored lines stands for approximated extinction depth.

By subdividing the area into multiple cells and estimating the non-linear parameters for each cell, new depth estimations were calculated using a non-linear regressions and the selected ALB measurements in each given cell as control points. This non-linear method is dependent on the cell size, and a water column simulation process. Correlations between the nonlinear SDB model results and the control points were evaluated (Table 5.1, Figure 5.6). It is also important to note that the imagery was not converted to radiometric units (i.e., $W/m^2/sr$). Instead, imagery digital number values were used, assuming a 5% radiometric uncertainty (Mishra et al. 2014 and Czapla-Myers et al. 2015). The uncertainty was important to define the step used on the search algorithm that defined initial vector $X0$ (Appendix B). The SDB model results indicated that a smaller cell will provide a better RMSE result. These results are expected as it is easier to fit smaller area to a given surface. However, having less than three control points within a cell would prevent to estimate depths, even when using a linear SDB model (minimum degree of freedom of one). For the non-linear SISDB model, there is no indication of the extinction depth for the blue-green, green-red and blue-red ratios (Figure 5.6). This issue is an artifact is caused by the image-processing algorithm that do not use a threshold. Since each spatial section of image is fitted to the control dataset, a transformation will "force" the water column radiance with no bottom detection to match the control point's surface solution.

Squared Window Side (cells)	RMSE (m)		
	Blue-Green	Green-Red	Blue-Red
3	0.67	0.69	0.66

Table 5.1. RMSE values of multiple non-linear regressions when modifying band pairs.

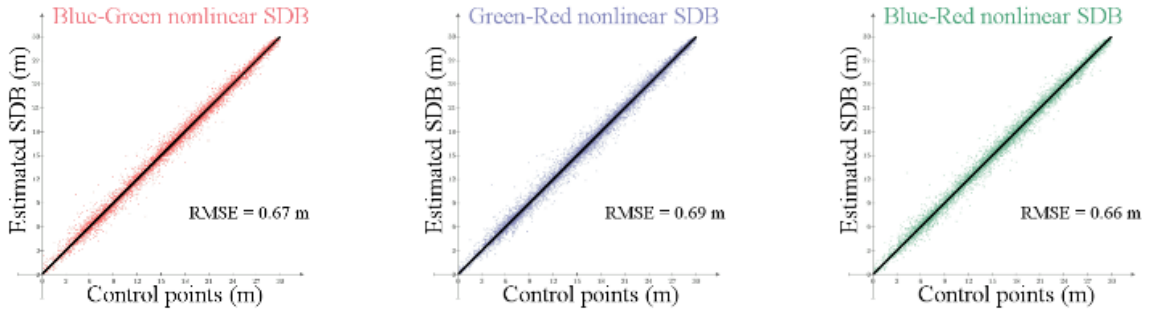

Figure 5.6. Scatter plots of the estimated non-linear SDB depths using blue-green, blue-red, and green-red band ratios against corresponding ALB measurements. The squared cells had 3-pixel side.

In some cases, the squared Jacobian matrix of the partial derivatives of the non-linear equations, $A^T A$, will have zero determinant and will prevent calculating a solution vector. In such scenario, a gap will be formed, even if five or more soundings are available inside the cell. Also, if a cell does not contain five valid control points, then a solution cannot be achieved and will result in a gap instead.

Diffuse attenuation coefficients are based on scaling factors ${m_0}^{ij}$ where i, j represent the bands used by SDB. Traditional linear regression fails since matrix A presents rank two. The solution was achieved using Moore-Penrose pseudoinverse. The results were concentrated in the Blue channel, and were calculated for Landsat 8 images of 2015, 2016 and 2017. Values outside the range [0,1] m^{-1} were neglected.

Bottom returns solution vector X_b, for each cell, presented outliers. Typically, six equations with three parameters (Equation 5.25). To minimize those unexpected results with *Landsat 8* imagery (16-bit dynamic range), solution vector X_b should comply with the digital number ranges between 5,000 to 20,000. These pixel value limits are based on land area range values per channel

for cells size 3x3 pixels (Figure 5.8). The ISODATA algorithm in ArcGIS was defined with a maximum of 10 classes with a 20-pixel minimum threshold per class. All configurations converged to one type of bottom return per study area.

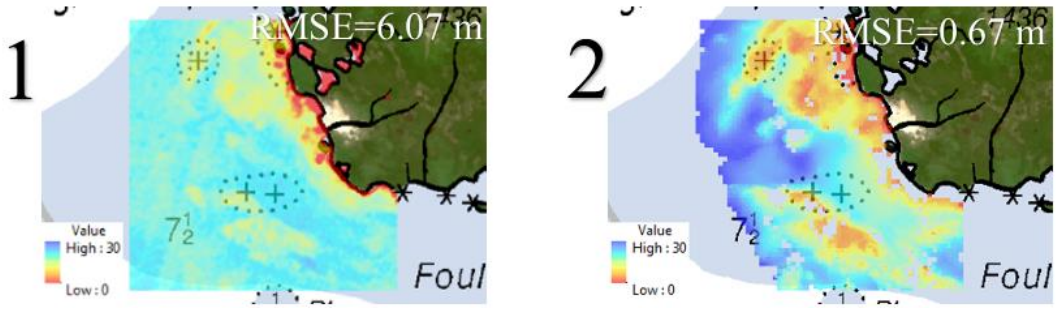

Figure 5.7. (1) traditional linear regression Blue-Green, (2) multiple, nonlinear 3x3 pixels squared window side.

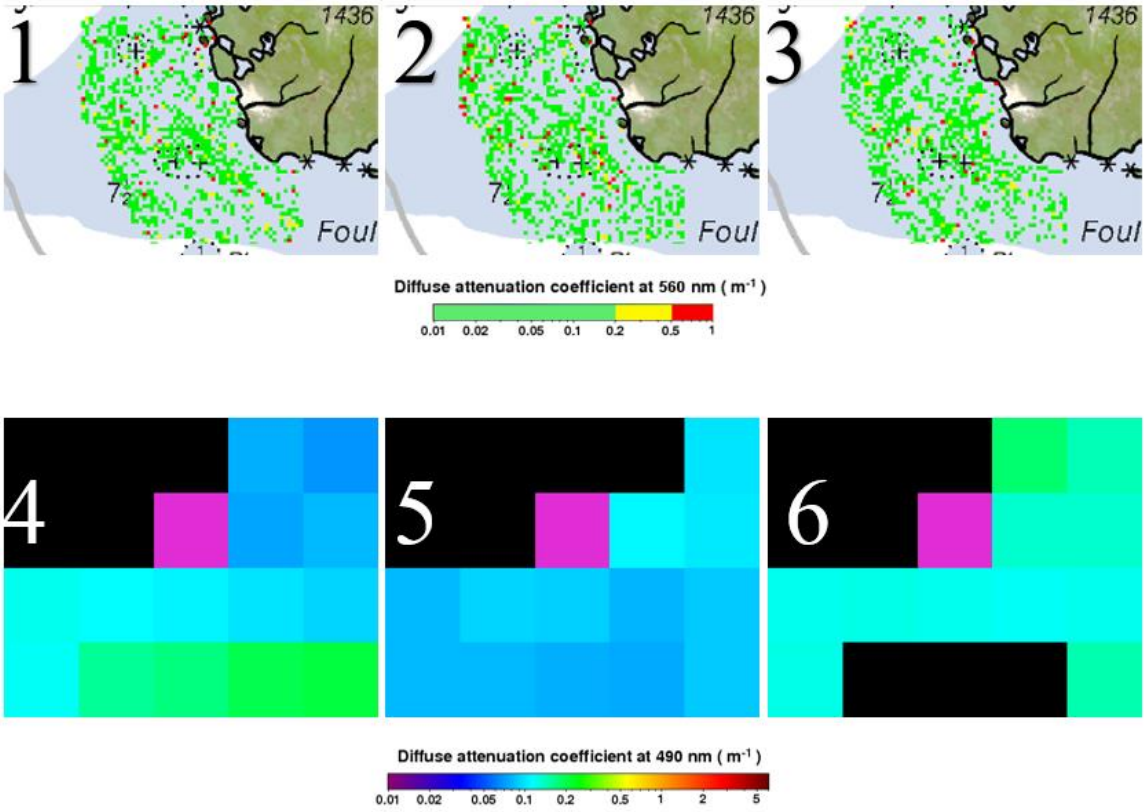

Figure 5.8. Diffuse attenuation coefficient (1) *Landsat 8* 2015, (2) 2016, (3) 2017, (4) Aqua MODIS 2015, (5) 2016 and (6) 2017. The pink pixel represents Simeonof Island on Aqua Modis spatial resolution.

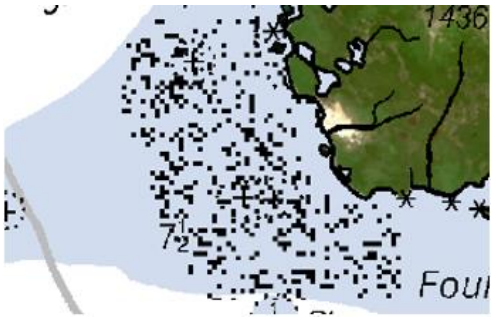

Figure 5.9. ISO cluster results for cell side of 3 pixels.

5.5 Discussion

The multiple, non-linear SDB model provides an enhanced performance compared to the more traditional linear SDB method. This is most noticeable in the very shallow waters (0-2 m), where a linear model does not provide a good correlation to the control points. In deep-waters close to the extinction depth, the multiple, nonlinear SDB method can better detect bottom features than the linear SDB method. This ability to detect a feature is due to the calculations of the water column parameters in multiple, non-linear SDB method that if ignored, could mask (or "blur") the bottom features. By recognizing the water column contributions to the SDB solution, it is possible to achieve a more accurate estimate of the bathymetry in remote areas. However, the multi-nonlinear SDB approach requires more computational resources, and is more dependent on dense distribution of control points. In addition, solving a nonlinear system of equations can become challenging.

A good estimation of the initial approximation vector, $X0$ (Appendix B) is required to produce a meaningful solution vector. This is due to the nature of a linearized RTE solution using

a Taylor expansion. The Jacobian matrix of the partial derivatives of the non-linear equations, *A*, yield incremental vectors ΔX that diverge the solution in the first interaction. Having the invariance of RMSE to linear parameters restricts the correlation analysis to the non-linear parameters. The definition of $X0$ is derived from simulating water column values using a step of 100 (digital number, DN). More consistent results could be achieved using steps smaller than 100 DN.

This decrease in step value "challenge" is due to the amount of processing time required for each cell adjustment calculation. Initial tests showed no noticeable changes on RMSE when using weight matrices associated with control point uncertainty. As such, it is not necessary to use weight matrices when conducting multiple, non-linear adjustments. However, if multiple survey sources are used as control points, weight matrices may be necessary to harmonize the different levels of survey accuracy. In this type of situation, using a weighted correlation should be considered when estimating the water column components for the starting vector $X0$.

The study results also showed that when using traditional linear regression, it is difficult to identify the extinction depth (i.e., optically-deep waters) when using control points (Figures 5.5). The spread of points in shallower depths did not provide a clear indication of linear behavior between estimated depths and control points. A limitation in the multiple, non-linear approach is that it ignores the extinction depth, and forces a local solution that matches the surface generated from the control points (Figure 5.6).

Further research could be performed to investigate a meaningful threshold for the multiple, non-linear SDB method that is close to the extinction depth. This could be achieved by rearranging Equation 5.7 as follows:

$$L(\lambda_1) = \underbrace{\left(L(\lambda_2) - L_w(\lambda_2)\right)e^{\frac{z-m_1}{m_0}}}_{analyze} + L_w(\lambda_1) \qquad 5.26$$

The portion of equation 5.26 selected to be analyzed should be compared against $L(\lambda_1)$, without the water radiance value, $L_w(\lambda_1)$. Optically-deep waters beyond extinction depth are defined as $L(\lambda_1) \approx L_w(\lambda_1)$. The analyzed part needs to represent a minimum significant percentage contribution of $L(\lambda_1)$ (e.g., 10%). Each cell should be analyzed separately. Similarly, another enhancement to the non-linear SDB algorithm is the use of different band pairs. The study results showed that the blue-red band pair performed better than the blue-green and the green-red band pairs (Table 5.1). This was not expected since the best penetration was achieved using the blue-green band. Traditional optimization methods usually disregard the blue-red band pair configuration. Even better RMSE results could be achieved by evaluating all three band pairs RMSE results together over each cell, and selecting depth estimations with minimum quadratic error.

When using the non-linear SDB method, it is also important to avoid receiving complex, infinite, and pole values for depth estimations that may occur. When simulating the water column components, it is necessary to first test if the pair of values would produce negative, zero or infinite values for the log ratio.

Bottom discrimination occasionally produced sparse estimations. The main reason for the gaps was solution vector X_B not complying to [5,000, 20,000] range. Smaller cells presented better spatial distribution. Cell sizes 3x3 converged to the same one class cluster, independent of the number of classes input (5-10). This was expected when observing NOAA raster nautical chart

16540. The area is marked as "Foul, with some rocks." Without bottom sample data, it is believed that one class was likely "rocks" or "rocky area".

Diffuse attenuation coefficient estimation depends on scaling coefficient m_0. Additional convex optimization methods should be investigated to enhance nonlinear solution vector and therefore diffuse attenuation estimative. Figure 5.8 shows the comparison between *Landsat 8* and *Aqua MODIS* estimations. They both showed agreeing results within [0, 0.2] m^{-1} range. A time series analysis should be considered to analyze the variations of this optical characteristic.

When solving Equation 5.25, all equations that composed Jacobian matrix A_b and observation vector L_b were assumed the same importance. An investigation on a weight matrix may yield better bottom estimation.

The ALB survey was conducted in 2009 and the L8 imagery used was from 2016. Ideally a survey from 2016 would be a more useful external benchmark to compare with the multi-non-linear SISDB. In the absence of such survey, it would be interesting to have this procedure tested under such controlled conditions to verify potential bias due to the changes on cell size for depth estimation. Also, bottom samples would be useful to check the ISODATA cluster classification. Ideally a training set would provide a more robust classification. It would be worthwhile to check the performance of this method using higher resolution imagery, such as *Worldview 2* or 3 in areas where ALB survey presented less data gaps.

For remote locations where no control points are available, it is possible to use the four non-linear parameters for each pixel, and derive a potential solution by using multiple images (i.e., multiple spectral observations) at the same location. For this process, depth becomes the 5th parameter in the non-linear adjustment whereby tide and wave height per pixel comprise the

observation matrix. Combining the channels into pairs based on multi-temporal images could potentially provide a solution without control points. To solve this problem, depth, water column components, bottom returns, and diffuse attenuation coefficients would need to be considered constant along time. As such, the time interval among images would need to be small enough to comply with such stable environment assumption.

CHAPTER 6

SUMMARY AND CONCLUSIONS

My three-part investigation (i.e., three separate, but related studies) focused on enhancing the use and capabilities of SDB approach to provide cartographers and hydrographers with an efficient and reliable means to derive near-shore bathymetry in poorly or outdated survey areas. Using a combination of image-processing techniques and time-series analysis, three study objectives were pursued.

6.1 Study 1 – Provide a full estimation of total propagated uncertainty (TPU)

For this study, the limitations of the two most common optimization algorithms used in SDB approaches (i.e., Stumpf and Dierssen) were investigated. A process was developed for SISDB TPU that considers the uncertainties related to control points, the radiometric quality of the satellite imagery, and the image processing steps used to calculate SDB. The process also included a means of vertical referencing to chart datum. Based on the empirical work of previous studies, it is assumed that the horizontal uncertainty of the SDB procedure is the same as the reported horizontal uncertainty of the *Landsat 8* imagery metadata. As such, the primary focus of this study was on the total vertical uncertainty TVU. As part of the evaluation, a new approach was developed to calculate the vertical uncertainty without the need to manually find an optically-deep water area within the image, or the need to use Monte-Carlo simulations.

The performance of various SDB configurations (i.e., pre-processing algorithms applied to the imagery, control point quality, and control point distribution over the study site) was quantified by comparing estimated depths and uncertainties to observed ALB data. Based on the results obtained at two study sites (Cape Ann, MA and Ft Myers, FL), similar performance was observed for both the Stumpf and the Dierssen models when using the same configuration. The best performing SDB configuration was achieved using low-pass filter (e.g., kernel size 3x3) with ALB control points at 100% coverage that were distributed over the entire study site.

To reduce depths and TVU to optimal values, recent survey data should be used rather than chart soundings or high-quality (i.e., IHO S-44 order 1b) legacy data. In particular, a recent survey (e.g., SBES lines) becomes an effective solution to provide useful depth information when applied to the SDB procedure. Ideally, the survey data should be collected shortly before or after the acquisition time of satellite imagery. Overall, the SDB approach using *Landsat 8* imagery provides a cost-efficient reconnaissance tool that can be used worldwide. However, this remote sensing-based hydrographic survey reconnaissance tool is not a replacement for traditional hydrographic survey technologies (e.g., ALB and SBES and MBES) that provide depth measurements at a cm-level accuracy.

6.2 Study 2 – Develop a means for change detection in dynamic shallow areas

In this study, a change detection process was developed for identifying the location and movement of dynamic shallow areas in riverine environments. Two river entrances were evaluated as study sites using multiple satellite imagery scenes over several years: Yukon River (Alaska, USA) and Amazon River (Brazil). Using digital image processing techniques, shoal features were identified in both study sites, and their translational and orientation trends were calculated. In addition, a method was developed to predict the location of the shoal features into the future with respect to the acquisition date of the last satellite imagery available over the study site.

The change detection process includes the use of Dierssen's log ratio model on multiple satellite images over the study site, and extraction of a feature of interest using Canny edge detection from each imagery log ratio. The extracted feature is then generalized and fitted into a defined topological feature (i.e., ellipse). By using multiple satellite imagery data over a period of years, a time-series is generated for the shoal feature's location based on the parameters for each of the extracted ellipses. In addition, a prediction of the shoal features' location, orientation, and flattening variations are calculated using linear regression models and statistical analysis.

The results of this study demonstrated the ability to update the location of shoal areas in remote locations without the need to vertically reference the SDB ratio model to chart datum. The generation of a well-defined topological feature (e.g., an ellipse) provides the capability to chart dynamic shoal areas, and predict their movement over time. However, it is important to recognize that the ability to predict future changes over longer time- periods (>5-7 years) may be constrained due to limited amount of satellite scenes over a multi-year period. Although there is a high repetition rate of the satellite coverage over a given site, environmental conditions such as

persistent cloud coverage, or surface ice, can limit the frequency of usable images. Also, the dynamic behavior and the shape of shoal areas may change over time due to significant climate-change events (e.g., global warming, major storms) or human activities (e.g., hydro-electric dams).

Based on the results of this study, it is possible to extend the adequacy of the charted features for river navigation. By stacking a time-series with predicted location of a feature into the future, it is possible to predict the near future position of the shoal area. In addition to charting applications, the study results can also be used for short-term applications such as notice to mariners for vessels transiting the river.

6.3 Study 3 – Develop non-linear approach for more accurate depth estimations

For this study, a SDB approach was developed to estimate depth in non-uniform conditions from a linear model into a full, non-linear SDB model. In linear SDB models, it is assumed that water column and bottom conditions are uniform and the water contribution for the observed radiance is negligible. The non-linear model takes into account water column effects that enable an improved means for bottom discrimination. Those are not accounted for in a SDB model using a linear regression. Using satellite imagery acquired over Simeonof Island, AK, it was possible to estimate the physical properties of the water column over the study site by comparing the results from non-linear SDB model to control points collected by ALB surveys.

Dierssen's SDB model was further developed into a non-linear version where the variability in water column components were calculated by subdividing study site into small cells of 3x3 pixels. Each cell was modeled individually, and then adjusted to its control points depending

on the cell size. Unlike traditional linear regression where only two parameters are calculated to estimate depths, the non-linear SDB presents hundreds of parameters.

The non-linear adjustment for each cell first requires a good estimation of a starting solution vector. Taking the correlation between non-linear log ratio and control points, simulation method was used to estimate the water column components. A linear regression was then conducted to calculate the remaining parameters which composed the initial solution vector. These values were then used to start an interactive adjustment for the non-linear case. Using the quadratic sum of the residuals as a threshold, the solution vector was achieved when no further convergence occurred.

Using the multiple, non-linear parameters for all cells, diffuse attenuation and bottom return estimations were based on the solution vectors of non-linear adjustment for all three bands pair combinations. The relationship between land areas in the different channels was also considered in the bottom returns estimation.

6.4 Future Research

Collectively, the results of these three studies can be regarded as improved methods that enhance the use SDB for hydrographic applications. However, before mapping and charting organizations can implement the results of these three studies, the methods and procedures that are described will need to be adjusted to available resources and standards. While there are many commercial software tools that can be used (e.g., *ArcGIS, ERDAS, ENVI, MAPLE, MATLAB, MATHCAD*) as well as Open Source tools (e.g., *QGIS, GRASS, SAGA,* and *R),* it will likely be commercial companies that specialize in hydrographic products and services (e.g., *CARIS, IIC Technologies, QPS*) that will develop new software applications. Ideally, some of CCOM's Industrial Partners may decide do this.

Like most scientific investigations, the results of these three studies are not complete, and indicate the need for further research in several areas.

6.4.1 Full development of the TVU model

In the first study, the TVU model is primarily dependent on the quality of the satellite imagery. This TVU model employed an analytical approach using the Special Law of Propagation of Variances (SLOPOV). Although it overcomes some of the limitations of using Monte Carlo estimations (Pe'eri et al., 2014), this study assumes that all sources of uncertainty in the linear SDB calculations are Gaussian distributed. It is possible to further enhance the TVU calculation by characterizing the uncertainties with other distributions that may be more fitting to describe the uncertainty. In addition, another improvement would be to subdivide the area in small cells and

use a non-linear model to estimate bathymetry. Such model would consider non-uniform water column and bottom conditions, as described in the third study.

6.4.2 Selection of topological features for describing dynamic shoals

In the second study, change detection and prediction of shoals moving along rivers were described using ellipses. The benefits of using an ellipse is that this topological feature can approximate the general shape of the feature and its center using relatively simple math. However, polygons or more complex shapes may better describe a shoal boundary and its center of mass. Also, a more complex polygon could be developed, avoiding overlapping the shoreline or river banks. In addition, investigation on automatic canny edge detection parameters need to be conducted.

6.4.3 Optical properties of the water column and the bottom

In the third study, the optical properties of the water column were inferred from the non-linear SDB model. Using more rigorous calculations based on solution derived from the Radiative Transfer Equations could provide a more accurate and comprehensive suite of water column and bottom indicators that can be used for oceanographic and benthic studies. Such parameters can include: diffuse attenuation coefficients, turbidity, chlorophyll concentrations, bottom sediments, vegetation, and more.

The non-linear solution was based on Least Squares Method. It is recommended to investigate this problem using other convex optimization methods, which potentially would reduce the dependency on the initial vector and improve processing time.

The extinction depth should be addressed assuring meaningful outcomes from nonlinear SDB. A potential approach was presented on Discussion section of Chapter 5, but needs to be fully investigated.

Diffuse attenuation variability along time should be examined, especially on areas where atmospheric conditions enable high rates of imagery acquisition. Other pseudoinverse algorithms should be explored in order to minimize losses in the least squares performance.

6.4.4 Combining the non-linear model and multiple satellite scenes

The approach used in the third study to extract four optical parameters (i.e., water column components, bottom returns and diffuse attenuation coefficients) was to divide the study area into small cells. However, the optical properties of the water column are considered constant along time and do not take into account any temporal contributions, such as tides or currents. The use of depth measurements and multiple images acquired over a period about five (5) years would allow inferring the dynamic water column conditions over the study site.

Another potential research topic based on using multiple images is to estimate bathymetry without control points. It is possible to use the four non-linear parameters for each pixel, and derive a potential solution by using multiple images (i.e., multiple spectral observations) at the same location. As such, depth becomes the 5th parameter in the non-linear adjustment whereby tide and

wave height per pixel comprise the observation matrix. Combining the channels into pairs based on multi-temporal images would potentially provide a solution without control points. To solve this problem, depth, water column components, bottom returns, and diffuse attenuation coefficients would need to be considered constant along time. As such, the time interval among images would need to be small enough to comply with such stable environment assumption.

LIST OF REFERENCES

Ahlgren, P., Jarneving, B. and Rousseau, R. (2003). Requirement for a Cocitation Similarity Measure, with Special Reference to Pearson's Correlation Coefficient. Journal of the American Society for Information Science and Technology, 54 (6): 550-560.

Andréfouët, S., Muller-Karger, F. E., Hochberg, E. J., Hu, C. and Carder, K. L. (2001). Change detection in shallow coral reef environments using Landsat 7 ETM+ data.. Remote Sensing of Environment, 78: 150–162.

Bachmann, C., Montes, M., Parrish, C., Fusina, R., Nichols, R., Li, R., Hallenborg, E., Jones, C., Lee, K., Sellars, J., White, S. and Fry, J. (2012). A dual-spectrometer approach to reflectance measurements under sub-optimal sky conditions. Optics Express 20: 8959–8973.

Ball, G. H. and Hall, D. J. (1965). ISODATA, a novel method of data analysis and pattern classification. Stanford Research Institute, Menlo Park.

Bramante, J.F., Raju, D.K., and Sin, T.M. (2013). Multispectral derivation of bathymetry in Singapore's shallow, turbid waters, Int. J. Rem. Sens. 34:6, 2070-2088

Brabets, T. P., Wang, B., and Meade, R. H. (2000). Environmental and hydrologic overview of the Yukon River Basin, Alaska and Canada: US Geological Survey: Anchorage, v. Water-Resources Investigations Report 99-4204. pp. 106.

Brando, V.E. and Dekker, A.G. (2003). Satellite hyperspectral remote sensing for estimating coastal water quality. IEEE Transactions on Geoscience and Remote Sensing, 41 (6): 1378–1387.

Brüllmann, D. D. and d'Hoedt, B. (2011). The modulation transfer function and signal-to-noise ratio of different digital filters: a technical approach. Dentomaxillofacial Radiology 40: 222-

229.

Canny, J., (1986). A computational approach to edge detection. IEEE Trans. Pattern Anal. Mach. Intell. PAMI-8 (6): 679–698.

Cochran, W.G. (1977). Sampling Techniques, 3rd ed. Wiley, New York.

Cunha, A. C., Brito, D. C., Brasil Junior, A. C., Pinheiro, L. A. R., Cunha, H. F. A., Krusche, A. V. (2012). Challenges and Solutions for Hydrodynamic and Water Quality in Rivers in the Amazon Basin. In: Harry Edmar Schulz; André Luiz Andrade Simões; Raquel Jahara Lobosco. (Org.). Hydrodinamics: Natural Water Bodies. Book3. 1ed. Janeza Trdine 9, 51000 Rijeka, InTech - Croacia, v. 3: 67-88.

Czapla-Myers, J., McCorkel, J., Anderson, N., Thome, K., Biggar, S., Helder, D., Aaron, D., Leigh, L. and Mishra, N. (2015). The ground-based absolute radiometric calibration of Landsat 8 OLI. Remote Sens. 7: 600–626.

Department of Commerce, Community and Economic Development, Division of Economic Development. (2014). Lower Yukon river regional port project: situational analysis and potential impacts.

Dierssen, H. M., Zimmerman, R. C., Leathers R. A., Downes, T. V. and Davis, C. O. (2003). Ocean color remote sensing of seagrass and bathymetry in the Bahamas Banks by high-resolution airborne imagery. Limnol. and Oceanogr. 48: 444–455.

Dustan, P., Dobson, E. and Nelson, G. (2001). Landsat Thematic Mapper: detection of shifts in community composition of coral reefs.. Conservation Biology, 15: 892–202.

Environment Outlook in Amazonia – Geo Amazonia. (2009). United Nations Environment Programme (UNEP); Amazon Cooperation Treaty Organization (ACTO).

Flener C., Lotsari, E., Alho, P. and Kayhko, J. (2012). Comparison of empirical and theoretical remote sensing based bathymetry models in river environments. River Res. Applic. 28: 118–133.

Gao, B. C. (1996). NDWI – A Normalized Difference Water Index for Remote Sensing of Vegetation Liquid Water from Space. Remote Sens. Environ. 58: 257–266.

Gemael, C. (2015). Introdução ao ajustamento de observações: aplicações geodésicas. Curitiba: Editora da UFPR. pp. 430. [in Portuguese]

Gonzalez, R. C. and Woods, R. E. (2017). Digital Image Processing. 4th Edition, Prentice Hall.

Grodsky, S. A., Reverdin, G., Carton, J. A. and Coles, V. J. (2014). Year-to-year salinity changes in the Amazon plume: Contrasting 2011 and 2012 Aquarius/SACD and SMOS satellite

data. Remote Sensing of Environment. 140: 14-22.

Guenther, G. C. (1985). Airborne Laser Hydrography: System Design and Performance Factors, NOAA Professional Paper Series, National Ocean Service 1, National Oceanic and Atmospheric Administration, Rockville, MD

Hogfe, K. R., Wright, D. J. and Hochberg, E.J. (2008). Derivation and integration of shallow-water bathymetry: implications for coastal terrain modeling and subsequent analyses. Marine Geodesy 31: 299–317.

Ingargiola, J., Oliver, C., Gilpin, J., and Saifee, S. (2013). Mitigation Assessment Team Report: Hurricane Charley in Florida. Appendix E: The History of Hurricanes in Southwest Florida. Federal Emergency Management Agency. p. E-2.

International Hydrographic Organization (IHO). (2008). IHO standards for hydrographic survey: Special Publication Nº. 44 (5th edition), International Hydrographic Bureau, Monaco, pp. 36.

International Hydrographic Organization (IHO). (2011). IHO manual on hydrography: Publication C-13 (1st edition), International Hydrographic Bureau, Monaco, pp. 46.

Jerlov, N.G. (1951). Optical studies of ocean water. In: Rep. Swedish Deep-sea Exp. H. Pettersson, ed., 3(1): 1-69.

Jerlov, N. G. (1961). Optical measurements in the eastern North Atlantic. Medd. Oceanogr. Inst. Göteborg, 38B: 4-40.

Jerlov, N.G. (1976). Marine Optics, New York, NY, Elsevier Scientific Publication.

Ji L., Zhang L., Wylie B. (2009). Analysis of dynamic thresholds for the normalized difference water index. Photogramm Eng Remote Sens. 75: 1307–1317.

Kampia, A., Klemm, A., Pe'eri, S., Barber, J.E., Merke, D. and Athens, E. (2016). Yukon River Prototype Electronic Charts Using Satellite Derived Bathymetry. Canadian Hydrographic Conference.

Kanno, A., Koibuchi, Y. and Isobe, M. (2011). Statistical combination of spatial interpolation and multispectral remote sensing for shallow water bathymetry. Geoscience and Remote Sensing Letters, IEEE, vol. 8, pp. 64-67.

Kirkpatrick, G.J., Orrico, C., Moline, M.A., Oliver, M. and Schofield, O.M. (2003). Hyperspectral absorption measurements of colored dissolved organic material in aquatic systems. Applied Optics, 42(33): 6564–6568.

Lamb, D. and Verlinde, J. (2011). Physics and Chemistry of Clouds. 1st Edition, Ed. Cambridge

University Press, pp 600.

LeDrew, E. F., Holden, H., Wulder, M. A., Derksen, C. and Newman, C. (2004). A spatial statistical operator applied to multidate satellite imagery for identification of coral reef stress. Remote Sensing of Environment, 91: 271–279.

Lee, M. and Tuell, G. H. (2003). A Technique for Generating Bottom Reflectance Images from SHOALS Data. U.S. HYDRO 2003, New Orleans, LA.

Li, P., Jiang, L. and Feng, Z. (2014). Cross-Comparison of Vegetation Indices Derived from Landsat-7 Enhanced Thematic Mapper Plus (ETM+) and Landsat-8 Operational Land Imager (OLI) Sensors. Remote Sens. 6(1): 310-329. doi:10.3390/rs6010310

Liceaga-Correa, M. A., and Euan-Avila, J. I. (2002). Assessment of coral reef bathymetric mapping using visible Landsat Thematic Mapper data. International Journal of Remote Sensing, Vol. 23, Nº. 1: 3-14.

Louchard, E.M., Reid, R.P., Stephens, F.C., Davis, C.O., Leathers, R.A. and Downeset, T.V. (2003). Optical remote sensing of benthic habitats and bathymetry in coastal environments at Lee Stocking Island, Bahamas: A comparative spectral classification approach. Limnol. Oceanogr., 48: 511–52.

Lyzenga, D. R. (1978). Passive remote sensing techniques for mapping water depth and bottom features. Appl. Optics, 17: 379–383.

Lyzenga, D. R. (1985). Shallow-water bathymetry using combined lidar and passive multispectral scanner data. Int. J. Rem. Sens. 6: 115–125.

Lyzenga, D. R., Malinas, N. P. and Tanis, F. J. (2006). Multispectral bathymetry using a simple physically based algorithm. IEEE Trans. Geo. Rem. Sens. 44: 2251–2259.

Mahiny, A. S., and Turner, B. J. (2007). A comparison of four common atmospheric correction methods. Photogrammetric Engineering and Remote Sensing, 73: 361-368.

Maritorena, S., Morel, A. and Gentili, B. (1994). Diffuse reflectance of oceanic shallow waters: Influence of water depth and bottom albedo, Limnology and Oceanography, 39: 1689-1703.

Matsunaga, T., Hoyano, A. and Mizukami, Y. (2001). "Monitoring of coral reefs on Ishigaki Island in Japan using multitemporal remote sensing data.". In Hyperspectral Remote Sensing of the Ocean Edited by: Frouin, R. J, Kawamura, H and Kishino, M. Vol. 4154: 212–222. Proceedings of SPIE.

McFeeters, S.K. (1996). The use of the Normalized Difference Water Index (NDWI) in the delineation of open water features. Int. J. Remote Sens. 17: 1425–1432.

McFeeters S. K. (2013). Using the Normalized Difference Water Index (NDWI) within a Geographic Information System to Detect Swimming Pools for Mosquito Abatement: A Practical Approach. Remote Sensing. 5 (7): 3544-3561. doi: http://dx.doi.org/10.3390/rs5073544

Mikhail, E. M. (1976). Observations and Least Squares. University Press of America, New York.

Mishra, D. R., Narumalani, S., Rundquist, D. and Lawson, M.(2005). Characterizing the vertical diffuse attenuation coefficient for downwelling irradiance in coastal waters: Implications for water penetration by high resolution satellite data. ISPRS Journal of Photogrammetry and Remote Sensing, 60 (1): 48 – 64. doi:10.1016/j.isprsjprs.2005.09.003

Mishra, N., Haque, M. O., Leigh, L., Aaron, D., Helder, D. and Markham, B. (2014). Radiometric Cross Calibration of Landsat 8 Operational Land Imager (OLI) and Landsat 7 Enhanced Thematic Mapper Plus (ETM+), Remote Sensing Journal (6): 12619-12638.

Mobley, C. D. 1994. Light and water: radiative transfer in natural waters. Academic Press, Inc.

Mobley, C.D., D. Stramski, W. P. Bisset, and E. Boss, 2004. Optical modeling of ocean waters: Is the case-1 case-2 still useful? Oceanography 17 (2): 60-67

Moura, R. L., Amado-Filho, G. M., Moraes, F. C., Brasileiro, P. S., Salomon, P. S., Mahiques, M. M., Bastos, A. C., Almeida, M. G., Silva, J. M., Araujo, B. F., Brito, F. P., Rangel, T. P., Oliveira, B. C. V., Bahia, R. G., Paranhos, R. P., Dias, R. J. S., Siegle, E., Figueiredo, A. G., Pereira, R. C., Leal, C. V., Hajdu, E., Asp, N. E., Gregoracci, G. B., Neumann-Leitao, S., Yager, P. L., Francini-Filho, R. B., Froes, A., Campeao, M., Silva, B. S., Moreira, A. P. B., Oliveira, L., Soares, A. C., Araujo, L., Oliveira, N. L., Teixeira, J. B., Valle, R. A. B., Thompson, C. C., Rezende, C. E. and Thompson, F. L. (2016). An extensive reef system at the Amazon River mouth, Science Advances Journal, vol 2, issue 4, doi: http://advances.sciencemag.org/cgi/doi/10.1126/sciadv.1501252. Last visited 02/16/2017.

National Oceanic and Atmospheric Administration (NOAA). (2013). Service Assessment: Hurricane/Post-Tropical Cyclone Sandy October 22–29, 2012. United States Department of Commerce, NOAA National Weather Service. pp 66. doi: http://www.nws.noaa.gov/os/assessments/pdfs/Sandy13.pdf (last date accessed: 17 Dec, 2014).

Palandro, D., Andréfouët, S., Muller-Karger, F. E., Dustan, P., Hu, C. and Hallock, P. (2003). Detection of changes in coral reef communities using Landsat-5 TM and Landsat-7 ETM+ data. Canadian Journal of Remote Sensing, 29: 201–209.

Park, J. Y., Ramnath, V., Feygels, V., Kim, M., Mathur, A., Aitken, J. and Tuell, G. (2010). Active-Passive Data Fusion Algorithms for Seafloor Imaging and Classification from CZMIL Data. In SPIE Proceedings on Algorithms and Technologies for Multispectral, Hyperspectral, and Ultraspectral Imagery XVI Vol. 7695, Orlando, FL. doi:10.1117/12.851991

Parrish, C.E. (2012). Chapter 6: Shoreline Mapping in Advances in Mapping from Remote Sensor Imagery: Techniques and Applications (Yang, X. and Li, J., Eds.), CRC Press, Taylor and Francis Group, Boca Raton, Florida: 145-168.

Pastol, Y. (2011). Use of Airborne LIDAR Bathymetry for Coastal Hydrographic Surveying: The French Experience. Journal of Coastal Research: Special Issue 62: 6 – 18.

Pe'eri, S. and Long, B. (2011). Lidar Technology Applied in Coastal Studies and Management, Journal of Coastal Research, Volume Special Issue 62: 1-5.

Pe'eri, S., Madore, B., Alexander, L., Parrish, C. E., Armstrong A., Azuike, C. and Tetteh, E. (2013). LANDSAT 8 Satellite-Derived Bathymetry, in The IHO-IOC GEBCO Cook Book, Edition 11.1.13 (Editor: Marks, K.), International Hydrographic Office (IHO)/ International Ocean Commission (IOC), Monaco Cedex, Monaco, IHO Publication B-11 and IOC Manuals and Guides, 63: 243-304.

Pe'eri, S., Parrish, C. E., Azuike, C., Alexander, L. and Armstrong, A. (2014), Satellite Remote Sensing as a Reconnaissance Tool for Assessing Nautical Chart Adequacy and Completeness, Marine Geodesy, 37(3): 293-314.

Pe'eri, S., Madore, B., Nyberg, J., Snyder, L., Parrish, C. E. and Smith, S. (2016). Identifying Bathymetric Differences over Alaska's North Slope using a Satellite-derived Bathymetry Multi-temporal Approach. Journal of Coastal Research: 56-63. doi: http://www.jstor.org/stable/44072540

Pe'eri, S., Morrison, J. R., Frederick, S., Mathieson, A., Lippmann, T. C. (2016). Eelgrass and Macroalgal Mapping to Develop Nutrient Criteria in New Hampshire's Estuaries Using Hyperspectral Imagery. Journal of Coastal Research: 209-218. doi: http://www.jcronline.org/doi/pdf/10.2112/SI76-018

Philpot, W. D. (1989). Bathymetric mapping with passive, multispectral imagery. Appl. Optics 28:1569–1578.

Philpot, W.D., Davis, C.O., Bissett, W.P., Mobley, C., Kohler, D.D.R., Lee, Z.P., Snyder, W., Steward, R.G., Gould, R. and Arnone, R. (2004). Bottom characterization from hyperspectral image data. Oceanography, 17(2): 76-85.

Polcyn, F.C., and Rollin, R.A. (1969). Remote Sensing Techniques for the Location and Measurement of Shallow Water Features. Willow Run Laboratories Report 8973-10-P, University of Michigan.

Polcyn, F. C. and Lyzenga, D. R. (1973), Calculations of water depth from ERTS-MSS data, in Proceedings, Symposium on Significant Results from ERTS-1, NASA Spec. Publ. SP-327.

Preisendorfer, R. W. (1976). Hydrologic Optics, vol. 1, Introduction, Natl. Tech. Inf. Serv., Springfield, VA.

Psusty, N. P. and Silveira, T. M. (2009). Geomorphological evolution of estuaries: The dynamic basis for morpho-sedimentary units in selected estuaries in the northeastern United States. Marine Fisheries Review71: 34-45.

Smith, R. C. and Baker, K. S. (1981). Optical properties of the clearest natural waters (200–800 nm). Appl. Opt. 20: 177–184.

Storey, J., Choate, M. and Lee, K. (2014). Landsat 8 Operational Land Imager On-Orbit Geometric Calibration and Performance, Multidisciplinary Digital Publishing Institute. Remote Sens. 2014, 6(11): 11127-11152

Stumpf, R. P., Holderied, K. and Sinclair, M. (2003). Determination of water depth with high-resolution satellite imagery over variable bottom types, Limnol. Oceanogr. 48: 547–556.

Su, H., Liu, H. and Heyman, W.D. (2008). Automated derivation of bathymetric information from multi-spectral satellite imagery using a non-linear inversion model, Mar. Geod. 31: 81–298.

Su, H., Liu, H., Wang, L., Filippi, A. M., Heyman, W. D. and Beck, R. A. (2014). Geographically Adaptive Inversion Model for Improving Bathymetric Retrieval From Satellite Multispectral Imagery. Geoscience and Remote Sensing, IEEE Transactions, vol. 52. pp. 465-476.

Su, H., Liu, H., & Wu, Q. (2015) Prediction of Water Depth from Multi-Spectral Satellite Imagery - The Regression Kriging Alternative. IEEE Geoscience and Remote Sensing Letters. 12(12): 2511-2515. doi: 10.1109/LGRS.2015.2489678

Taboga, M. (2012). Lectures on probability theory and mathematical statistics, 2nd Ed. CreateSpace Publishing Platform.

Tournay, J. P. and Quéméneur, P. (2013). De l'image satellite à la spatiocarte marine au SHOM, Annales hydrographiques, Series 6, Vol. 9 (No.778): 25-36.

Tuell, G. and Park, J. Y. (2004). Use of SHOALS bottom reflectance images to constrain the inversion of a hyperspectral radiative transfer model. In: Kammerman G (ed) Proceedigs SPIE vol 5412, Laser Radar and Technology Applications IX. pp. 185–193. doi:10.1117/12.564929.

Tuell, G.H., Ramnath, V., Park, J.Y., Feygels, V., Aitken, J. and Kopelivich, Y. (2005). Fusion of SHOALS bathymetric LIDAR and passive spectral data for shallow water rapid environmental assessment. In Proceedings of the Oceans 2005, Volume 2. pp. 1046–1051.

US Geological Survey. (2016). Landsat 8 (L8) Data Users Handbook. doi: https://landsat.usgs.gov/sites/default/files/documents/Landsat8DataUsersHandbook.pdf

Vanderstraete, T., Goossens, R. and Ghabour, T.K. (2006). The use of multi-temporal Landsat images for the change detection of the coastal zone near Hurghada, Egypt. Int. J. Rem. Sens. 27 (17): 3645–3655.

Vaníček, P. (1995). Introduction to adjustment calculus. Department of Geodesy & Geomatics Engineering University of New Brunswick: Fredericton.

Vogelmann, J. E., Helder, D., Morfitt, R., Choate, M. J., Merchant, J. W. and Bulley, H. (2001). Effects of Landsat 5 Thematic Mapper and Landsat 7 Enhanced Thematic Mapper Plus radiometric and geometric calibrations and corrections on landscape characterization. Remote Sens. Environ. 78:55–70.

Wang, C. K. and Philpot, W.D. (2007). Using airborne bathymetric LiDAR to detect bottom type variation in shallow waters. Remote Sensing of Environment, 106: 123–135. doi:10.1016/j.rse.2006.08.003.

Weisstein, E. W. (2017). Ellipse, From MathWorld— A Wolfram Web Resource. doi: http://mathworld.wolfram.com/Ellipse.html. Last visited on 02/16/2017.

Weisstein, E. W. 2017. Correlation Coefficient, From MathWorld – A Wolfram Web Resource. doi: http://mathworld.wolfram.com/CorrelationCoefficient.html. Last visited on 05/30/2017

Wells, D. E. and Krakiwsky, E. J. (1971). The Method of Least Squares. Department of Survey Engineering, Lecture Notes nº 18, University of New Brunswick, Fredericton.

White, S. A., Parrish, C. E., Calder, B. R., Pe'eri, S. and Rzhanov, Y. (2011). LIDAR-Derived National Shoreline: Empirical and Stochastic Uncertainty Analyses. Journal of Coastal Research: Special Issue 62: 62 – 74.

Wiegmans, B. and Konings, R. (2017). Inland Waterway Transport: Challenges and prospects (Routledge Studies in Transport Analysis), published by Routledge. pp 238.

Yu, Q., Tian, Y.Q., Chen, R.F., Liu, A., Gardner, G.B. and Zhu, W. (2010). Functional linear analysis of in situ hyperspectral data for assessing CDOM in rivers. Photogrammetric Engineering and Remote Sensing, 76(10): 1147–1158.

Zainal, A. J. M., Dalby, D. H. and Robinson, I. S. (1993). Monitoring marine ecological changes on the east coast of Bahrain with Landsat TM. Photogrammetric Engineering and Remote Sensing, 59: 415–421.

APPENDICES

Appendix A – Ellipse fitting

A.1 Mathematical definitions of the topological feature

The topological feature that is used to describe an extracted area from the SDB ratio model is an ellipse. The reasons for using this type of conic are 1) it is a closed geometry, 2) its sensitivity to the dimensions of the feature (e.g., major and minor semi-axis and scaling factors), and 3) its orientation (i.e., rotation angle). The complex geometry derived from edge detection is then simplified by adjusting this topological feature. In this study, both the parametric and quadratic definitions of the ellipse are used. In its parametric form, it is possible to describe a shifted ellipse curve with a center located at ($x0, y0$) that is rotated at angle of θ with respect to the coordinate system (Figure A.1) as follows:

$$x(t) = a \cdot cos(t) \cdot cos(\theta) - b \cdot sin(t) \cdot sin(\theta) + x0$$
$$y(t) = a \cdot cos(t) \cdot sin(\theta) + b \cdot sin(t) \cdot cos(\theta) + y0 \qquad \text{A.1}$$

Where a is the semi-major axis, b semi-minor axis, $x0$ horizontal coordinate of ellipse's center, $y0$ vertical coordinate of ellipse's center, t angle formed between semi-major axis a and segment line defined by any given ellipse point and ellipse center, ranging from 0 to 2π radians, and θ rotation angle between X-axis and semi-major axis a.

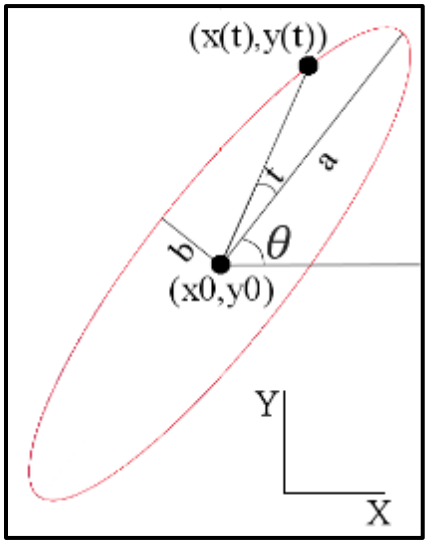

Figure A.1. Parametric description of an ellipse.

The curve of the ellipse can also be described in a quadratic form as (Weisstein, 2017):

$$A \cdot {x_1}^2 + B \cdot x_1 \cdot y_1 + C \cdot {y_1}^2 + D \cdot x_1 + F \cdot y_1 + G = 0 \qquad \text{A.2}$$

The center of the ellipse $(x0, y0)$ will become:

$$x0 = \frac{C \cdot D - B \cdot F}{B^2 - A \cdot C}$$

$$y0 = \frac{A \cdot F - B \cdot D}{B^2 - A \cdot C} \qquad \text{A.3}$$

The semi-major axis, *a*, and the semi-minor axis, *b*, will become:

$$a = \sqrt{2 \cdot \frac{(A \cdot F^2 + C \cdot D^2 + G \cdot B^2 - 2 \cdot B \cdot D \cdot F - A \cdot C \cdot G)}{(B^2 - A \cdot C) \cdot \left[\sqrt{(A-C)^2 + 4 \cdot B^2} - (A + C)\right]}}$$

$$b = \sqrt{2 \cdot \frac{(A \cdot F^2 + C \cdot D^2 + G \cdot B^2 - 2 \cdot B \cdot D \cdot F - A \cdot C \cdot G)}{(B^2 - A \cdot C) \cdot \left[-\sqrt{(A-C)^2 + 4 \cdot B^2} - (A + C)\right]}} \quad \text{A.4}$$

The counterclockwise angle of rotation from the X-axis to the major axis of the ellipse will become:

$$\theta = \begin{cases} 0, if\ (B = 0 \wedge A < C) \\ \frac{\pi}{2}, if\ (B = 0 \wedge A > C) \\ \frac{1}{2} \cdot arctan\left(\frac{2 \cdot B}{A - C}\right), if\ (B \neq 0 \wedge A < C) \\ \frac{\pi}{2} + \frac{1}{2} \cdot arctan\left(\frac{2 \cdot B}{A - C}\right), if\ (B \neq 0 \wedge A > C) \end{cases} \quad \text{A.5}$$

A minimum of 7 points are required to describe the ellipse (A.2) and obtain at least one degree of freedom. However, the quadratic equation can lead to a zero-vector solution. This problem can be solved by forcing one of the coefficients, except for G, to have unit value:

$$(A \quad B \quad C \quad D \quad F \quad G)^T = \left(1 \quad \frac{c_1}{2} \quad c_2 \quad \frac{c_3}{2} \quad \frac{c_4}{2} \quad c_5\right)^T \quad \text{A.6}$$

Thus, reducing the number of variables and allowing the quadratic equation to have a coherent solution.

$$x_1{}^2 + c_1 \cdot x_1 \cdot y_1 + c_2 \cdot y_1{}^2 + c_3 \cdot x_1 + c_4 \cdot y_1 + c_5 = 0 \qquad \text{A.7}$$

This new equation (A.7) allows to determine the ellipse parameters with, at least, 6 points (instead of 7).

A.2 Initial fitting

The adopted procedure to solve a new system of equations is the Least Square Method (LSM) using a parametric adjustment (Vaníček, 1995):

$$\underbrace{\begin{pmatrix} x_1 \cdot y_1 & y_1{}^2 & x_1 & y_1 & 1 \\ \vdots & & & & \vdots \\ x_n \cdot y_n & y_n{}^2 & x_n & y_n & 1 \end{pmatrix}}_{K} \cdot \underbrace{\begin{pmatrix} c_1 \\ \vdots \\ c_5 \end{pmatrix}}_{X} = \underbrace{\begin{pmatrix} -x_1{}^2 \\ \vdots \\ -x_n{}^2 \end{pmatrix}}_{L} \qquad \text{A.8}$$

The solution for vector ***X*** is given by:

$$X = (K^T \cdot K)^{-1} \cdot (K^T \cdot L) \qquad \text{A.9}$$

In this study, the weight matrix is assumed to be an identity matrix since there is no usable information that can quantify the observation vector, L. Horizontal uncertainty (described in the imagery metadata files) is assumed constant for all image pixels. The result from the initial fitting show that the ellipse plot does not contain all the points that compose the extracted feature (Figure A.2).

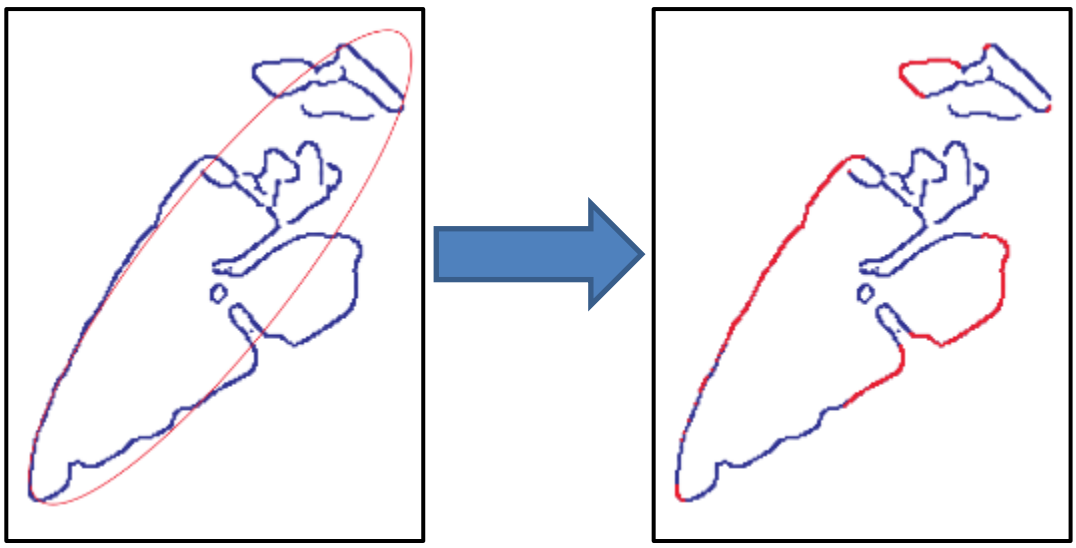

Figure A.2. Ellipse adjusted based on extreme coordinate points, and identification of points outside the first approximation (in red).

A.3 Iterative fitting

To automatically identify all the points that are outside the ellipse solution from the Initial Fitting step, the coordinates of these points are analyzed against a conic geometry (Figure A.3). In addition, it is necessary to solve the general ellipse equation in order to analyze the ellipse's curve against each axis:

$$f(x) = x^2 + x \cdot (c_1 \cdot y_0 + c_3) + (c_2 \cdot {y_0}^2 + c_4 \cdot y_0 + c_5) = 0$$
$$g(y) = y^2 \cdot (c_2) + y \cdot (c_1 \cdot x_0 + c_4) + ({x_0}^2 + c_3 \cdot x_0 + c_5) = 0 \qquad \text{A.10}$$

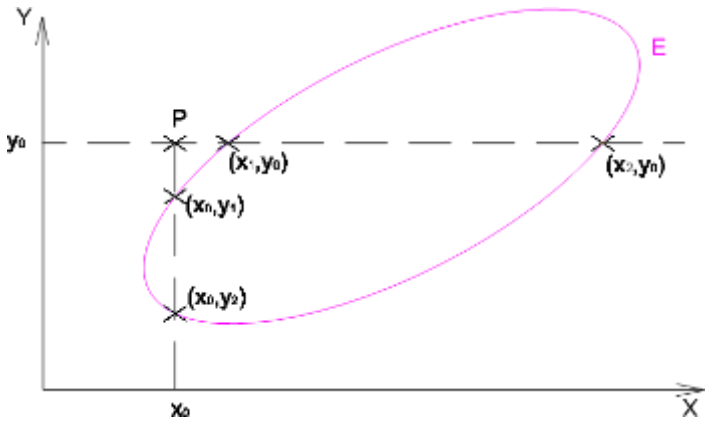

Figure A.3. Checking for points outside the ellipse.

If point $P(x_0, y_0)$ is located outside of the bounds of the ellipse, i.e., $(x_1 : x_2, y_1 : y_2)$, then the points outside of the ellipse must comply with at least one of the following conditions:

$$(x_1, x_2) \in \mathbb{R} \wedge [(x_0 < x_1 \wedge x_0 < x_2) \vee (x_0 > x_1 \wedge x_0 > x_2)] = 1$$
$$(y_1, y_2) \in \mathbb{R} \wedge [(y_0 < y_1 \wedge y_0 < y_2) \vee (y_0 > y_1 \wedge y_0 > y_2)] = 1 \qquad \text{A.11}$$

The points presenting the highest residuals (i.e., distance) to the ellipse curve were selected and re-evaluated. Based on this new dataset, a new ellipse can be defined. In order to include all the extracted area points within an ellipse, an additional interactive analysis using a LSM was implemented. Using the initial ellipse that provides a good preliminary approximation, gradients from the points outside the initial ellipse to ellipse's curve, *E*, are calculated (Appendix A). Normally-projected points, *Q*, based on the gradients on the ellipse curve are extracted and

distances, $\left|\overrightarrow{QP}\right|$, from the points outside the initial ellipse, *P*, to ellipse's curve are calculated (Figure A.4).

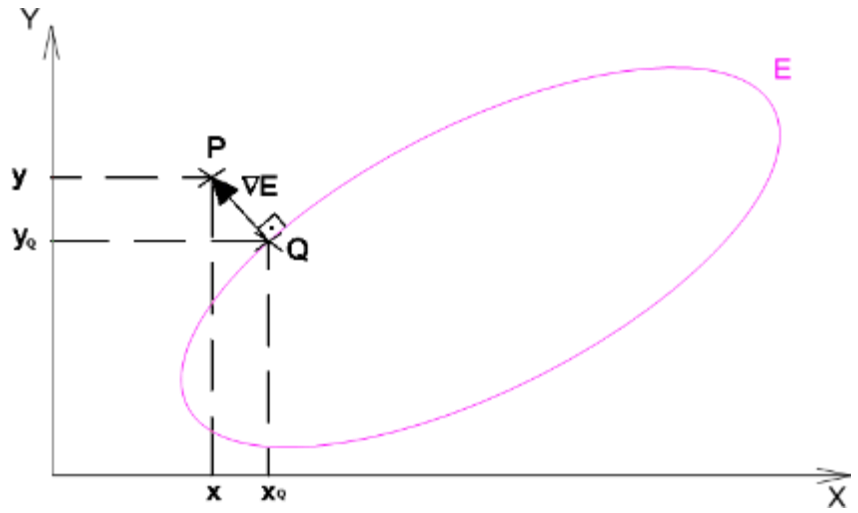

Figure A.4. Projecting feature points into ellipse E along its gradient.

Let $E(x, y)$ be the general ellipse equation:

$$E(x,y) = x^2 + c_1 \cdot x \cdot y + c_2 \cdot y^2 + c_3 \cdot x + c_4 \cdot y + c_5 = 0 \qquad \text{A.12}$$

The gradient can be written as:

$$\overrightarrow{\nabla E} = \left(\frac{\partial E(x,y)}{\partial x}, \frac{\partial E(x,y)}{\partial y}\right) = (2 \cdot x + c_1 \cdot y + c_3\,, 2 \cdot y \cdot c_2 + c_1 \cdot x + c_4) \qquad \text{A.13}$$

Since $\left|\overrightarrow{\nabla E}\right| = k \cdot \left|\overrightarrow{QP}\right|$, where $k \neq 0$:

$$x_Q(k) = \frac{(x - k \cdot c_3) \cdot (k \cdot 2 \cdot c_2 + 1) + [-(k \cdot c_1) \cdot (y - k \cdot c_4)]}{(k \cdot 2 \cdot c_2 + 1) \cdot (k \cdot 2 + 1) - (k \cdot c_1)^2}$$

$$y_Q(k) = \frac{(k \cdot c_3 - x) \cdot (k \cdot c_1) + (k \cdot 2 + 1) \cdot (y - k \cdot c_4)}{(k \cdot 2 \cdot c_2 + 1) \cdot (k \cdot 2 + 1) - (k \cdot c_1)^2} \qquad \text{A.14}$$

By substituting A.14 into A.12 you get:

$$h(k) = E\big(x(k), y(k)\big) = 0 \qquad \text{A.15}$$

The *k* value that satisfies $h(k) = 0$ enables a calculation of P coordinate values *(x,y)*. A traditional Newton-Raphson is used in order to determine the $h(k)$ roots that satisfies $h(k) = 0$ and enables a calculation of *P(x,y)* where:

$$k = k_0 - \frac{h(k_0)}{\left.\frac{dh(k)}{dk}\right|_{k=k_0}} \qquad \text{A.16}$$

Since this method is interactive, it depends on establishing a good initial estimate for k_0. As a logical starting point, zero was selected to be the starting value.

Points that contained the highest residuals after adjusting the first ellipse were identified, and only the ones outside the ellipse were selected. These points were grouped according to its quadrant (assuming that the origin of original ellipse to be the center). A maximum of 8 points per quadrant were retained (Figure A.6).

To calculate the new extreme points, coordinates were developed using ellipse gradient analysis (Figure A.5). To comply with conditions described in A.11, the new adjusted ellipse must have no feature point outside it. The point coordinates were then extended along the gradient vector using (Figure A.5):

$$x' = x + (p) \cdot cos(\alpha_i)$$
$$y' = y + (p) \cdot sin(\alpha_i) \qquad \text{A.17}$$

Where α_i is the angular orientation based on the gradient vector, and p is an integer value between [1,100], representing the pixel shift value that increases until the new adjusted ellipse.

Based on the new extreme points coordinates (point N, Figure A.5), the new adjusted ellipse provides a more robust and meaningful representation of all original feature points. An Illustration of the Iterative fitting step is presented in Figure A.6.

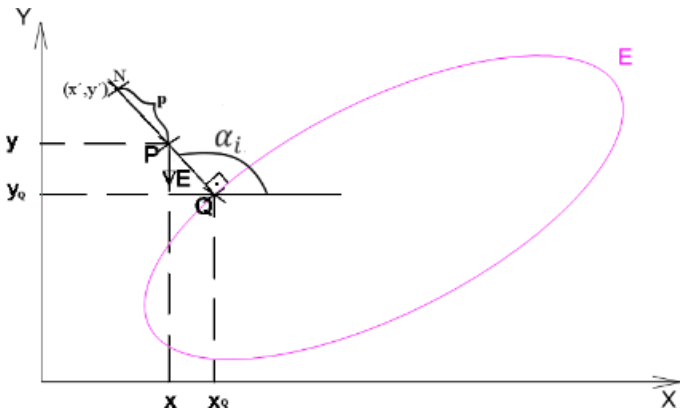

Figure A.5. Calculating the new extreme points (point N) coordinates using ellipse gradient analysis.

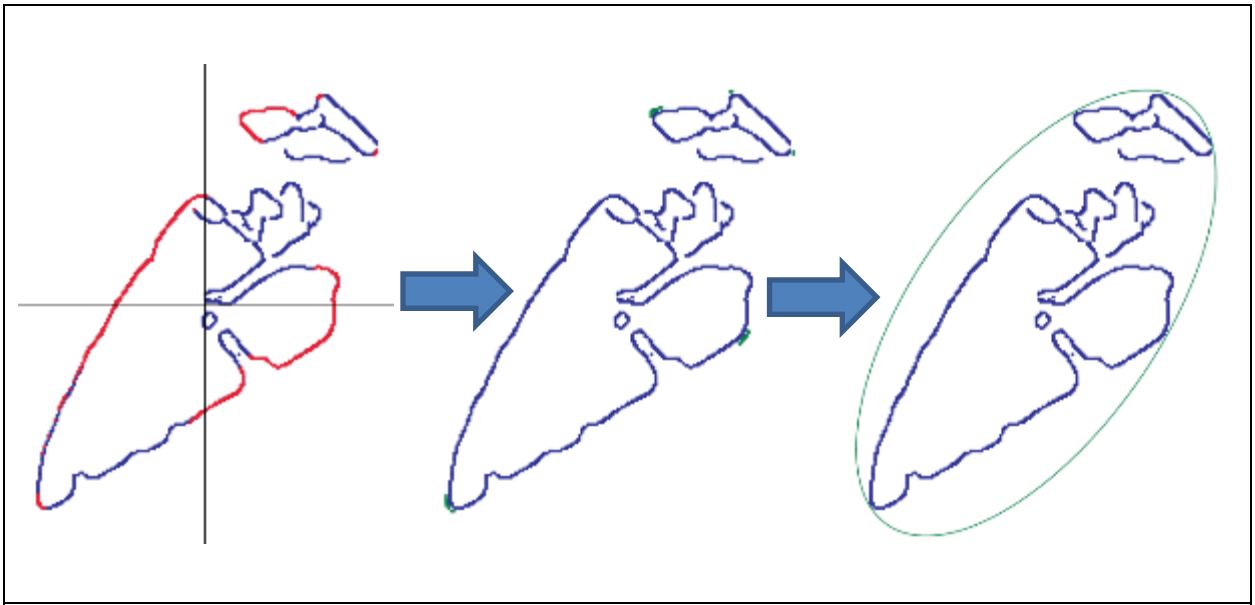

Figure A.6. Illustration of the Iterative fitting steps: (Right) Points located outside of the initial ellipse fitting (in red); (Center) new extreme points (in green) used to fit a new ellipse; (Left) final ellipse fitting after several iterations (in green).

Appendix B – Starting vector X0

The biggest caveat to calculate solution vector X is its dependency on $X0$. If starting vector is not well defined, the algorithm may diverge and the system may not present a solution. To select a good 'starting' $X0$ vector, the variables were split into linear ($X0_1$ and $X0_4$) and non-linear ($X0_2$ and $X0_3$). This separation is required to first estimate the non-linear values, and then the linear ones.

The justification of this process is described as follows. Let A and B be two aleatory variables and C, D two linear transformed aleatory variables from A and B, respectively:

$$C = iA + j$$
$$D = kB + l \qquad \text{B.1}$$

The correlation between A and B is, based on Taboga (2012):

$$Corr(A,B) = \frac{cov(A,B)}{\sigma_A \sigma_B} = \frac{\mathrm{E}[(A - \mathrm{E}[A])(\mathrm{B} - \mathrm{E}[B])]}{\left(\sqrt{\mathrm{E}[(A - \mathrm{E}[A])^2]}\right)\sqrt{\mathrm{E}[(B - \mathrm{E}[B])^2]}} \qquad \text{B.2}$$

The correlation between C and D is:

$$Corr(C,D) = \frac{cov(C,D)}{\sigma_C \sigma_D} = \frac{cov(iA+j, kB+l)}{\sigma_{iA+j}\sigma_{kB+l}} =$$

$$= \frac{\mathrm{E}[(iA+j-\mathrm{E}[iA+j])(kB+l-\mathrm{E}[kB+l])]}{\left(\sqrt{\mathrm{E}[(iA+j-\mathrm{E}[iA+j])^2]}\right)\left(\sqrt{\mathrm{E}[(kB+l-\mathrm{E}[kB+l])^2]}\right)} =$$

$$= \frac{\mathrm{E}[(iA-\mathrm{E}[iA]+j-\mathrm{E}[j])(k\mathrm{B}-\mathrm{E}[kB]+l-\mathrm{E}[l])]}{\left(\sqrt{\mathrm{E}[(iA-\mathrm{E}[iA]+j-\mathrm{E}[j])^2]}\right)\left(\sqrt{\mathrm{E}[(kB-\mathrm{E}[kB]+l-\mathrm{E}[l])^2]}\right)} = \qquad \text{B.3}$$

$$= \frac{\mathrm{E}[(iA-i\mathrm{E}[A]+j-j)(kB-k\mathrm{E}[B]+l-l)]}{\left(\sqrt{\mathrm{E}[(iA-i\mathrm{E}[A]+j-j)^2]}\right)\left(\sqrt{\mathrm{E}[(kB-k\mathrm{E}[B]+l-l)^2]}\right)} =$$

$$= \frac{ik\mathrm{E}[(A-\mathrm{E}[A])(\mathrm{B}-\mathrm{E}[B])]}{ik\left(\sqrt{\mathrm{E}[(A-\mathrm{E}[A])^2]}\right)\left(\sqrt{\mathrm{E}[(B-\mathrm{E}[B])^2]}\right)} = Corr(A,B)$$

Based on B.3 the correlation between two variables is invariant if one (or both) is subject to linear transformation.

For a given SDB linear regression where one wants to map from A (log ratio vector not considering water column contribution) into B (bathymetric control points), two linear parameters will do the mapping:

$$\begin{matrix} B_1 = iA_1 + j \\ \vdots \\ B_n = iA_n + j \end{matrix} \qquad \text{B.4}$$

To solve the system of equations in B.4, the matrix form:

$$\underbrace{\begin{pmatrix} B_1 \\ \vdots \\ B_n \end{pmatrix}}_{L} = \underbrace{\begin{pmatrix} A_1 & 1 \\ \vdots & \vdots \\ A_n & 1 \end{pmatrix}}_{A0} \underbrace{\begin{pmatrix} i \\ j \end{pmatrix}}_{K0} \tag{B.5}$$

The solution vector $K0$ will come from minimizing the quadratic sum of the residuals vector V:

$$V = A0K0 - L$$

$$\frac{d(V^T V)}{dK0} = 0 \tag{B.6}$$

$$K0 = (A0^T A0)^{-1}(A0^T L)$$

The minimum value $V^T V$ is the metrics for adjustment goodness under Least Squares Method (LSM). There is another way of estimating $V^T V$ without calculating solution vector $K0$. Taking the coefficient of determination r^2 between log ratio values and correspondent control points, it is possible to relate it to the minimum $V^T V$ (Weisstein, 2017):

$$r^2 = 1 - \frac{\sum_{i=1}^{n}[(A0K0)_i - B_i]^2}{\sum_{i=1}^{n}(B_i - \bar{B})^2}$$

$$r^2 = 1 - \frac{V^T V}{\sum_{i=1}^{n}(B_i - \bar{B})^2} \tag{B.7}$$

Where $\bar{B}$ is the mean value of bathymetric control points.

Since r^2 is the quadratic form of correlation coefficient, it is also insensitive to linear transformations of its aleatory variables. Going back to SDB linear regression, one could estimate the RMSE just using the correlation between the log ratio and its correspondent control points and the variance of observation vector L. If the intent is for a smaller $V^T V$, the model should address non-linear parameters that will also minimize r^2. Regarding the $X0$ estimation, the initial focus should be on $X0_2$ and $X0_3$. Since $X0_1$ and $X0_4$ have no potential impact on r^2, they were assigned 1 and 0 values, respectively. The non-linear parameters were based on simulated potential values. The range interval for each channel was based on:

$$L(\lambda_1) \approx L_w(\lambda_1) \mid e^{-2k(\lambda_1)z} \approx 0 \qquad \text{B.8}$$

B.8 condition is satisfied at optically deep waters. In the study site, each band values at deeper waters were evaluated to compose the ranges (Table B.1). The simulation also constrained the non-linear values to ignore complex numbers for depth estimations.

L8 Channel	Maximum water column	Minimum water column
B2 (blue)	10000	8400
B3 (green)	8000	6800
B4 (red)	7000	5900

Table B.1. Study site water column ranges per L8 channel.

Once the simulated $X0_2$ and $X0_3$ values are determined, they can be regarded as "fixed", and a new linear regression can be performed to estimate $X0_1$ and $X0_4$, as follows:

$$K1 = (A1^T A1)^{-1}(A1^T L) = \begin{pmatrix} X0_1 \\ X0_4 \end{pmatrix} \quad \text{B.9}$$

Where $A1 = \begin{pmatrix} ln\left[\frac{L(\lambda_1)_1 - X0_2}{L(\lambda_2)_1 - X0_3}\right] & 1 \\ \vdots & \vdots \\ ln\left[\frac{L(\lambda_1)_N - X0_2}{L(\lambda_2)_N - X0_3}\right] & 1 \end{pmatrix}$. Finally, the initial vector $X0$:

$$X0 = \begin{pmatrix} K1_1 \\ K0_1 \\ K0_2 \\ K1_2 \end{pmatrix} \quad \text{B.10}$$

Using this as a starting vector $X0$, it can be used to perform an interactive adjustment that will define solution vector X.